Electrochemical and Photoelectrochemical Properties of Oxide and Chalcogenide Semiconductors

by

FARINAZ FIROUZAN

DISSERTATION

Submitted in partial fulfillment of the requirements for the degree of Doctor of
Philosophy at The University of Texas at Arlington
December, 2020

Supervising committee:

Krishnan Rajeshwar, Supervising Professor
Daniel W. Armstrong
Saiful M. Chowdhury
Robin T. Macaluso

To

My parents,

Soheila Alizadeh & Alireza Firouzan

For their endless love and support

To

All doctoral students,

Who were on board flight PS572-Ukrainian Airline, which took off from Tehran's International Airport on 8th of January 2020 but never reached its destination. I will graduate thinking of each and every one of you and your families.

ACKNOWLEDGMENTS

I am sincerely thankful to my research advisor, Professor Krishnan Rajeshwar, for his continued support, contribution, and encouragement throughout my research work. I would also like to express my gratitude to my committee members Professor Daniel W. Armstrong, Professor Saiful M. Chowdhury, and Professor Robin T. Macaluso for their comments, advice, and support during my graduate studies. Also, I would like to take this opportunity to express my gratitude to collaborate with Professor Robin T. Macaluso's group and for her help over the course of my research. I greatly appreciate the assistance of all faculty and staff in the Department of Chemistry and Biochemistry at the University of Texas at Arlington. I owe a great debt of gratitude to my colleague and friend, Abbas Vali, for his generous help and support during my research.

Finally, and most importantly, my deepest gratitude is reserved for my parents, Soheila and Alireza who instilled a vision in me. Words will not be enough to articulate my heartfelt gratitude for my only brother, Yousef, my sister, Faranak and for my beloved, Kamyar. I am blessed to have all of them in my life. I would also like to thank all my UT Arlington and Texas friends for their instructions, demonstrations and thoughtful discussions.

Finally, my humble gratitude also goes to Professor Saiful M. Chowdhury for his suggestions and motivations throughout my PhD journey.

ABSTRACT

Electrochemical and Photoelectrochemical Properties of Oxide and Chalcogenide Semiconductors

Farinaz Firouzan, Ph.D.

The University of Texas at Arlington, 2020

Supervising Professor: Krishnan Rajeshwar

Photoelectrochemical (PEC) water splitting using inorganic semiconductors is a promising approach to store sunlight as sustainable fuels. Chalcogen-based (S, Se, Te) semiconductors are important in numerous technology applications especially related to photovoltaic solar conversion, fuel cells, hydrogen generation etc. On the other hand, oxide semiconductors offer many advantages such as stability in a variety of electrolytes, a diverse range of bandgaps and the Earth-abundance of their constituent elements. In this vein, we investigated the quaternary metal chalcogenide, $Ca(La_{1-x}Ce_x)_2S_4$ ($0 \leq x \leq 1$) photoelectrochemical behavior in an aqueous redox electrolyte. These solid solution series were synthesized in Prof. Macaluso's laboratory by a sealed ampule method. In this work, we mainly focused on the role of *f* electrons in the PEC behavior of these solid solution series, where the *f* electron density is absent in

$CaLa_2S_4$ and is progressively increased until it is maximized in $CaCe_2S_4$. All the samples were found to be *n*-type semiconductors as synthesized.

The second part of this research addressed the use of photocurrent polarity (i.e., whether anodic or cathodic) in a PEC situation to assess whether a Cu_2O semiconductor electrode sample behaved as an *n*- or *p*-type semiconductor. Using electrodeposited copper(I) oxide film as a sample platform, complications arising from the presence of Cu as an unwanted impurity phase and/or PEC corrosion of the oxide film in the photocurrent polarity data are discussed. Such artefacts are shown to be a possible contributory factor in many previous studies that have (erroneously) identified *n*-type semiconductor behavior in electrodeposited copper oxide films.

Among all the requisite properties of an inorganic semiconductor, the dynamics of interfacial charge transfer is an important common denominator for technological applications. Most attention in this regard has been paid to the dynamics of minority carrier transfer; only sporadic studies have focused on *majority* carrier transfer across the solid/electrolyte interface. However, recent studies have underlined the growing realization that the charge transfer kinetics of both minority and majority carriers are often coupled. Performance optimization of the interfaces must address both these charge transfer pathways such that deleterious carrier recombination can be minimized. Therefore, this portion of the dissertation study addresses the experimental understanding of interfacial charge transfer dynamics at semiconductor/electrolyte interfaces *in the dark*. For these experiments, binary *n*-type TiO_2 and WO_3 semiconductors were chosen because of their excellent PEC stability, high PEC activity, and overall robustness over a wide pH range. Similarly, binary and ternary *p*-type semiconductors such as copper (II) oxide (CuO), copper bismuth oxide ($CuBi_2O_4$), and silver vanadate ($AgVO_3$) were selected to compare their charge transfer kinetics in the dark. Such comparative studies are conspicuously absent in the literature, and in particular, dark current-forward bias potential measurements are largely lacking for these compounds. Tafel analyses were used to evaluate the standard rate constant, k°, the exchange current density, j_0, and the transfer coefficient, α in all these cases.

Based on these kinetics data, a general conclusion could be made that *p*-type oxide semiconductors exhibited faster kinetics than their *n*-type counterparts. For comparison, Pt electrode was included as benchmark in these experiments. The data also indicated that heterogeneous charge transfer at metal/electrolyte interfaces had faster kinetics compared to semiconductor/electrolyte interfaces. This contrasting behavior stems from surface state density variations in the two sets of cases. The most marked feature of the experimental data was the evidence for localized states within the bandgap. The results were interpreted on the basis of a model involving charge transfer mediated by surface states. The practical implications of these data are finally discussed.

TABLE OF CONTENTS

LIST OF ILLUSTRATIONS

LIST OF TABLES

CHAPTER 1

INTRODUCTION

The interconversion of different forms of energy has been of central importance in science and technology. The challenge of utilizing solar energy for the direct conversion of electricity and fuel has become a research topic of much current interest. This encourages fundamental investigations on the interactions of light and chemical/electrochemical reactions at electrode surfaces in electrochemical cells. Also, photoelectrochemical (PEC) water splitting by semiconductor photoelectrodes is a potential approach to convert intermittent sunlight into storable fuels and chemicals. Among various inorganic semiconductors, metal chalcogenide[1–5] and metal oxide semiconductors[6–8] are promising candidates because of their excellent properties for numerous technologically important applications such as PEC water splitting, photocatalytic pollutant degradation, or photovoltaic solar energy conversion. A brief background on these materials is given in the following sections.

1.1 Semiconductors

Materials exhibit different behavior mainly because of their chemical bonding and electronic band structures. The electronic band structure of solid materials consists of many closely-spaced electron energy levels in which the highest energy filled band, called the “valence band” (VB) is analogous to the highest occupied molecular orbital (HOMO) in molecules. The next higher band is the lowest unoccupied molecular orbital (LUMO) known as “conduction band” (CB) for the solid counterparts. The energy separation between these bands is called the energy band gap (E_g). Depending on the size of E_g, materials can be classified into electronic conductors, semiconductors, or insulators. Electronic conductors are a group of materials with no separation between their filled and unfilled energy levels (i.e., overlapped bands). The difference between semiconductors and insulators lies in their E_g size which defines the optoelectronic properties of the material. In this regard, insulators have a larger E_g than semiconductors; therefore, varying the temperature or applying a bias voltage will not result in significant charge transfer in insulating materials such as plastic, glass, wood, etc.

While semiconductors are akin to insulators by the nature of their band structure, adding a small amount of impurities (or “dopants”) into the host structure makes them electronically conductive. In the case of silicon (with four valence electrons), adding an impurity dopant with an extra valence electron (e.g., phosphorous with five valence electrons) than atoms of the host lattice, results in an *n*-type semiconductor. In contrast, doping with impurity atoms containing fewer valence electrons (e.g., boron with three valence electrons) than atoms of the host, results in a *p*-type semiconductor. Figure 1.1 shows a schematic diagram of the two types of semiconductors.

An important concept in semiconductor physics is the Fermi level (E_F), which is defined as the energy where the probability of a level being occupied by an electron (at 0 K) is ½. For an intrinsic semiconductor, E_F is approximately mid-point between the VB and CB. In a doped semiconductor, the location of E_F depends on the doping level. For *n*-type semiconductors, E_F lies slightly below the CB, whereas for *p* -type semiconductors, E_F lies slightly above the VB (Figure 1.1).

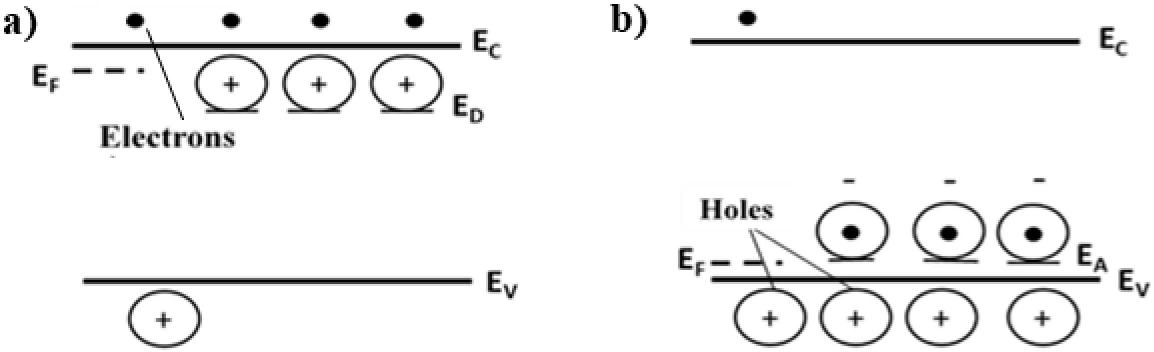

Figure 1.1 Schematic diagram of (a) *n*-type and (b) *p*-type semiconductors. E_F is the Fermi level of the semiconductor, E_D and E_A are the energy levels created by the donor and acceptor dopants, respectively. [Bard, A. J.; Faulkner, L. R. *Electrochemical Methods: Fundamentals and Applications*, 2nd ed.; Wiley: New York, 2001.].

1.2 Metal Chalcogenide Semiconductors

Metal chalcogenides, are the combinations of metals with the three chalcogen elements: sulfur, selenium, or tellurium. Chalcogenides of the transition and main group metals have attracted much attention because of the multitude of technological applications that they offer. These include solar photovoltaics[9–11] and water splitting,[12,13] thermoelectric energy conversion,[14] energy storage (batteries and supercapacitors),[15] heterogeneous (photo)catalysis,[15] electrocatalysis,[16,17] fuel cells[15,16] and even superconductors[18] and topological insulators.[5] Binary metal sulfides such as MoS_2 and WS_2, have become promising materials in this regard.[19–22] Of the binary sulfides, perhaps the most thoroughly studied in photoelectrochemical (PEC) and photocatalytic applications is CdS.[13] Its band gap is ~ 2.4 eV and absorbs wavelengths up to 510 nm. Its valence band edge position is compatible with the requirements for water photooxidation and photocatalytic environmental remediation.[23] Ternary (and quaternary) chalcogenides have gained importance in recent years, especially for applications related to photovoltaic solar conversion. Examples include copper indium gallium sulfide and selenide (CIGS) and copper zinc tin sulfide (CZTS).[24]

Rare-earth chalcogenides are also particularly interesting because of their wide array of crystal structures and physical properties.[2] One distinguishing feature of rare-earth chalcogenides is the localized nature of the 4*f* band. As examples of notable discoveries of new rare-earth chalcogenides in recent years, $Ce_8Sb_2S_{15}$ exhibits a red color due to a 4*f* to 5*d* electronic transition. Thus, the $f \rightarrow d$ electronic transitions are responsible for colors in other well-known metal chalcogenide pigments, CdS and CdSe.[25]

The optical transition in rare-earth chalcogenides is generally accepted as originating from electronic transitions involving localized $4f \rightarrow 5d$ orbitals. To better understand the role of *f* electrons in optical rare-earth based chalcogenides, we strategically chose to investigate a solid solution series, $Ca(La_{1-x}Ce_x)_2S_4$ ($0 \leq x \leq 1$) (prepared by Prof. Macaluso's group),[26] where the *f* electron density is absent in $CaLa_2S_4$ and is progressively increased until it is maximized in $CaCe_2S_4$. However, the PEC behavior of rare earth-derived chalcogenides such as γ-Ln_2S_3 and $CaLn_2S_4$, has not been investigated, at least to our knowledge. Thus, we investigated their structural, optical, and PEC behavior in our laboratory.

1.3 Metal Oxide Semiconductors

Oxide semiconductors are eminently attractive candidates for solar photovoltaic,[27] solar water photoelectrolysis[28] and photocatalytic remediation[29] applications. Historically, titanium dioxide (TiO_2) and zinc oxide (ZnO) are the materials which sparked worldwide interest in oxide semiconductors for the above applications. The main virtue of these oxide semiconductors relative to other types of semiconductor material candidates such as Group II-VI (*e.g.*, CdSe, CdTe) and Group III-V (*e.g.*, GaAs, InP) compounds is that the oxide component elements are generally both plentiful in nature (unlike Ga, In, etc.) and environmentally benign (unlike *e.g.*, Cd). Listed below are some of the properties of oxide semiconductors that determine their use in solar energy:[8]

- Optical energy gap (to have absorption in the visible region of the solar spectrum)
- Optimal positions of the conduction and valence band edges with respect to the reduction potentials of the substrate of interest
- Chemical, electrochemical, and photoelectrochemical stability
- Active surface area
- Nontoxic

Needless to say, the semiconductor has to be chemically inert and photochemically stable over a wide pH range. Further, the semiconductor surface has to have high electrocatalytic activity to sustain high photocurrents and large O_2 or H_2 generation rates. Finally, the use of a semiconductor photocatalysts for environmental remediation applications requires that both highly reducing and highly oxidizing active species are generated at the semiconductor/medium interface.[29] Thus the semiconductor conduction band-edge has to lie at a reasonably negative potential while the valence band-edge should be located at positive potentials. In addition, the photocatalyst must have all of the combination of optical, electronic, and surface characteristics listed above. It is difficult for one oxide semiconductor to possess all of these desirable properties. Therefore, it is not surprising that we do not yet even have an ideal candidate material for any one given application.

Oxide semiconductors were prepared with different methods previously developed in our laboratory.[30,31] Several methods have been commonly used to synthesize TiO_2 and WO_3 including hydrothermal,[32] electrodeposition,[33] chemical vapor deposition,[34] direct oxidation, and electrochemical anodization.[30,35] Of these methods, electrochemical anodization has attracted considerable interest since it can produce self-organized structures at ambient temperatures.[30] The dense and uniform nature of anodized oxides inhibits ionic conductivity along with offering excellent electron percolation pathways for charge transfer between interfaces.[30,35–39] Therefore, anodic oxide films with high surface area were initially used for the proposed research. On the other hand, cathodic electrodeposition has been successfully employed to fabricate *p*-type oxide semiconductors in the present work. While both anodic and cathodic deposition approaches are important, more precise control of film stoichiometry is obtained with the latter approach.[40] Electrodeposition was used to prepare the oxides on fluorine-doped tin oxide (FTO) substrate.

Electrodeposition is well established for depositing metals with a wide range of applications from large-area surface treatments to most advanced electronic industries.

This method facilitates large-area deposition and low-temperature processing of materials where large areas of semiconductors are required such as in photovoltaic power generation.[41] The TiO_2 and WO_3 thin films were anodically grown on the corresponding metal substrates (Ti and W respectively). Other selected *p*-type semiconductors were deposited on FTO substrates. These substrates have shown excellent stability in aqueous media.[42] Equally important, the intrinsically good optical transparency of FTO substrates is a bonus for optoelectronic and PEC experiments.[42]

1.4 Kinetic Parameters of Oxide Semiconductors

In electrochemistry, the estimation of the standard rate constant, k^0, is of paramount interest when the performance of electrode materials is examined. The rate constant offers an indication of the speed of interfacial charge transfer between an electroactive species and the electrode surface.[43] As it stands, k^0 is one of the most substantial pieces of information one can extract through the use of electrochemical techniques. Although considerable literature concerning semiconductor electrodes exists,[36,44–48] charge transfer kinetics at the semiconductor/electrolyte interfaces must be further explored.

This dissertation addresses experimental analyses of the interfacial charge transfer process at the semiconductor/electrolyte interface *in the dark*. In this regard, TiO_2 and WO_3 as *n*-type and CuO, $CuBi_2O_4$, and $AgVO_3$ as *p*-type oxide candidate semiconductors were selected to study their charge transfer kinetics. These oxide (TiO_2 and WO_3) semiconductor materials are known for their excellent chemical and PEC stabilities, high photoactivity, and stability in a wide pH range.[49] These oxides are also important in many important applications. For example, $CuBi_2O_4$ is a *p*-type semiconductor that possesses several attractive features for use as a photocathode in solar water splitting.[50] Silver vanadate ($AgVO_3$) is a promising ternary oxide semiconductor for water splitting and photocatalytic remediation because of its small E_g and chemical stability.[51] Copper (II) oxide (CuO) has attracted much attention because of its application in photovoltaic solar cells and its high solar absorbance and non-toxicity. This material is also important for high T_C superconductors.[52]

1.5 Dissertation Outline

Chapter 2 describes the theoretical background and literature review of this work. Chapter 3 explains the chemicals, instrumentation, and procedures that were used in this dissertation project. Chapter 4 contains the results and discussion on two aspects: (a) photoelectrochemical properties of metal oxides and metal chalcogenide semiconductors (b) electrochemical properties of metal oxide semiconductors including charge transfer kinetics of *n*- and *p*-type semiconductors in the dark. Chapter 5 finally summarizes the conclusions that were made from this project.

CHAPTER 2

THEORETICAL BACKGROUND

2.1 Electrochemistry Concepts

Electrochemistry is a branch of chemistry that deals with the interconversion between electrical and chemical energy. Its application in everyday life expands from batteries, controlling corrosion, metallurgy, electrolysis and even technological advances like electric cars and generally anything that involves energy storage.[53–55] Electrochemical measurements on chemical systems are carried out for various reasons including, attainment of thermodynamic data about a reaction, generation of unstable intermediates, and analysis of trace amount of metals and inorganic compound in different systems.[55] Oxidation and reduction reactions play an important role in all of these electrochemical processes. An oxidation reaction involves the loss of one or more electrons from chemical species while a reduction reaction is the gain of one or more electrons by chemical species. It is not possible to have one process without the other one and the combination of these two processes together is called a redox reaction.[54]

According to these definitions, the main principle of electrochemical processes is based on the transfer of electrons in a system; electrons can flow from the oxidized species, which is also called the reducing agent or reductant, to the reduced species (Red), which is also called the oxidizing agent or oxidant (Ox).[53] An electrochemical system consists of three different electrodes, working, counter, and reference. The working electrode is the electrode in which the reaction of interest is occurring.[54,55] It is often used in conjunction with a counterelectrode and a reference electrode in a three electrode system.

Depending on whether the reaction on the electrode is a reduction or an oxidation, the working electrode can be referred to as either a cathode or an anode. Gold, silver, platinum, inert carbon such as glassy carbon, mercury drop and film electrodes are commonly used electrode materials. The counterelectrode, along with the working electrode, completes the circuit over which current is either controlled or measured. The potential of the counterelectrode is not measured and adjusts to complete the reaction occurring at the working electrode. This configuration allows the potential of the working electrode to be measured against a known reference electrode without compromising the stability of that reference electrode by passing current through it.[54,55] A reference electrode is an electrode which has a stable and well-defined electrode potential.

To understand the role of electrochemistry in different chemical reactions, a variety of electrochemical methods have been developed.[55] These methods can either lead to acquisition of quantitative information about a chemical reaction like the number of electrons transferred or the redox behavior. Voltammetry is an important class of electrochemical methods. Voltammetry applies a constant/varying potential at the working electrode and measures the resulting current. This method gives information about the redox potential of an analyte and its electrochemical behavior. Linear sweep voltammetry (LSV)[56] is an example of a potential sweep technique in which the electrode potential is ramped between two potential limits at a particular scan rate while the electrode current is monitored.[55] The resulting curve is known as a voltammogram and provides information on the rate of electrochemical reactions as a function of potential. From the sweep-rate dependence of the voltametric current, several quantitative properties of the charge transfer reaction can be determined. The measured current during this process is often normalized to the electrode surface area and is referred to as the current density.[55] The current density is also plotted against the applied potential.

2.2 Photoelectrochemistry Concepts

Photoelectrochemistry studies the interaction between light and electrochemical systems. In other words, it is the reaction on the electrode in an excited state.[10] This excitation can originate from an electrode (metal or semiconductor) or a substance (adsorbed molecule) at the interface between the electrode and a solution.[57] In photoelectrochemical experiments, irradiation of an electrode with light, absorbed by the electrode material, causes the generation of a current called a photocurrent. The dependence of photocurrent on the wavelength, electrode potential, and solution composition provides information about the nature of photoprocesses and their energetics and kinetics.[55]

In recent years, a tremendous surge of interest has developed in the field of photoelectrochemistry, particularly in the application of PEC systems to the problem of solar energy conversion and storage.[58] In a historical context, it is interesting to note that most of the studies in the 1970s and the early 1980s were oriented toward photovoltaic conversion (the conversion of sunlight to electrical power) and energy storage possibilities with PEC devices. In the late 1980s and with the falling of oil prices, a reorientation of PEC studies toward materials synthesis, processing, and characterization particularly with the electronics industry as a target consumer, was promoted.[59] Until now, photovoltaics has been dominated by solid state junction devices, often made of silicon. Recently, the emergence of a new generation of photovoltaic cells, based on nanocrystalline materials and conducting polymer films has been the topic of many studies.[58,60–62] These cells offer the prospect of cheap fabrication together with other attractive features such as flexibility. The phenomenal recent progress in fabricating and characterizing nanocrystalline materials has opened up a whole new window of opportunity. Surprisingly, some of the new devices have high conversion efficiencies, which compete with those of conventional devices.[58]

All phenomena associated with the photoelectrochemical systems are based on the semiconductor/electrolyte interface.[55] The main component of every PEC cell is the semiconductor which converts incident photons to electron-hole pairs.[55] When a semiconductor is irradiated with photons of energy ≥ than the E_g, the electrons from the valence band are excited to the conduction band (e_{CB}^{-}), leaving a positively charged particle in the valence band, termed a 'hole' (h_{CB}^{+}), see Reaction 2.1.

$$hv \rightarrow e^{-} + h^{+} \qquad [2.1]$$

The electron – hole pairs then diffuse and/or migrate to the semiconductor surface and can take part in subsequent redox reactions.

A schematic diagram of the photocatalysis process is shown in Figure 2.1 below. These photogenerated charge carriers can undergo (i) recombination in the bulk of the semiconductor or through trap states on the surface, and release heat and/or luminescence; or else (ii) charge transfer, by reacting with an electron acceptor or donor species resulting in subsequent redox reactions.[28,35] Figure 2.2 is a schematic diagram of the different recombination and charge transfer processes on a semiconductor particle. The photocatalytic efficiency depends on the number of charge carriers taking part in the reaction, and on the effective separation of the photogenerated electron – hole pairs. Electron – hole pairs in the bulk of the semiconductor recombine with evolution of heat. Those present in the space-charge region (the excess charge in the semiconductor that does not reside at the surface, as it would in a metal, is distributed in this region) are separated and result in current generation. Some undergo recombination either within the space charge region or in trap states at the surface.

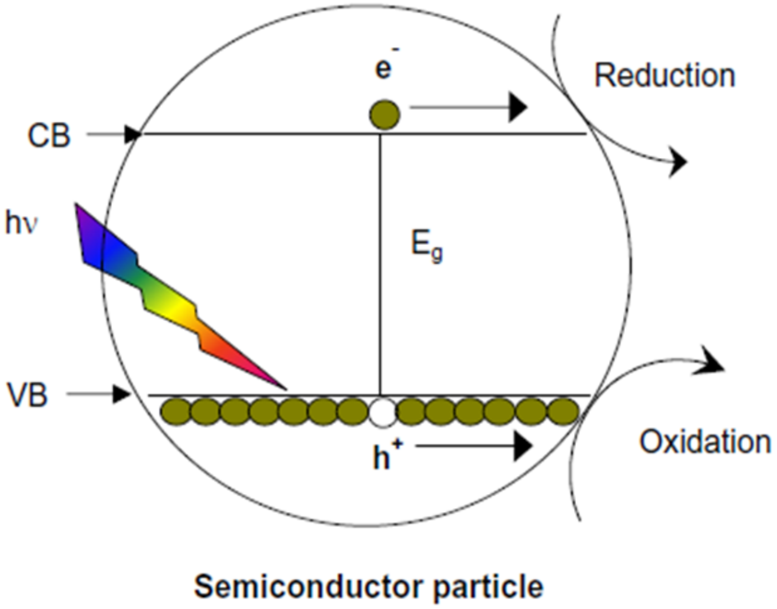

Figure 2.1 Schematic diagram of bands and electron-hole pair formation on light absorption in a semiconductor particle shown as a sphere. [Memming, R. Electron Transfer Process with Excited Molecules at Semiconductor Electrodes, *Prog. Surf. Sci.*, 1984, 17, 7-74.].

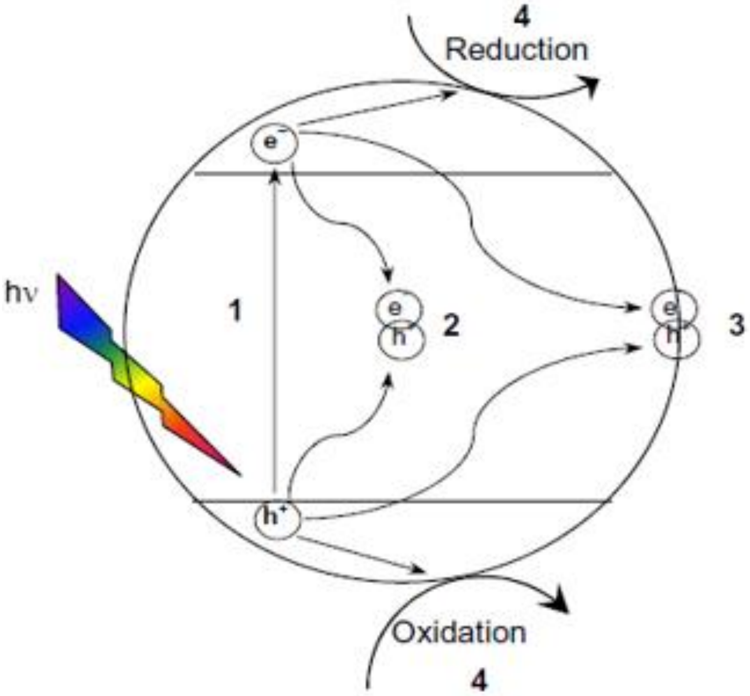

Figure 2.2 Schematic representation of the recombination and redox processes on the semiconductor particle. (1) charge carrier generation; (2) bulk recombination; (3) surface recombination; (4) charge transfer. [Memming, R. Electron Transfer Process with Excited Molecules at Semiconductor Electrodes, *Prog. Surf. Sci*., 1984, 17, 7-74.].

The electrons move from the semiconductor phase to the external circuit, while the holes move to the surface and oxidize the species in solution, generating *photoanodic* current in a *n*-type semiconductor. Photooxidation occurs at less positive potentials than that required for an inert metal electrode since light irradiation assists the oxidation process. Similarly, irradiation of a *p*-type semiconductor results in *photocathodic* current flow and promotes a photo-reduction reaction.[54,55] In the next section, the kinetics aspects of charge transfer in the dark are briefly addressed.

2.3 Charge Transfer Kinetics in the Dark

Charge transfer occurs between two quantum states: from a filled donor state to an empty acceptor state. Charge transfer reaction from an electrode (an electronic conductor, metal or semiconductor) to a redox couple in an electrolyte can be cathodic or anodic. The cathodic (reduction) process occurs from an occupied state in the electrode to a vacant state in the electrolyte. This state is offered by the oxidized species (Ox) of the redox couple. In the anodic (oxidation) process, electrons from the reduced species (Red) of an occupied state in the electrolyte transfer to a vacant state in the electrode. In heterogeneous charge transfer, electrons are transferred between the redox active chemical species and a solid-state electrode. Qualitative and quantitative analysis of the rates of heterogeneous charge transfer processes has been the focus of many studies due to their technological and scientific significance. The past couple of decades have witnessed remarkable advances in the development of several theories on the interfacial charge transfer process.[44,63–72] These theories have been proposed to explain the standard rates of heterogenous charge transfer reactions in electrode/electrolyte interfaces.

2.3.1 Metal/Electrolyte Interface (MEI)

In the case of metal/electrolyte interface, immersing a metal electrode in solution results in immediate charge transfer at the interface resulting in an equilibrium condition (no net current flow).[55] At equilibrium, the E_F of the metal electrode will be equal to the Fermi level of the redox species in solution (solution redox energy).[55] A graphic illustration of this situation is seen in Figure 2.3; it displays the corresponding distribution of occupied and vacant states in both phases at equilibrium.

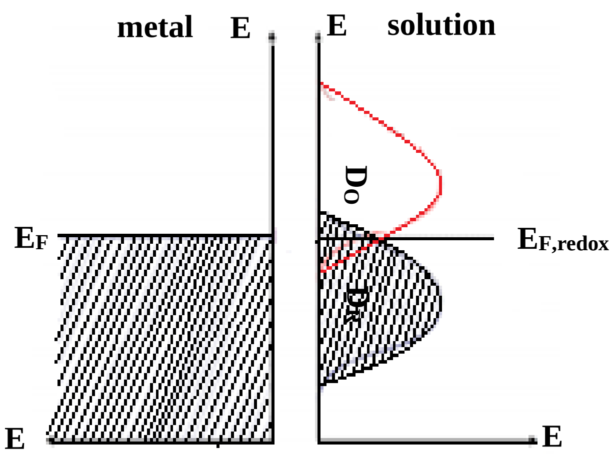

Figure 2.3 Schematic diagram of the metal/electrolyte interface at equilibrium. [Memming, R. Electron Transfer Process with Excited Molecules at Semiconductor Electrodes, *Prog. Surf. Sci.*, 1984, 17, 7-74.].

In an electrochemical reaction, equilibrium is characterized by the Nernst equation (Eq. 2.2), which links the electrode potential to the bulk concentrations of the participants as shown below, where C_O* and C_R* are the bulk concentrations of oxidized and reduced redox species, and $E°'$ is the formal potential.[55] As a result, for a simple one-step one-electron transfer, the rate constant of electron transfer must be equal in both directions and equal to the standard rate constant (k^0).

$$Ox + ne^- \leftrightarrow Red \quad , \quad E = E^{0\prime} + \frac{RT}{nF} \ln \frac{C_O^*}{C_R^*} \qquad [2.2]$$

In a metal electrode, charge transfer occurs in the vicinity of the Fermi level ($E = E_F$). The solution side of the interface is thought to be made up of several "layers." That closest to the electrode, the *inner layer,* which contains solvent molecules and sometimes other species (ions or molecules) that are said to be specifically adsorbed, is called Helmholtz double layer.[55] According to the Gerischer model[44] for a MEI, charge transfer reactions at interfaces are strongly affected by the electric forces, which are present in the electric double layer. Since these forces can be varied by external overpotential (η), the kinetics are phenomenologically characterized by the relations between current and applied overpotential. The *i-E* (current *vs*. potential) data will be utilized to extract the kinetic parameters of the electrochemical reaction for the metal (*e.g.*, Pt), oxides (*n*- and *p*-type), and chalcogenide semiconductors ($Ca(La_{1-x}Ce_x)_2S_4$) as mentioned in a previous chapter.

2.3.2 Methodology

At the MEI, polarization in both cathodic and anodic directions, often results in symmetric current flow as schematically shown in Figure 2.4. The current-overpotential behavior of the metal/electrolyte interfaces is different from that at semiconductors because there is always a large density of states in the conductor. In addition, the concentration of electrons on the surface is not a function of overpotential. The kinetics of majority carrier charge transfer in the dark can be gleaned by converting the polarization curve (*i vs. E*) to a Tafel plot (*log i vs.* η).[55] Tafel plot is a convenient way to analyze electrode properties and the reaction mechanism; also it can be used to derive important kinetic parameters. Thus, for analyzing electrochemical performance, the Tafel analysis is combined with the Butler-Volmer equation (Eq. 2.3) in many studies.[55]

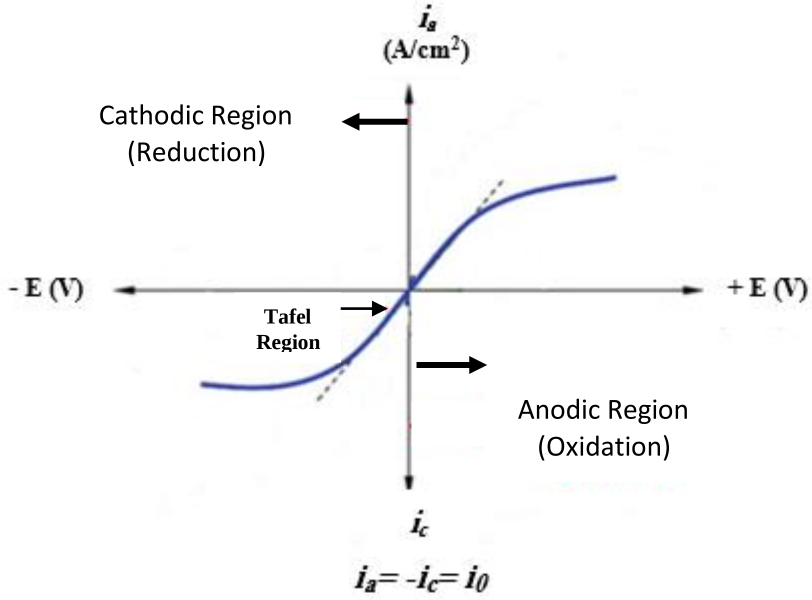

Figure 2.4 Polarization curve for a metal/electrolyte interface.

The Tafel equation (Eq. 2.4) relates the reaction rate, as measured by an electric current, to the applied electrochemical overpotential via a linear correlation between *log i* and η, (see Eq. 2.4). By combining with the Arrhenius equation and Transition State Theory,[55] the Tafel slope, *b*, can be derived to be reversely proportional to the so-called charge transfer coefficient (α), in Equation [2.5].[55]

$$i = i_0 \, [e^{-\alpha f \eta} - e^{(1-\alpha) f \eta}] \qquad [2.3]$$

$$\eta = a + b \log i \quad (\eta = E - E^0) \qquad [2.4]$$

$$b = \frac{2.3\ RT}{\alpha F} \qquad [2.5]$$

where i is a net current (A), i_0 is the exchange current (A), α is a transfer coefficient, $f = F/RT$, η is overpotential (V), and the symbols F, R and T have their usual significance.

The slope of a Tafel plot affords the value for α, the intercept yields the exchange current (i_0, the current at equilibrium, i.e., the rate at which oxidized and reduced species transfer electrons with the electrode) known as a descriptor of the catalytic activity (Eq. 2.6), and the corresponding k^0 (cm.s^{-1}) value can be derived from Equation 2.7.[55]

$$log\ i = log\ i_0 - \frac{\alpha F}{2.3\ RT}\eta \qquad [2.6]$$

$$i_0 = nFAk^0C^* \qquad [2.7]$$

In equations [2.6] and [2.7], A is the electrode area, C^* (mol.cm^{-3}) is the redox concentration, and k^0(cm. s^{-1}) is the standard heterogeneous rate constant. These equations were applied to estimate α, j_0 ($\frac{i_0}{A}$, exchange current density) and k^0 of materials in what follows.

In an ideal system with perfect symmetry, $\alpha = 0.5$ and i_0 is proportional to k^0. Such Tafel plots are illustrated in Figure 2.5 for a MEI in both polarization directions. As shown in Figure 2.5, there is an anodic branch with slope of $(1- a)\ F/2.3RT$ and a cathodic branch with slope of $-aF/2.3RT$ to apply for the determination of a. In addition, both linear directions extrapolate to an intercept of log i_0 to calculate the standard rate constant of the electrode. The plots deviate sharply from linear behavior as η approaches zero, because the back reactions can no longer be considered as negligible.

Of the approaches considered thus far for determination of k^0, cyclic voltammetry (CV)[73] has proved useful for probing the kinetic parameters, since the Marcus theory[72,74,75] was first reported. The equations developed by Nicholson [76–78] can be used to estimate k^0 values for the electrode materials.

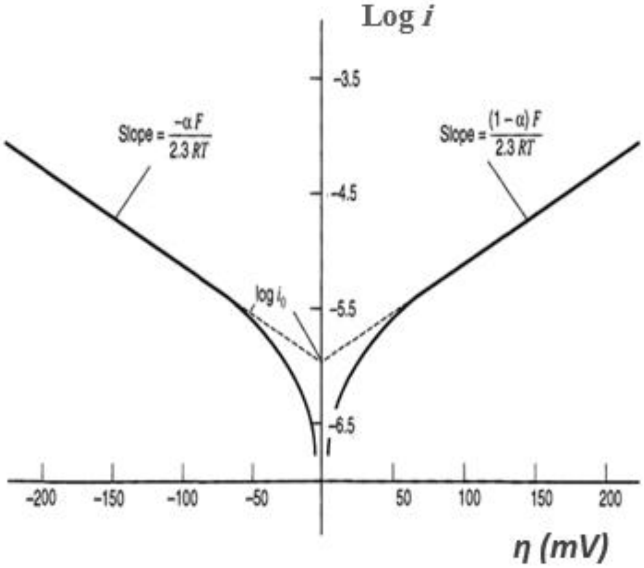

Figure 2.5 Tafel plots for anodic and cathodic branches of the current-overpotential curves for O + ne^- ↔R. [Bard, A. J.; Faulkner, L. R. *Electrochemical Methods: Fundamentals and Applications*, 2nd ed.; Wiley: New York, 2001.].

Tables 2.1 and 2.2 summarize literature studies on the kinetic parameters of Pt with various techniques and methods for two different redox couples, Fe $(CN)_6^{3-/4-}$ and $Fe^{2+/3+}$. The α values (~ 0.5) in Table 2.1 for Pt electrode from different methods illustrate the symmetry of energy barriers in the reaction. This idea can be amplified by considering α in terms of the geometry of the cathodic and anodic intersection regions in the Tafel plot for metal electrodes. In an ideal system, the standard Tafel plot is expected to be linear with a slope of $2.3RT/\alpha F$ (*i.e.*, $59.1/\alpha$ (mV/decade) at 25 °C).[55] Larger slopes are generally found for systems that do not have Nernstian heterogeneous kinetics and overall chemical reversibility.[55]

Table 2.1 Kinetics parameters for Pt and $Fe(CN)_6^{3-/4-}$ redox couple.

Entry No.	α	$J_0 \times 10^3$ (A/cm^2)	$k^0 \times 10^2$ (cm/s)	Technique	Ref.
1	NR	NR	9.0	Faradaic impedance	79
2	0.55 0.50	9.2 10.0	9.5 13	Cyclic potential step Cyclic coulombic step	80
3	NR	NR	8.0	Rotating disk electrode	81
4	0.61	50	5.0	Rotating disk electrode	82
5	0.50 0.46	NR NR	24 2.8	Current impulse	83
6	0.50	NR	3.0	Rotating disk electrode	84
7	NR	NR	10.9	Cyclic voltammetry	85
8	NR	NR	1.7	Cyclic voltammetry	42
9	0.24 (R) 0.59 (O)	NR NR	1.5 1.3	Rotating disk electrode Rotating disk electrode	86
10	0.45 NR	NR NR	14 8.5	Steady state voltammetry Cyclic voltammetry	87
11	0.50	NR	0.1	Rotating disk electrode	88

Table 2.2 Kinetics parameters for Pt and $Fe^{2+/3+}$ redox couple.

Entry No.	α	$J_0 \times 10^2$ (A/cm^2)	$k^0 \times 10^3$ (cm/s)	Technique	Ref.
1	NR	3.21	3.0	Linear sweep voltammetry	89
2	0.46	NR	4.0	Faradaic impedance	79
3	0.38 0.39	4.78 5.26	5.0	Cyclic potential step Cyclic current step	80
4	NR	2.34	5.3	Linear sweep voltammetry	90
5	NR	NR	11	Rotating disk electrode	81
6	0.46	NR	4.3	Rotating disk electrode	91
7	0.63	0.23	2.4	Rotating disk electrode	82
8	0.50	NR	9.0	Rotating disk electrode	84
9	0.49	NR	1.5	Rotating disk electrode	92
10	NR	NR	3.0	Cyclic voltammetry	42
11	0.50 0.50	0.64 0.59	1.3 1.2	Rotating disk electrode Rotating cylinder electrode	93
12	0.37 (R) 0.73 (O)	NR NR	10 5.0	Rotating disk electrode Rotating disk electrode	86

Interestingly enough, the rate constants quoted in Tables 2.1 and 2.2 are in good agreement with the extreme sensitivity of $Fe(CN)_6^{3-/4-}$ to the surface effects reported by previous investigators in my group.[42] The pertinent observations reveal k^0 values to be one order of magnitude smaller compared to the Pt electrodes in contact with $Fe^{2+/3+}$ the redox couple. Although many studies of heterogeneous rate constants are available for metal electrodes,[84,86,94–98] relatively little kinetic information exists for semiconductor electrodes; this is discussed in the next section.

2.3.3 Semiconductor/Electrolyte Interface

When a semiconductor comes into contact with a redox electrolyte, the Fermi levels of the semiconductor and redox species are equalized. Unlike in a metal, the energy bands are bent upward or downward depending on the dopant as shown in Figure 2.6. For an *n*-type semiconductor, the *space-charge region* comprises of positive charges due to the depletion of electrons from it (depletion layer). The band edges in this region are thus different from the energies in the bulk of the semiconductor. Due to the positive charge in the space-charge region, the band edges are bent upwards (band bending) due to the energy difference between the space-charge region and the bulk of the semiconductor. In the case of a *p*-type semiconductor, the space-charge region consists of excess negative charge and the bands are bent downwards (Figure 2.6).

In an ideal semiconductor/electrolyte interface without surface or interface states, charge transfer can only occur *via* the two energy bands, and the two processes can be treated separately.[55] This is because the charge transfer process at the semiconductor/electrolyte interface is strongly affected by the density of available carriers (electrons and holes) at the interface.

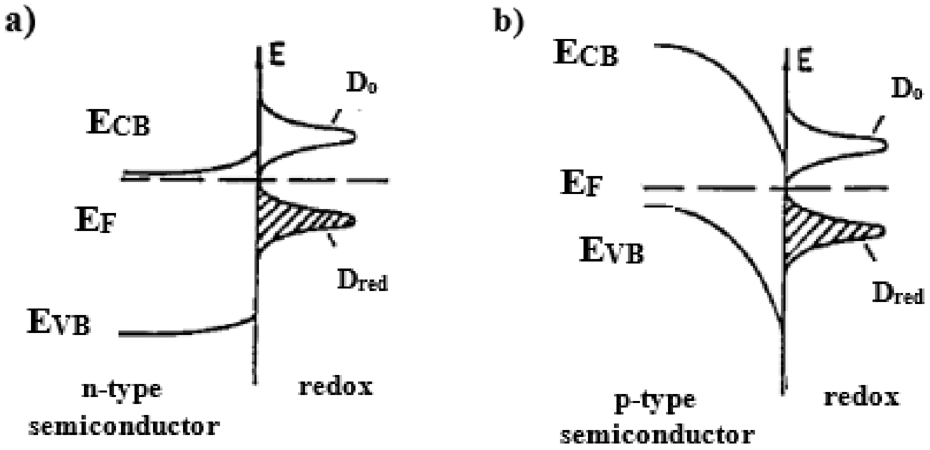

Figure 2.6 Semiconductor/electrolyte interfaces at equilibrium a) *n*-type and b) *p*-type. [Bard, A. J.; Faulkner, L. R. *Electrochemical Methods: Fundamentals and Applications*, 2nd ed.; Wiley-VCH : New York, 2001.].

The observed *i-E* behavior of a semiconductor/electrolyte interface (Figure 2.7) differs from that at metals, where there is always a large density of states in the conductor. In the *dark*, charge transfer involving redox species in solution with energy levels in the band gap of the semiconductor is usually dominated by the majority carriers, electrons for *n*-type and holes for *p*-type. Despite many published papers on theories of charge transfer kinetics, experimental studies of the kinetics at semiconductor electrodes have not advanced as rapidly. Most experiments in this field are still interpreted within the context of a model developed in the 1960s by Gerischer.[70,99] The problem here lies in precise control of the physical parameters of electrodes (thickness, porosity, surface states, the doping level etc.), among others, to ensure sufficient reproducibility of the kinetics measurements.

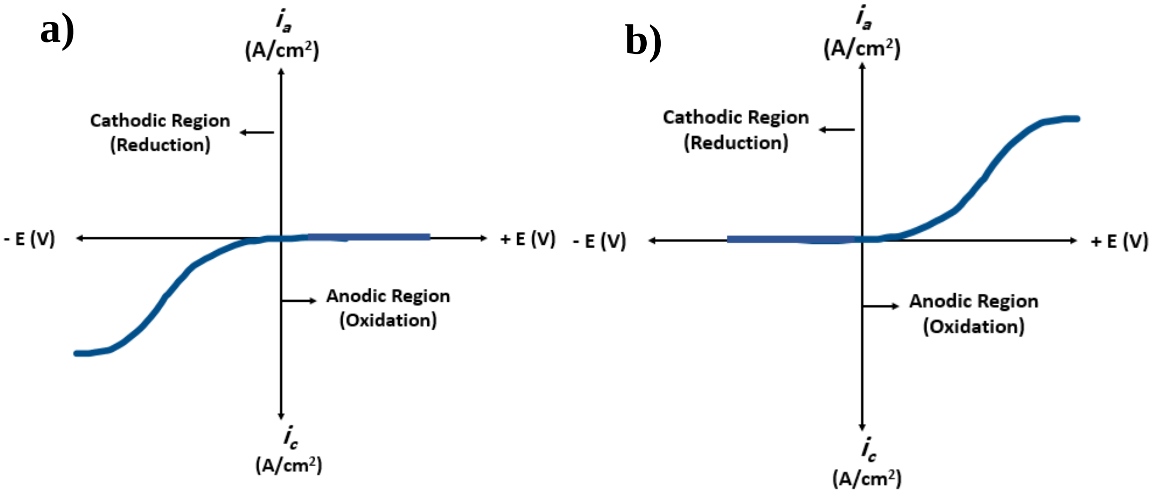

Figure 2.7 Schematic *i*-*E* curves of a) *n*-type, b) *p*-type semiconductor.

Likewise, relatively few measurements have been reported at *nonilluminated* semiconductor electrodes in the past few decades (see Tables 2.3 and 2.4).

The fundamental aspects of interfacial charge transfer kinetics were reviewed by Lewis[100] interpreting different forms of rate constants and expressions. The first part of this review consisted of developing a mathematical framework for rate constant expressions commonly used to describe interfacial charge transfer kinetics. Toward this goal, he defined two different expressions of standard rate constants for semiconductor/electrolyte interfaces, k_{sc}^{0}, one in the unit, cm.s^{-1}; and the other one by considering the concentration of majority carriers at the electrode surface (n_{sc} and p_{sc}), yielding the unit, cm^{4}.s^{-1}. Following these expressions, relevant data are presented in Tables 2.3 and 2.4; they were culled from previous literature studies *in the dark*. These data include oxide semiconductors, elemental and binary non-oxide semiconductors, and chalcogenide semiconductors.

Table 2.3 [a] Literature data on charge transfer rate constants for oxide semiconductors.

Entry No.	Oxide Semiconductor	Redox Couple	Electrolyte	Standard Rate Constant		Ref
				k^0 (cm/s)	k^0 (cm^4/s)	
1	ITO	$Fe(CN)_6^{3-/4-}$ $Fe^{2+/3+}$	1 M KNO_3	2.7×10^{-3} 1.1×10^{-3}	---	42
2	ZnO	FC^+/FC DM^+/DM	0.1 M $TBABF_4$	---	4.0×10^{-18} 7.0×10^{-23}	101
3	WO_3	Fc FcAc $FcMe_{10}$	0.1 M CH_3CN	---	3.1×10^{-24} 0.65×10^{-24} 3.6×10^{-24}	102

[a] Abbreviations used in this table: Fc = Ferrocene, FcAc = Acetylferocene, $FcMe_{10}$ = bis(pentamethylcyclopentadienyl), FC^+/FC = Ferricenium, DM^+/DM = decamethyl ferricenium, $TBABF_4$ = tetrabutylammonium fluoroborate, ITO = Indium tin oxide.

Table 2.4 [a] Literature data on charge transfer rate constants for non-oxide semiconductors.

Entry No.	SC	*p*/*n*-type	Redox Couple	Electrolyte	Standard Rate Constant		Ref
					k^0 (cm/s)	k^0 (cm^4/s)	
a) Elemental Semiconductors							
1	Si	*n*	benzyl viologen$^{2+/+}$	1.0 M LiCl	---	$(6.0\pm 3.0)\times 10^{-17}$	103
2	Si	*n*	$Ru(NH_3)_6^{3+}$ MV^{2+} $Co(sep)_3^{3+}$	1.0 M KCl	---	$(5.9\pm 1.2)\times10^{-16}$ $(1.1\pm 0.3)\times10^{-22}$ $(3.5\pm 4.6)\times10^{-23}$	104
b) *n*-type Binary Semiconductors							
3	GaAs	*n*	Cu^{1+}/Cu^{2+}	6.0 M HCl	2.7×10^{-10} [b]	---	105
4	$Fe_{80}B_{20}$	*n*	$Fe(CN)_6^{3-/4-}$	Borate buffered pH=8.4	5.7×10^{-13} 4.4×10^{-14}	---	106
c) *p*-type Binary Semiconductors							
5	GaAs	*p*	Cu^{1+}/Cu^{2+}	6.0 M HCl	1.0×10^{-2}	---	107
d) *n*-type Binary Chalcogenides							
6	MoS_2	*n*	$Fe(CN)_6^{3-/4-}$ $Cu(NH_3)_4^{2+/1+}$	0.50 M KCl pH= 7 0.50 M NH_4Cl pH= 10.5	3.0×10^{-8} 8.0×10^{-7}	---	108
e) *p*-type Binary Chalcogenides							
7	WSe_2	*p*	$Ru(NH_3)_6^{3+/2+}$	0.50 M Na_2SO_4	1.7×10^{-16}	---	109

[a] Abbreviations used in this table: MV^{2+} = methylviologen dication, [b] Calculated from their data, SC = semiconductor.

2.4. Charge Transfer Kinetics via Surface States

There are two main routes for charge transfer processes between the semiconductor electrode and the electrolyte: (1) Direct, *isoenergetic* charge transfer between the conduction band or valence band in the semiconductor and energy levels in the electrolyte. This model was first developed by Marcus[110] and then by Gerischer.[70] It predicts that, provided E_{cs} (conduction band energy at the surface) does not change with polarization, the current is proportional both to the density of electrons at the surface, n_s, and the concentration of oxidized species, C_{ox}. (2) *Inelastic* electron and hole transfer involving states localized in the bandgap of the semiconductor in a two-step mechanism: filling of surface states with conduction band electrons, and further isoenergetic transfer to empty electrolyte levels. In other words, charge transfer can be mediated by surface or interface states. Figure 2.8 schematically shows the two routes for charge transfer between the semiconductor and electrolyte.

Bard *et al.*[111] were the first to invoke mediation of charge transfer by surface states in order to explain the anomalously *high* Tafel slopes. Later, Vandermolen *et al.*[49] were the first to observe current saturation in Tafel plots. They interpreted this phenomenon with a two-step charge transfer kinetics model involving surface states within the bandgap. The current saturation was found in some 3*d*-orbital semiconductors in the dark cathodic reduction of the oxidized electrolyte species.[112] In contrast, semiconductors such as ZnO, the ones without *d*-orbitals in their conduction band, showed ideal behavior in the dark cathodic reduction process.[112] This lends credence to the idea that the surface states present in transition metal oxides, also mediate charge transfer to the electrolyte.

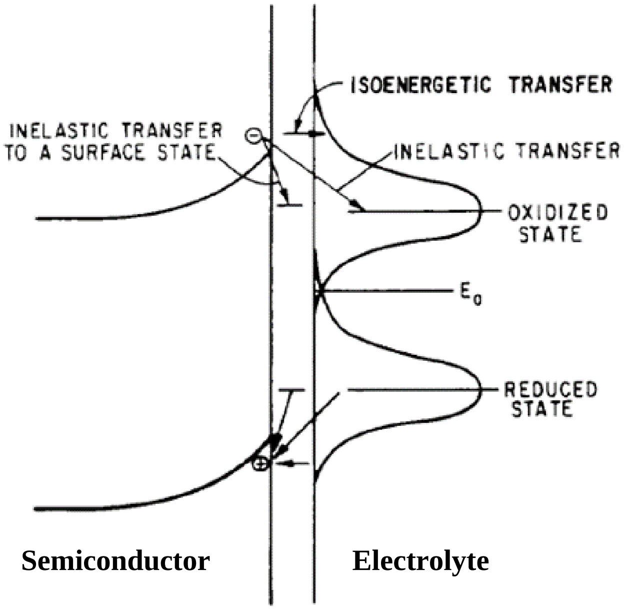

Figure 2.8 Schematic illustration of various electron transfer processes between the semiconductor electrode and electrolyte.[R. H. Wilson, *Electron Transfer Processes at the Semiconductor-Electrolyte Interface,* Taylor & Francis: New York, 1980; pp. 1–87.].

CHAPTER 3

EXPERIMENTAL

3.1 $Ca(La_{1-x}Ce_x)_2S_4$ ($0 \leq x \leq 1$)

Powder samples of $Ca(La_{1-x} Ce_x)_2S_4$ ($0 \leq x \leq 1$) were prepared in Prof. Macaluso's group by grinding a stoichiometric ratio of CaS, Ce_2S_3 and La_2S_3 with an agate mortar and pestle. The powders were ground and placed in tantalum foil inside a dry box filled with circulating ultra-high purity argon. The foil and its contents were placed inside a fused silica ampoule and sealed under vacuum as per details given elsewhere.[26]

3.1.1 Preparation of $Ca(La_{1-x} Ce_x)_2S_4$ ($0 \leq x \leq 1$) Thin Films

Samples of $Ca(La_{1-x}Ce_x)_2S_4$ ($0 \leq x \leq 1$) were obtained from Prof. Macaluso's group to study their photoelectrochemical behavior. Porous films of $Ca(La_xCe_{1-x})_2S_4$ particles (geometric area = 1.0 cm^2) were deposited on Ti substrates from an aqueous suspension consisting of $Ca(La_xCe_{1-x})_2S_4$ particles, which were obtained by grinding the sulfide particles in an agate mortar together with a polyethylene glycol [PEG (Sigma Aldrich) - MW= 20,000)] water solution. The sulfide : PEG : water mass ratio of the resulting suspension was 1:1:5. First, the sulfide particles were prepared by grinding in an agate mortar for 20 min to minimize the particle size, then the PEG-water solution was added gently and mixed to make a homogenous aqueous suspension. Prior to film deposition, a pretreatment process was carried out for each substrate, the Ti substrates were cut into 3.0 × 1.0 cm pieces and chemically etched in 36% HCl for 10 min to remove organic contaminants, then washed ultrasonically with deionized water and dried under nitrogen

(N_2) gas. Ti was used as a substrate, because of its superior corrosion resistance. Also, Ti has very high conductivity compared with FTO or other TCO substrates. The geometrical area was defined by adhesive tape into 1.0 cm^2. A small aliquot of the obtained suspensions was spread uniformly using a glass rod onto the previously cleaned, etched, and sealed Ti substrate. After deposition of aqueous suspensions on the assigned area and drying at room temperature, the electrodes were annealed in a furnace at 350 °C for 30 min and subsequently at 450 °C for 30 min to improve adhesion of the sulfide compound to the Ti substrate. This process resulted in a uniform, homogeneous film of $Ca(La_xCe_{1-x})_2S_4$ that adhered well to the titanium substrates as shown in Figure 3.1. To further assess semiconductor characteristics of the thin films, photocurrent response measurements were performed using a Ti-supported $Ca(La_xCe_{1-x})_2S_4$ thin film electrode as photoanode in a three-electrode electrochemical cell.

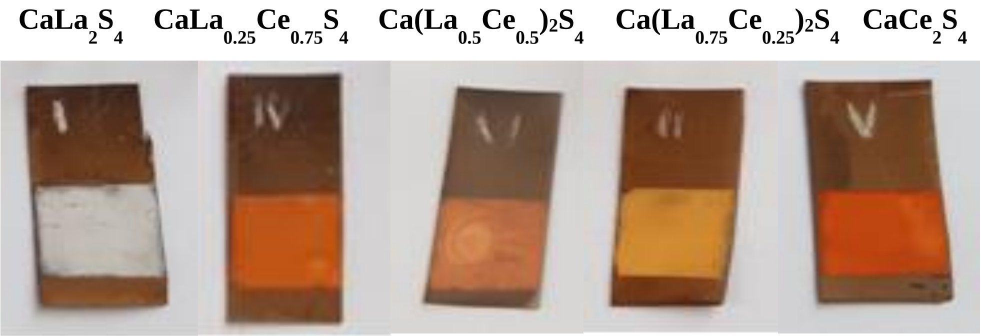

Figure 3.1 $Ca(La_{1-x}Ce_x)_2S_4$ thin films with x = 0.0, 0.25, 0.50, 0.75 and 1.0.

3.2 Copper (I) Oxide (Cu_2O)

For the electrodeposition of Cu_2O, 50 mM copper acetate [$Cu(CH_3COO)_2$ (Aldrich, 99% pure)] and 80 mM sodium acetate [$NaCH_3COO$ (Aldrich, 99% pure)] (with a pH of

5.0 ± 0.1 adjusted by concentrated acetic acid) were used. Double-distilled water (Corning Megapure) was used to prepare all solutions. All the chemicals were used as received without further purification.

3.2.1 Electrodeposition of Copper (I) Oxide

The electrodeposition of Cu_2O thin films[113,114] was carried out in a standard three-electrode chemical cell using CH Instrument potentiostat (Model CHI720C). Fluorine-doped tin oxide (FTO) conductive glass (MSE Pro^{TM}, surface resistivity: 15 Ω/sq) served as a working electrode (WE). A Pt foil and a Ag/AgCl/4M KCl electrode were used as the counterelectrode (CE) and reference electrode (RE), respectively. The electrodeposition solution was then transferred into the cell containing WE, CE, and RE. Prior to electrodeposition, FTO substrates were cut into 3.0 × 2.0 cm pieces using a glass cutter and then cleaned ultrasonically in the order: acetone, ethanol, and distilled water for 15 min in each solution. To probe the electrodeposition potential window for Cu_2O, linear sweep voltammogram was first recorded with FTO as a working electrode starting at + 0.2 V to -0.2 V at a scan rate of 5 mV/s (Figure 3.2). The cathodic reduction peak (peaking at -0.16 V) indicates the cathodic electrodeposition potential window (0.0 to -0.2 V) for metallic copper. Based on these data, the electrodeposition of Cu_2O thin films was performed potentiostatically on the FTO substrate at two different deposition potentials of 0.0 V and -0.1 V versus Ag/AgCl/4M KCl. The electrodeposition of thin films took place for 40 min and 25 min at potentials of 0.0 V and -0.1 V, respectively to approach the same thickness at room temperature (25°C).

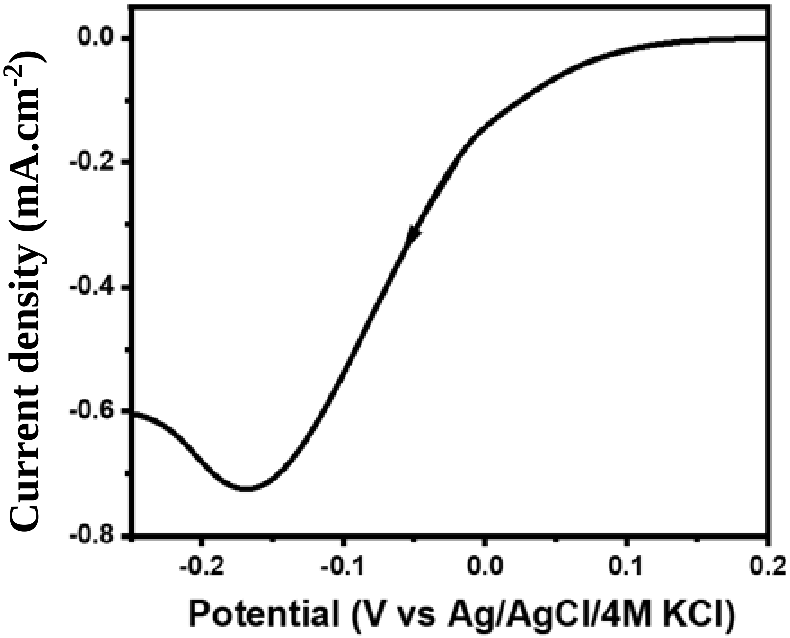

Figure 3.2 Linear sweep voltammograms for FTO in 50 mM copper acetate and 80 mM sodium acetate, 5 mV/s scan rate (pH: 5.0 ± 0.1).

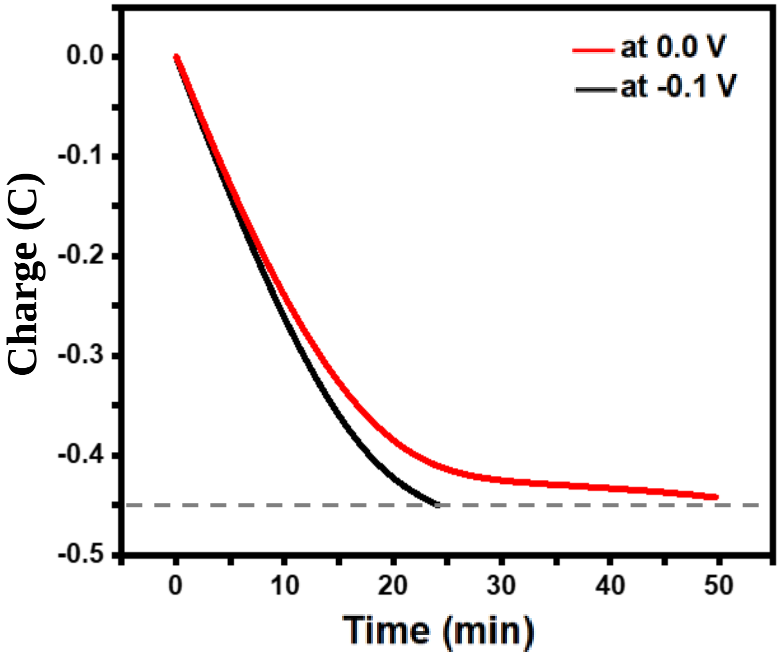

Figure 3.3 Potentiostatic electrodeposition of Cu_2O at 0.0 and -0.1 V in 50 mM copper acetate and 80 mM sodium acetate (pH: 5.0 ± 0.1), 5 mV/s scan rate.

The thickness of the synthesized thin films was controlled by adjusting the charge at 0.45 C for both films as shown in Figure 3.3. Through the potentiostatic deposition, a homogeneous and evenly coated brown layer gradually formed on the FTO substrate. After deposition, the films were rinsed gently with deionized water and dried in air for studying further physical characterization and PEC behavior.

3.2.2 Sample Crystallinity

Characterization of the electrodeposited synthesized oxides was carried out using X-ray diffraction (XRD).[115,116] X-ray diffraction (XRD) of the electrodeposited synthesized samples was performed on a high-resolution PANalytical Empyrean diffractometer equipped with a PIXcel3D detector. Diffractograms used a 2θ step size of 0.02° between 25°-70° with a dwell time of 1.25 s. A Cu Kα radiation source with λ = 1.5406 Å was used for XRD analysis of the prepared films. Further analyses of the XRD patterns used the X-pert Highscore software.

3.3 Titanium Dioxide and Tungsten Trioxide (TiO_2 and WO_3)

Either titanium foil (Alfa Aesar, 0.25 mm thick, 99.95%) or tungsten foil (Alfa Aesar, 0.25 mm thick, 99.95%) was used as the substrate for growth of nanoporous oxide films. Nanostructured TiO_2 film was grown in an anodization solution containing 0.15 M ammonium fluoride [NH_4F (Aldrich, 99% pure)] with glycerol : H_2O (90 : 10). Sodium fluoride [NaF (Alfa Aesar, 99% pure)] was used to prepare an electrolyte solution for electrochemical anodization of W. The use of viscosity modifiers such as glycerol in the media was reported[117] to afford smooth nanotubes of TiO_2 by suppressing local concentration fluctuations and pH bursts during anodization.

3.3.1 Electrochemical Anodization of Ti and W Thin Films[30]

Strips were cut into 3.0 × 1.5 cm pieces and mechanically polished to mirror finish using silicon carbide sandpaper of successively finer roughness (220, 320, 600, 1200, 1500, and 2000 grit) followed by alumina micropolish suspension down to 0.05 μm. They were then cleaned in three 5 min steps in ultrasonicated acetone, 2-propanol, and finally ultrapure water and then dried in flowing N_2 stream and used immediately. Anodization was performed in a two-electrode cell setup equipped with a 420X Power Supply (The Electrosynthesis Company, Inc., NY). The electrochemical cell was connected in series to a variable resistor (100 kΩ) that was decreased to zero to simulate a voltage ramp of ~ 0.2 V/s, and then the voltage was held at the preselected level for anodization times varying from 1 to 3 h. A metal foil (either Ti or W) pressed between a set of O rings in the electrochemical cell, leaving 0.78 cm^2 exposed to the electrolyte, served as the working electrode (anode) and platinum as a cathode (Figure 3.4). The electric contact was located on the backside of the sample. Titanium dioxide films were anodically grown at a voltage of 20 V for 3 h and the voltage was held at 55 V for tungsten trioxide for an anodization duration of 3 h. A schematic diagram for the electrochemical anodization of Ti and W is shown in Figure 3.4.

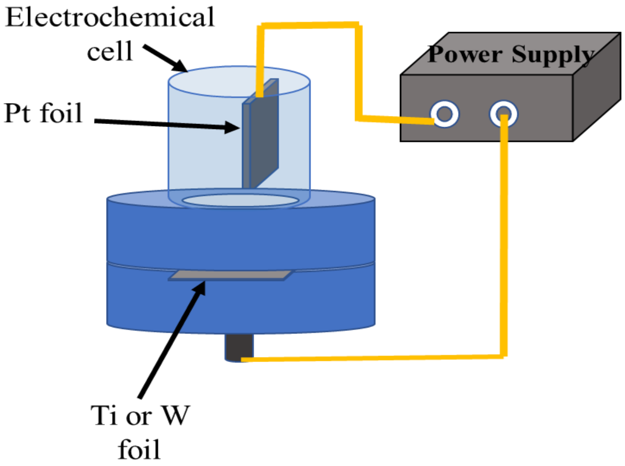

Figure 3.4 Schematic diagram for electrochemical anodization of Ti and W.

As elaborated elsewhere,[30] anodization voltages in the 20-40 V range resulted in uniform and self-organized nanotubes, while both lower and higher voltages resulted in disorganized nanoarchitectures. Extensive carrier recombination was noted for anodization voltages higher than 20 V for TiO_2. As in the case of WO_3, higher voltages (e.g., 55 V) with lower time yielded a uniform smooth film. At longer times, the pore organization was disrupted and the morphology changed to a disordered appearance and low voltages gave rise to nanocube clusters.[30] Once the oxide films were grown, the anodized metal foils were removed from the O-ring assembly and carefully washed by immersion in deionized water and were annealed at 350 °C for 3 h in an air furnace.

3.4 Copper (II) Oxide (CuO), Silver Vanadate ($AgVO_3$), and Copper Bismuth Oxide ($CuBi_2O_4$)

Bismuth nitrate, $Bi(NO_3)_3\cdot 5H_2O$ (≥98.0%), copper nitrate, $Cu(NO_3)_2\cdot 2.5H_2O$ (98.0%), potassium perchlorate, $KClO_4$ (99.0−100.5%), and dimethyl sulfoxide, $(CH_3)_2SO$ (DMSO (≥99.0%)) were purchased from Sigma-Aldrich. Electrodeposition of CuO was performed in a 40 mM copper nitrate, $Cu(NO_3)_2 \cdot 2.5H_2O$ (Alfa Aesar) solution. Silver nitrate, $AgNO_3$ (99.9%) and ammonium vanadate, NH_4VO_3 (99.0%) were used as Ag and V source, respectively, for the electrodeposition of $AgVO_3$. Acetonitrile, CH_3CN (Sigma-Aldrich) and double-distilled water (H_2O) were used as solvent. Tetrabutylammonium perchlorate, $CH_3CH_2CH_3CH_2)_4N(ClO)_4$ and potassium nitrate, KNO_3 (Alfa-Aesar) were also used to prepare electrolyte solutions. Sodium dodecyl sulfate, $CH_3(CH_2)_{11}SO_4Na$ (Sigma-Aldrich) was used as binder. All the chemicals were used as received without further purification.

3.4.1 Electrodeposition of $CuBi_2O_4$, CuO, and $AgVO_3$

The electrochemical cell set up was the same as that described above in section 3.2.1. Electrodeposition of $CuBi_2O_4$ was carried out by passing 0.04 C/cm^2 at $E = -1.5$ V vs Ag/AgCl/4 M KCl, followed by a resting time of 2 s. This cycle was repeated 10 times to pass a total charge of 0.40 C/cm^2. The Cu/Bi films were heated at 450 °C for 3 h in air (ramping rate = 3.5 °C/min) to form $CuBi_2O_4$ films. Cathodic electrodeposition of CuO and $CuBi_2O_4$ was done as per details given elsewhere.[50] A two-step approach was used for the electrosynthesis of $AgVO_3$. The silver metavanadate thin film was prepared by sweeping the potential from 0.70 V to 0.90 V. In the first step, a silver thin film was deposited cathodically from $AgNO_3$ solution. In the second step, the silver thin film was stripped anodically in NH_4VO_3 solution to generate Ag^+; and subsequent in situ precipitation with VO_3^- to yield $AgVO_3$ thin film on the substrate as per details given elsewhere in our related work.[31]

3.5 Photoelectrochemical (PEC) Characterization

A similar electrochemical set up was used with 0.1 M sodium sulfate, Na_2SO_4 (Alfa Aesar, 99.9%) as supporting electrolyte and 0.1 M sodium formate, HCOONa (Alfa Aesar, 99.9%) was added as hole scavenger. The electrolyte solution was purged with ultrapure N_2 for 15 min prior to the photovoltammetry measurements. For photovoltammetry, the potential was swept at a low scan rate of 5 mV/s with the dark/illuminated cycles alternated in 5 s intervals with a manual chopper. Figure 3.5 shows a schematic of the photoelectrochemistry experiment setup. The PEC measurements used a full spectrum solar simulator (400W Xe-arc lamp, Newport/Oriel instruments) as a radiation source, whose output was manually interrupted to examine both the "dark" current and photocurrent. The electrochemical cell was placed ~ 20 cm away from the radiation source. The nominal photon flux at the electrode surface was 300 mW/cm^2 (measured using a radiant power meter [Newport 70260) combined with a probe (Newport, 70268)]. The PEC measurements were carried out at ambient temperature. Prior to the PEC measurements, the Ti or W foils were masked with adhesive tape to prevent any interference of conductor or metal with the electrolyte. For all the synthesized *n*-type semiconductor thin films ($Ca(La_{1-x}Ce_x)_2S_4$, Cu_2O, TiO_2, and WO_3), the PEC solutions included Na_2SO_4 with HCOONa added as a hole scavenger (capturing the photogenerated holes from the electrodes).

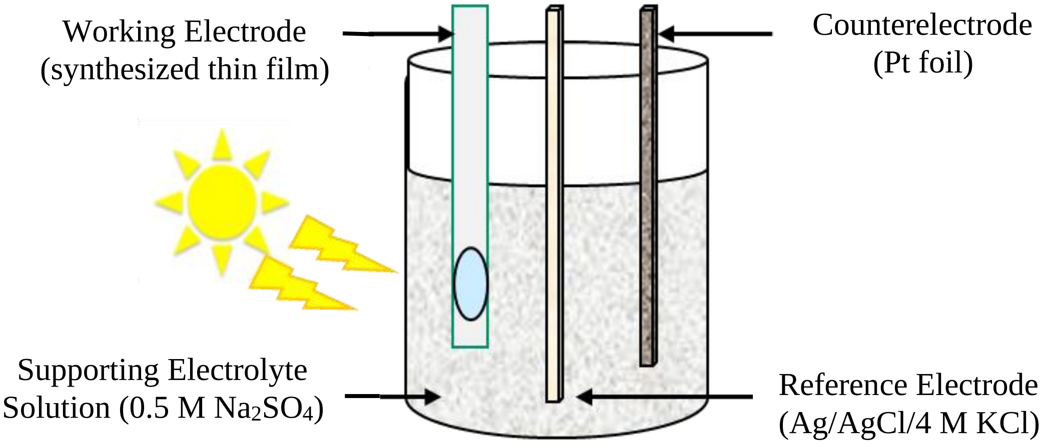

Figure 3.5 Schematic diagram of the photoelectrochemistry experiment setup.

The same electrochemical solutions contained Na_2SO_4 with dioxygen purged as an electron acceptor for synthesized *p*-type oxide semiconductor thin films during the photovoltammetry measurements. Having established that $AgVO_3$ has reasonable electrochemical stability in a non-aqueous electrolyte,[31] PEC experiments were conducted using 0.2 M tetrabutylammonium perchlorate, $(CH_3CH_2CH_3CH_2)_4N(ClO)_4$ (TBAP, Alfa Aesar) in acetonitrile, CH_3CN (Sigma-Aldrich). The electrolyte was purged with dioxygen (as an electron acceptor) during the photovoltammetry measurements.

3.5.1 Photoelectrochemical Stability of *n*-$CaCe_2S_4$

The PEC data bearing on the photostability of *n*-$CaCe_2S_4$ in aqueous sulfite and polysulfide media were obtained and compared. The aqueous polysulfide consisting of 1 M Na_2S, 1 M S and 1 M NaOH was used to kinetically stabilize *n*-$CaCe_2S_4$ photoanodes from undergoing anodic corrosion. A Pt wire and Ag/AgCl/4 M KCl were used as the counterelectrode and reference electrode, respectively. In all the cases, nitrogen gas was purged through the solutions for de-aeration. Throughout the measurements, a radiation source of 400 W Xe lamp (Newport) was kept at fixed distance from the cell (20 cm) for 90 min continuously. Anodic photocurrent stability of $CaCe_2S_4$ electrode was attained by photocurrent-time profiles in two different solutions, (i) aqueous polysulfide (1 M Na_2S, 1 M S and 1 M NaOH) and compared with (ii) 1 M Na_2SO_4 (as supporting electrolyte) with 0.1 M Na_2SO_3 added as hole scavenger. In both cases, the photoanode was poised at +0.6 V vs. Ag/AgCl/4 M KCl.

3.6 Electrochemical Characterization of *n*- and *p*-type Oxide Semiconductors in the Dark

Measurements were carried out using the electrochemical cell set up coupled to a potentiostat same as defined above. Potassium ferricyanide, $K_3Fe(CN)_6$ (Sigma-Aldrich) and potassium ferrocyanide, $K_4Fe(CN)_6$ (Sigma-Aldrich) were used as a redox couple in 0.5 M potassium nitrate, KNO_3 (Alfa Aesar) as supporting electrolyte. Ferric nitrate, $Fe(NO_3)_3$ (Sigma-Aldrich) and ferrous sulfate, $FeSO_4$ (Sigma Aldrich) were used as another redox couple in 0.5 M KNO_3. Cathodic currents (forward bias) were measured for TiO_2 and WO_3 by applying bias potential more negative than the flat band potential for both redox couples. The same electrochemical measurements were carried out for as-synthesized *p*-type oxide semiconductors. The anodic dark currents were evaluated for $CuBi_2O_4$, CuO, and $AgVO_3$ for both redox couples by applying a bias potential more positive than the flat band potential. The results of these measurements are discussed in the next chapter.

CHAPTER 4

RESULTS AND DISCUSSION

4.1 Photoelectrochemical Properties

Photoelectrochemical properties of selected *n*- and *p*- type semiconductors are analyzed in this section. In the case of *n*-type (*p*-type) semiconductors, the minority carriers are holes (electrons). The photogenerated holes oxidize solution species which results in a photoanodic current flow and promotes photooxidation reactions. In *p*-type semiconductors, photogenerated electrons are responsible for photocathodic current flow.

4.1.1 *N*-type Ca $(La_{1-x}Ce_x)_2S_4$ Thin Films

The photoelectrochemical properties of $Ca(La_{1-x}Ce_x)_2S_4$ $(0 \leq x \leq 1)$ thin film electrodes were evaluated by means of LSV under intermittent light incidence, and compared to the two end members. Photovoltammetry measurements were recorded at a low scan rate of 5 mV/s with the sweep potential applied from -0.7 V to +1.0 V. A manual chopper was used to create 5 s interval dark/illuminated cycles. As shown in Figure 4.1, anodic photocurrents were observed for all samples when polarized at $E > E_{eq}$ consistent with *n*-type semiconductor behavior. The spiked transient profiles in Figure 4.1 associated with charge carrier recombination reverted to a rectangular one as the samples were increasingly reverse-biased in the positive potential regime, indicating that charge carrier $(e^{-} - h^{+})$ recombination was suppressed at higher overpotentials. While the lowest current density was observed for $CaLa_2S_4$, higher current densities were measured for cerium-containing samples.

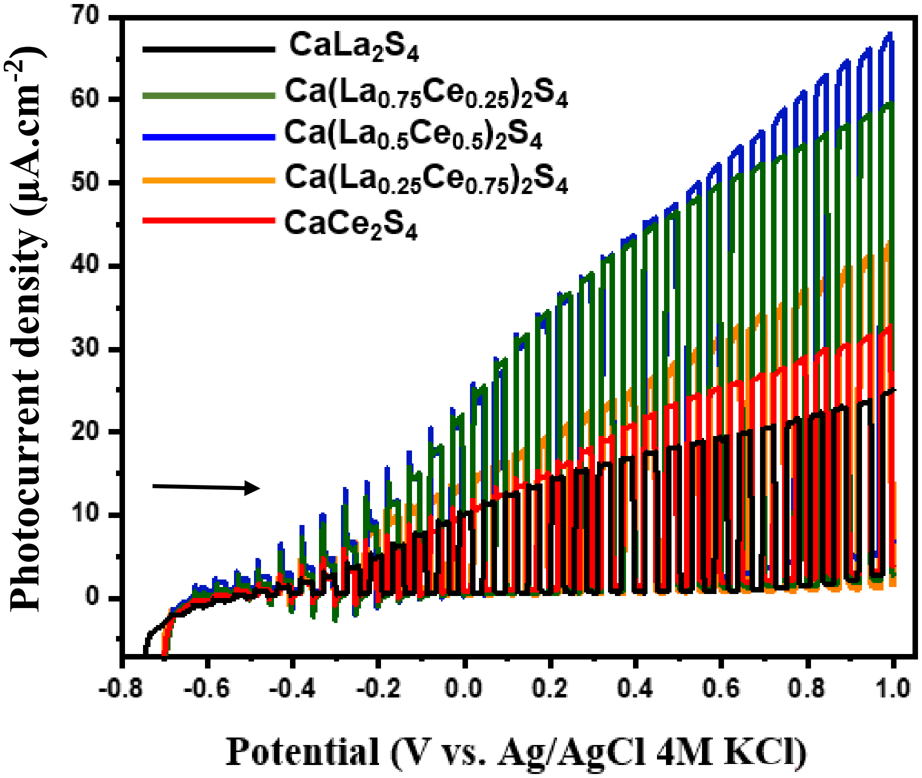

Figure 4.1 Photocurrent measurements under intermittent irradiation of thin film electrodes, immersed in aqueous 0.1 M Na_2SO_4 solution containing 0.1 M Na_2SO_3 as hole scavenger.

As Ce was progressively substituted for La, higher current densities were measured. The highest current density (at a fixed potential, 1.23 V vs. RHE) was observed for x = 0.50 as shown in Figure 4.2. While incorporation of Ce was beneficial up to a point, higher amounts were clearly deleterious, and in fact, $CaLa_2S_4$ exhibited inferior photoactivity relative to the other samples in Figure 4.2. Clearly, other factors (bulk carrier transport, surface electrocatalytic activity) must play a role here. The relationship between the photocurrent (I_{ph}) at 1.23 V vs. RHE and cerium stoichiometry is illustrated in Figure 4.2. The I_{ph} is found to improve as Ce was progressively substituted for La, reaching a peak around x = 0.50. Continued increase of Ce content then causes decline in photocurrent.

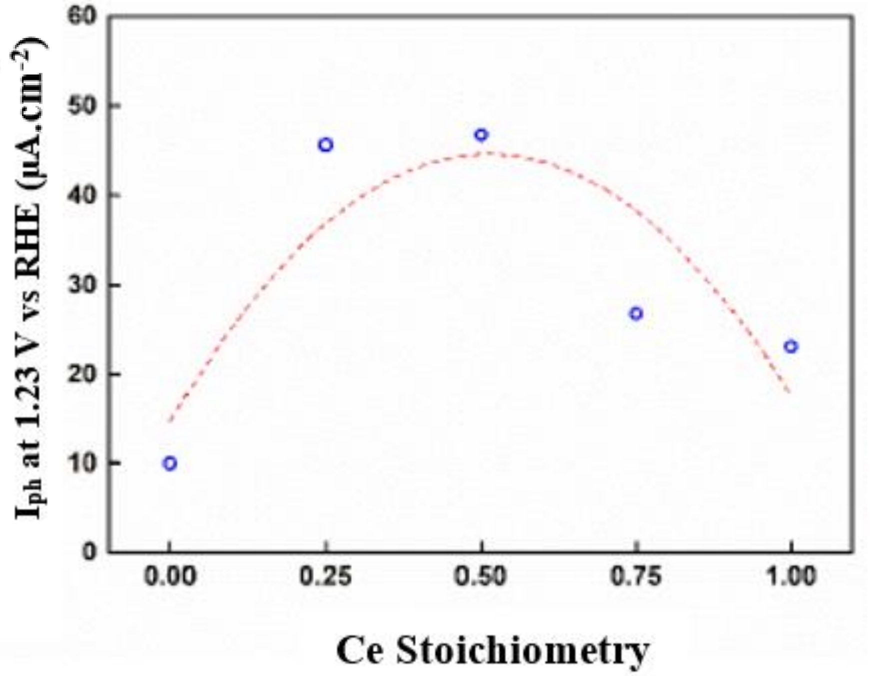

Figure 4.2 Relationship between photocurrent at 1.23 V vs RHE and cerium stoichiometry of $Ca(La_xCe_{1-x})_2S_4$ compounds. The dashed line is simply drawn as a guide to the data trend.

The increase of I_{ph} at lower Ce content (with partially filled *f*-orbital) mainly comes from a new energy level in the host material. This changes the original electronic movement route, and more electrons diffuse to the surface, which enhances the photocurrent response.[118,119] It can also be attributed to a shrinking of the band gap due to reduced impact of *d* electronic states (La), which limit carrier transport, relative to $CaLa_2S_4$.[26] On the other hand, when additional Ce was introduced into the films, it is possible that oxygen crystal defects are produced, as has been observed previously by other groups at high Ce content.[119,120] Although some amount of defects can impart beneficial properties, such as improved conductivity, these defects also result in the capture of photoinduced electrons and holes resulting in an adverse impact on photocurrent. High Ce content may cause the formation of a large amount of defects, which would hinder electron transfer, increase recombination, and therefore weaken the performance of PEC films.[119] The *n*-$CaCe_2S_4$ decomposition potential is in close proximity to its band edges, as shown in Figure 4.3. While this suggests that the compound is thermodynamically susceptible to anodic photocorrosion, photovoltammetry measurements presented in the following section, do not show degradation of photocurrent over time in the presence of sulfite and polysulfide redox couples.

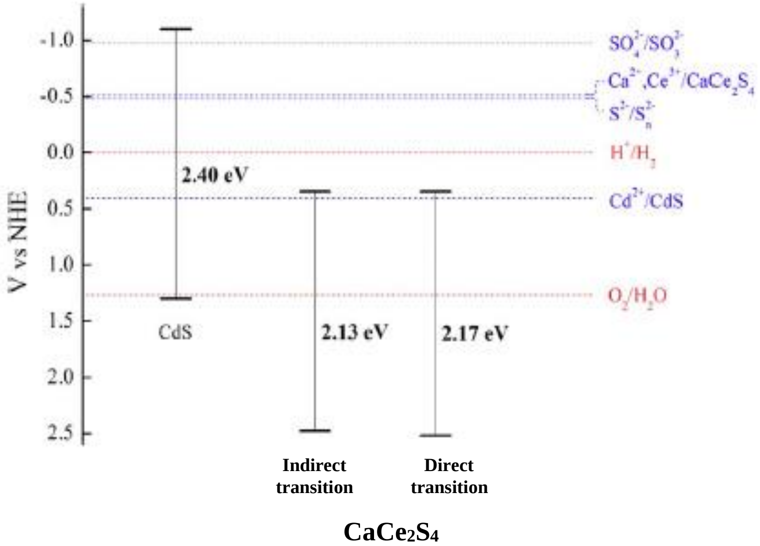

Figure 4.3 Valence band edge and conduction band edge locations for n-$CaCe_2S_4$. [Sotelo, P. *et al*. Ternary Rare Earth Sulfide $CaCe_2S_4$: Synthesis and Characterization of Stability, Structure, and Photoelectrochemical Properties in Aqueous Media. *J. Solid State Chem.* 2018, *262*, 149–155.].

4.1.2 Photoelectrochemical Stability of *n*-type $CaCe_2S_4$ Thin Film

Aqueous polysulfide redox electrolyte is commonly used to kinetically stabilize metal chalcogenide photoanodes from undergoing anodic corrosion.[121,122] For example, the band edges of a benchmark compound, CdS, are compared against the sulfide/polysulfide redox potential in Figure 4.3 with its decomposition potential. The decomposition potential for the ternary chalcogenide ($CaCe_2S_4$) was also calculated from the 8-electron reaction.[123] The relative ordering of the decomposition potential and the sulfite and polysulfide redox couples for this compound is shown in Figure 4.3. As discussed by previous authors,[124,125] the relative dispositions of the two redox couples suggest that hole transfer to polysulfide kinetically offsets the (presumably slow) hole attack of the semiconductor itself leading to suppression of photocorrosion.[123] While this compound is certainly thermodynamically susceptible to anodic photocorrosion, our data suggest that both the sulfite and polysulfide redox couples are able to kinetically suppress it (see Figures 4.4 and 4.5).

Figure 4.4 contains PEC data bearing on the photostability of *n*-$CaCe_2S_4$ in aqueous sulfite and polysulfide electrolytes. Firstly, the hole transfer kinetics are significantly improved in polysulfide as compared to the sulfite redox electrolyte. This can be gauged by comparing the relative photocurrent levels in the photovoltammetry data in Figure 4.4. Thus the photocurrents in polysulfide (blue trace) are ~ 2-fold higher relative to sulfite (red line), underlining the faster kinetics in the former case. The Ti (substrate) data in Figure 4.4 constitute a blank, indicating that the evolving native oxide layer on Ti has insignificant photoactivity under the irradiation conditions relevant to this study. Figure 4.5 contains photocurrent-time profiles for the Ti|$CaCe_2S_4$ photoanode at a fixed reverse bias potential in the two electrolytes (polysulfide and sulfite). In all the cases, nitrogen gas was purged through the solutions for de-aeration, and the noise from this is especially visible on the upper trace in Figure 4.5.

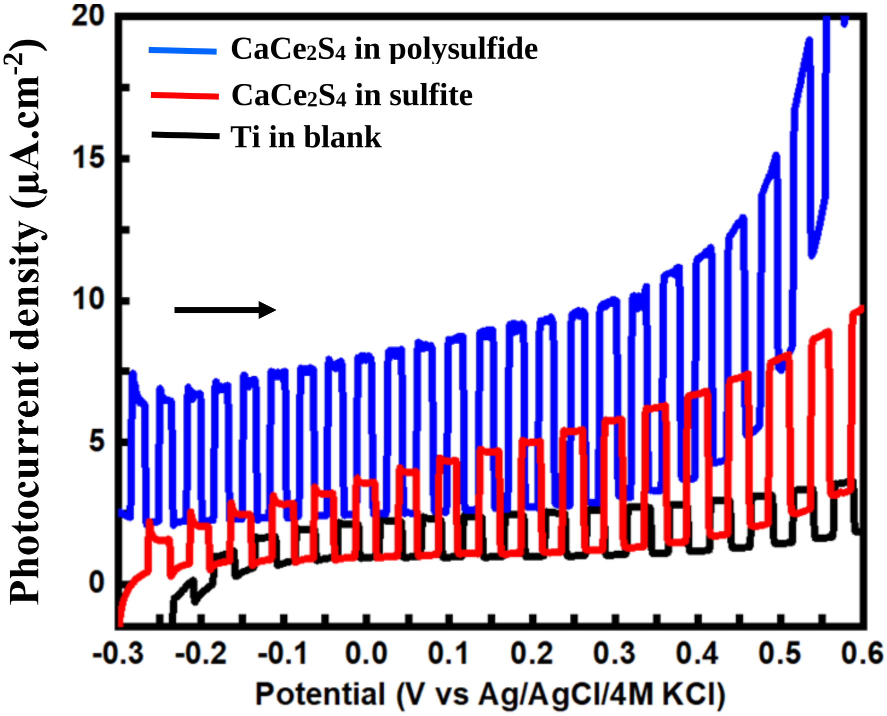

Figure 4.4 Photovoltammetry of Ti|CaCe$_2$S$_4$ electrode at 5 mV/s scan rate with intermittent irradiation in polysulfide (blue) and sulfite (red) redox electrolytes.

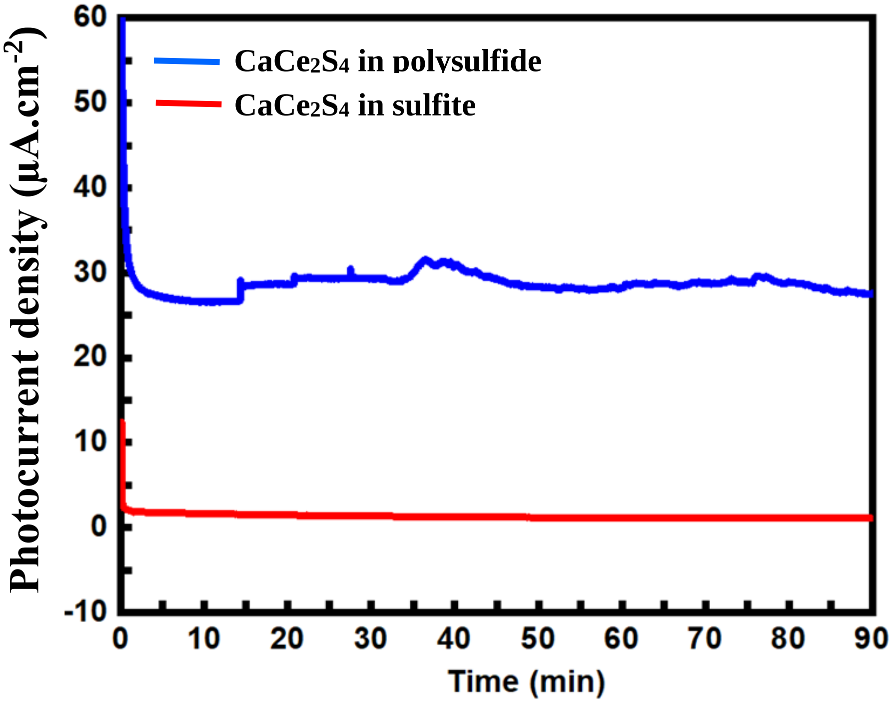

Figure 4.5 Anodic photocurrent versus time in the two electrolytes with the photoanode poised at +0.6 V vs. Ag/AgCl/4 M KCl.

The photocurrents are stable and horizontal with respect to time (after an induction period of ~ 2 min) indicating that the photoanode surface is not undergoing significant photocorrosion. An induction period is commonly observed in such experiments[126] and is attributable to surface exchange of sulfide with solution species.

4.1.3 Bipolar (*n*- and *p*-type) Photoactivity of Cu_2O

The origin of the intrinsic *n*-type conductivity of Cu_2O is a matter of debate,[127,128] yet it has been gained substantial interest. In the literature, most of the investigations have proposed that oxygen vacancy (V_O) is the electron donating source in explaining the experimental results of *n*-type behavior. For example, Han *et al.*[129] found that *n*-type Cu_2O thin films can be produced when the deposition potential is higher than -0.05 V in acidic solutions. They have shown this trend by zero-bias photocurrent measurements. They specified that Cu^{2+} reduction process results in the growth of Cu_2O accompanied by high oxygen vacancies. Wang *et al.*[114] have reported a similar phenomenon in which the electrodeposited *n*-type Cu_2O films were converted to *p*-type behavior covered with a layer of CuO after they were annealed at 400 °C in air. Kalubowila *et al.* [113] synthesized *n*-Cu_2O by depositing copper (Cu) thin film on the substrate prior to the Cu_2O film deposition. They have found this approach can remove/minimize the additional *p*-type photocurrent observed in Cu_2O thin films and improve the *n*-type behavior in PEC performance. The copper (I) oxide most commonly occurs as a *p*-type semiconductor and this behavior is attributed to the formation of Cu vacancies in the lattice.

On the other hand, thermodynamic calculations[130] have shown that oxygen vacancies or Cu anti-sites cannot provide donor levels within the oxide bandgap. Therefore, the origin of the *n*-type conductivity claimed for electrodeposited Cu_2O in many previous studies, remains problematic. Indeed, to quote previous authors:[130] "The identity of true source being responsible for the *n*-type conductivity of undoped Cu_2O (sic) will be a critical issue."

On the other hand, the photocurrent polarity (PCP) data and interpretations presented below offer a way out of this dilemma. The photoactivity of electrodeposited Cu_2O films is shown in Figures 4.6 and 4.7. These figures illustrate the bipolar nature of the PCP observed for electrodeposited Cu_2O film samples. Two different deposition potentials (0.0 and -0.1 V) were used to prepare the films as shown in the experimental chapter (Figure 3.3). The photovoltammograms in Figure 4.6 show cathodic photocurrent spikes in both cases, diagnostic of *p*-type behavior. Note that the potential was scanned in the negative direction consistent with a reverse biased situation. On the other hand, when the scan was initiated in the opposite direction, the results in Figure 4.7 were obtained.

Now, the PCP excursions in Figure 4.7 are photoanodic in nature. Interestingly, the magnitude of these photoanodic spikes is very dependent on the potential at which the films were initially electrodeposited, being more magnified when the film was made at a more negative potential (-0.1 V). Similar profiles as in Figure 4.7 appear in previous studies in the literature.[113,114] Also worthy of note in Figure 4.7 is the dark anodic wave (peaking at $\sim$0.25 V) and the rising anodic background on which the photocurrent spikes are superimposed. This dark envelope is higher for the sample electrodeposited at the more negative potential. To better understand the cause of this bipolar photoactivity, film characterization was carried out by XRD for the prepared Cu_2O films (Figure 4.8).

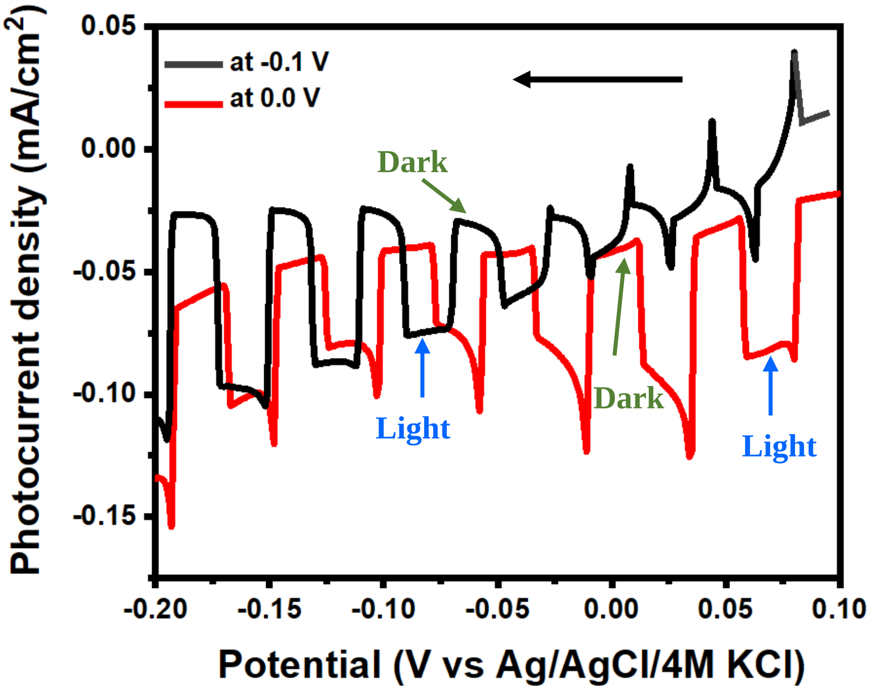

Figure 4.6 Photovoltammograms in reverse bias regime for two electrodeposited film samples in oxygenated 0.5 M sodium sulfate medium.

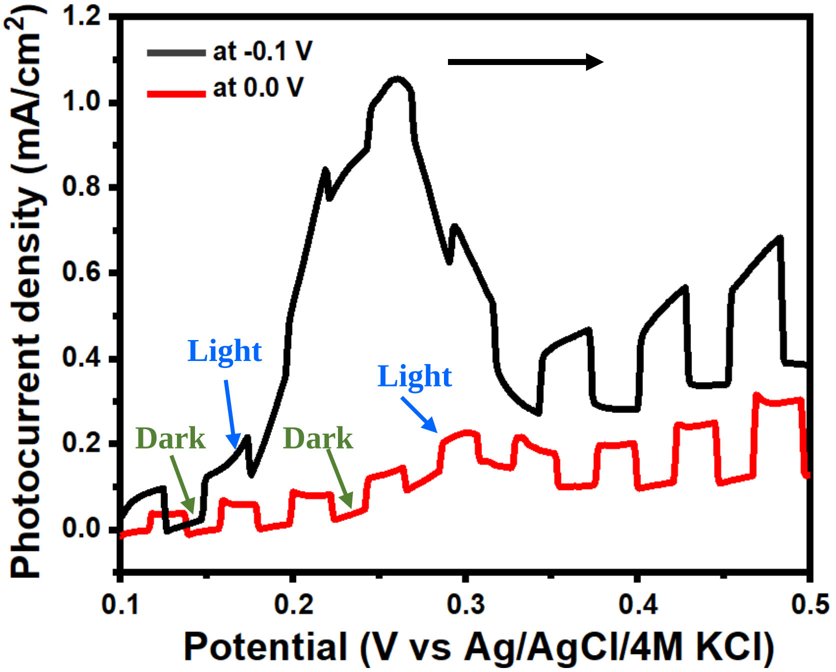

Figure 4.7 Photovoltammograms in forward bias regime for two electrodeposited film samples in oxygenated 0.5 M sodium sulfate medium.

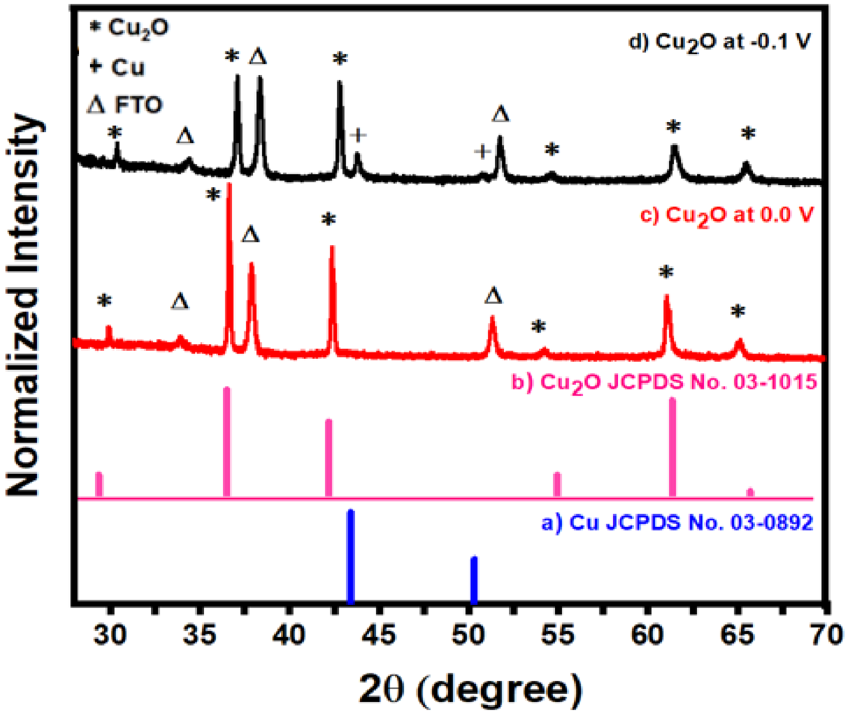

Figure 4.8 XRD patterns of (a) reference Cu, (b) reference Cu_2O, (c) as-prepared film at 0.0 V and (d) as prepared film at -0.1 V.

X-ray diffraction data on the electrodeposited film samples (Figure 4.8) reveal the enhanced co-deposition of metallic Cu phase as the deposition potential is made more negative. It is important to note that, during the electrodeposition process, the possible reactions are:

$2Cu^{2+} + H_2O + 2e^- \rightarrow Cu_2O + 2H^+$ $E^\circ = + 0.295$ V *vs.* SHE at pH = 5.0 [4.1]

$Cu^{2+} + 2e^- \rightarrow Cu$ $E^\circ = + 0.340$ V *vs.* SHE [4.2]

When the overpotential increased with the decrease of applied potential, Reactions [4.1] and [4.2] could occur thermodynamically. However, Reaction [4.2] is thermodynamically more favorable than Reaction [4.1] due to its higher overpotential at a certain reduction potential. Hence, Reactions [4.1] and [4.2] can occur simultaneously. The Cu phase, co-deposited from Reaction [4.2] may be anodically stripped, for example, in 0.1 M KNO_3 solution at + 0.25 V for 20 min. The anodic stripping was continued till no anodic currents were observed from the residual metallic copper (see Figure 4.9).

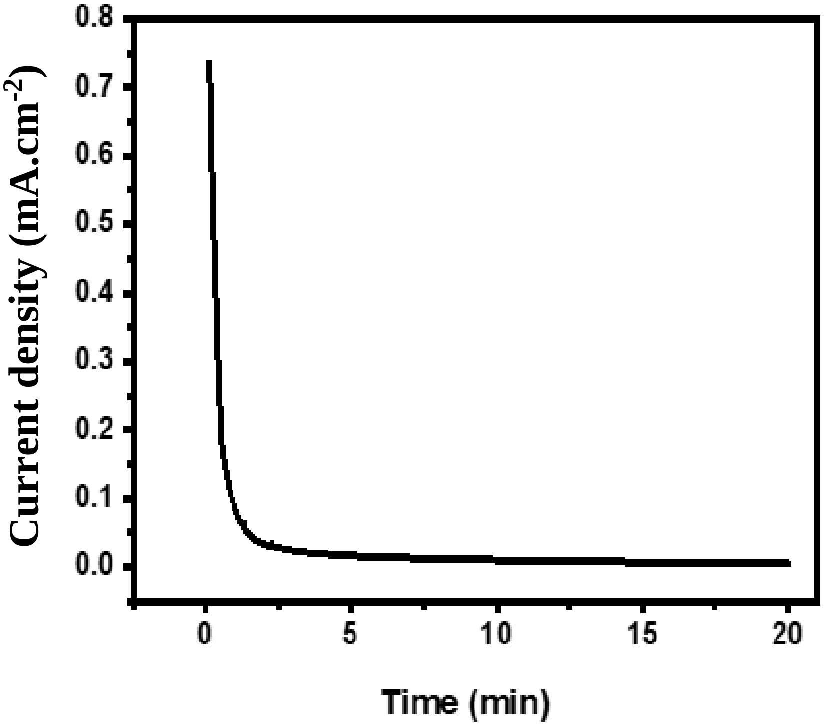

Figure 4.9 Anodic stripping at +0.25 V for 20 min in 0.1 M KNO_3 for the oxide sample electrodeposited at -0.1 V.

The anodically stripped films were then characterized by XRD for proof of removed electrodeposited metallic Cu (Figure 4.10). Photocurrent response measurements were then performed using the anodically stripped Cu_2O thin films (Figure 4.11). The followed photocurrent measurements validate the possible contributory factor in many previous studies that have (erroneously) identified *n*-type semiconductor behavior in electrodeposited copper oxide films.[113,114,129] X-ray diffraction data (see Figure 4.10, scan d) support the notion that the Cu co-phase has been removed from the film.

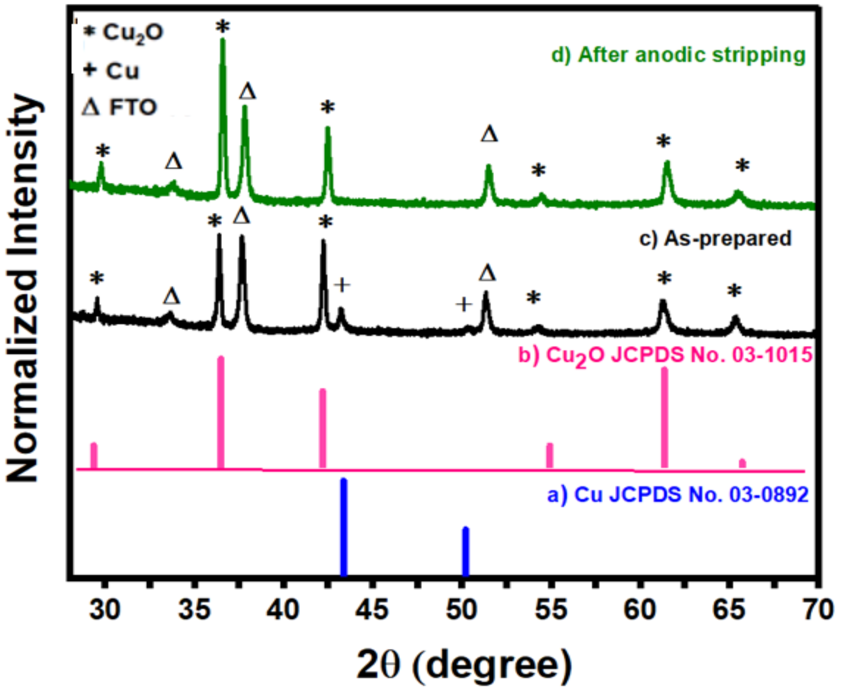

Figure 4.10 XRD data showing the result of anodic stripping of the Cu phase from the oxide sample electrodeposited at -0.1 V.

Interestingly, a repeat of the PEC experiments as in Figure 4.7 yielded the data in Figure 4.11. After anodic stripping, the Cu peaks disappeared compared to the as-prepared thin films. The anodic photoactivity of thin film electrodes shows significantly less dark currents with less current densities compared to the photovoltammetry measurements as in Figure 4.7. The anomalous anodic photocurrent spikes are virtually gone after stripping off the Cu phase, and as a result, the anodic photocurrent decreases significantly. Traces of Cu below the detection limit of XRD are presumably still present given the residual spikes in Figure 4.11.

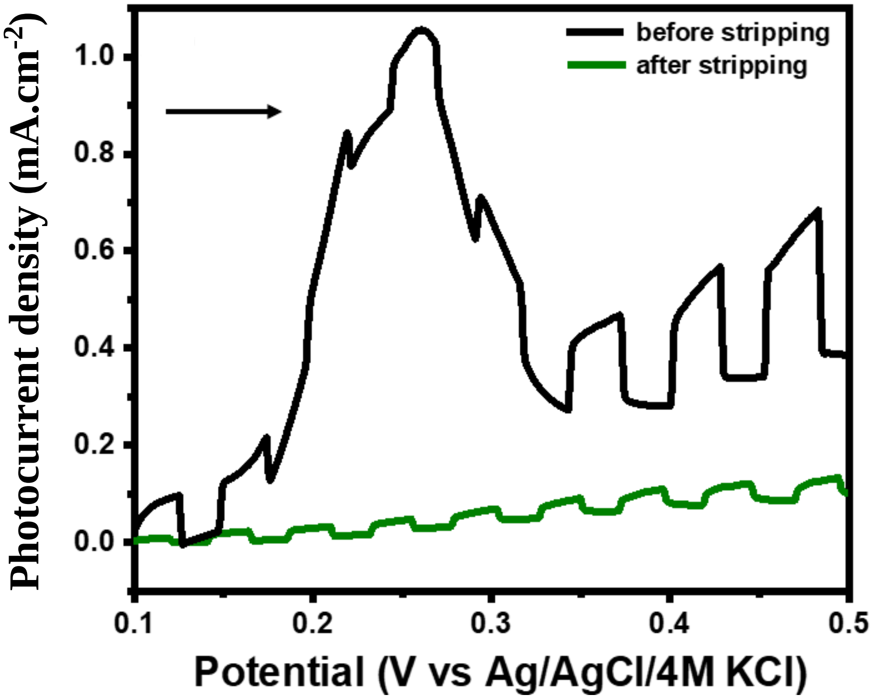

Figure 4.11 Photovoltammograms for copper oxide films electrodeposited at -0.1 V before (black) and after (green) anodic stripping of the Cu phase.

The photocurrent after anodic stripping thin films implies that *n*-type behavior of Cu_2O comes from the presence and oxidation of metallic copper that deposited as a byproduct along with Cu_2O during potentiostatic electrodeposition. This is supported by the XRD patterns above. To explore the implications of this trend on the conductivity of Cu_2O films, anodic stripping was performed at different times of 0.5, 5, 10, 15, and 20 min. By increasing the anodic stripping time, total charge increased, indicating the removal of the relative content of metallic Cu increased. The anodic PCP signals were inversely correlated with the amount of Cu in the film as shown by the plot in Figure 4.12.

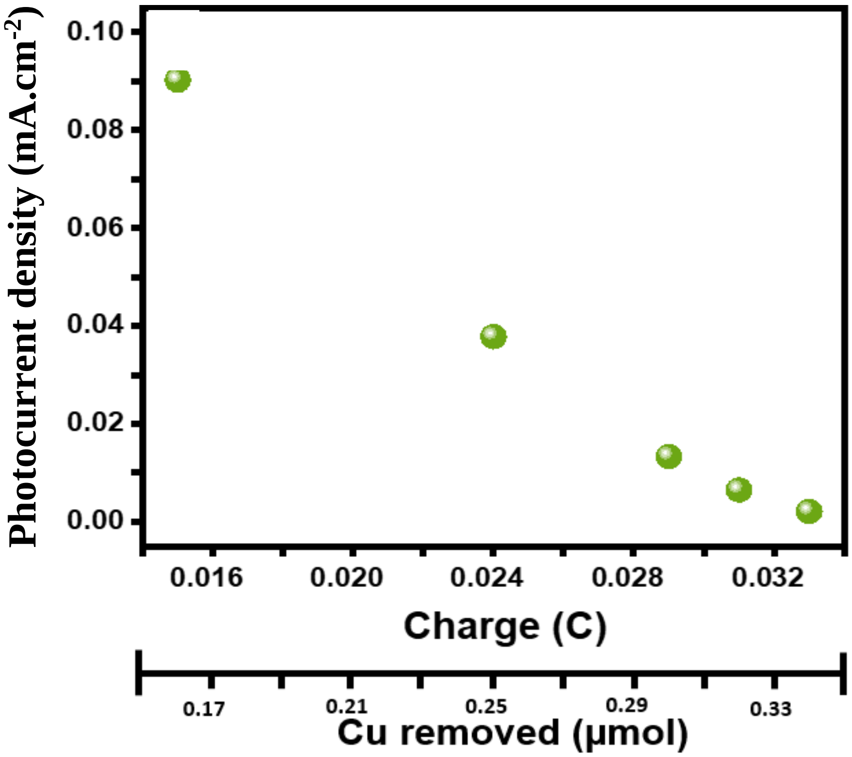

Figure 4.12 Correlation of the anomalous photoanodic spike with the amount of Cu in the film.

To translate the stripping charge to the amount of copper removed, Faraday's law (see Eq. 4.3) was invoked with the reasonable assumption of 100% coulombic efficiency for the stripping process and an electron stoichiometry of 1 for the process: Cu → Cu^+.

$$Q = nFN \qquad [4.3]$$

Q is total charge (C), n is number of electron per mole, F is Faraday's constant (96485 C/mol), and N is the moles of analyte. After determining the moles of Cu removed from the film, one can calculate the ratio of remained Cu/Cu_2O by assuming that in t = 0, the amount of Cu deposited on the film was the same as the amount removed (0.34 µmol) in

20 min. The Cu/Cu_2O ratio changed from an initial value of 0.142 to 0.077 (30 s), 0.037 (5 min), 0.016 (10 min), and 0.008 (15 min) before decaying to zero at t = 20 min.

Most importantly, it is worth underlining at this juncture, that in at least three of the prior studies,[113,114,129] data such as those in Figures 4.7 and 4.11 led the authors to attribute *n*-type conductivity to their copper oxide samples. Accepting for the moment that the as deposited copper oxide films are *p*-type, the PCP profiles in Figure 4.6 may be easily rationalized. The photogenerated minority carriers (electrons for a *p*-type semiconductor) are driven to the interface by the imposed reverse bias potentials where they are utilized for reduction of dissolved electrolyte species (e.g., dioxygen). On the other hand, when the bias potential is swept in the forward bias (positive) direction as in Figures 4.7 and 4.11, the majority carriers (holes) are driven to the interface. If an oxidizable agent such as Cu is present in the film, an anodic current will be the result as seen in Figures 4.7 or 4.11 (see also Eq. 4.4):

$$Cu + h^+ \rightarrow Cu^+ \qquad E^\circ = +0.52 \text{ V vs. SHE} \qquad [4.4]$$

The (anomalous) anodic "photocurrent" spikes in Figures 4.7 and 4.11 may be attributed to photoconductive enhancement of current flow as a result of the markedly lower electronic resistivity of metallic copper relative to copper oxide (~1.67 μΩ cm for Cu vs. ~104 Ω cm for Cu_2O, Refs. 131, 132). Another complication arises from the possible photocorrosion of Cu_2O:

$$Cu_2O + 2H^+ + 2e^- \rightarrow 2Cu + H_2O \qquad [4.5]$$

$$Cu_2O + 2OH^- + 2h^+ \rightarrow 2CuO + H_2O \qquad [4.6]$$

Reaction [4.4] is a majority carrier (*i.e.*, hole) driven process and the copper (II) oxide product can exhibit *n*-type behavior accounting for the photoanodic spikes observed in Figures 4.7 and 4.11. In fact, the copper oxide example in this study shows that the presence of an unwanted impurity phase such as Cu in the electrodeposited film sample may give rise to anomalous PCP signals that may be misinterpreted and mistakenly assigned to the conductivity type of the semiconductor phase. The preceding discussion showed that the anodic spikes have their origin in Cu rather than the oxide semiconductor film. The nanocrystalline film samples (such as the oxide films in this study) also behave in a more complicated manner under irradiation relative to their flat film counterparts. Whether minority (e.g., Figure 4.6) or majority (e.g., Figures 4.7, 4.11) carriers manifest under irradiation hinges on factors such as film conductivity in addition to the other factors identified in an earlier study.

Mott-Schottky plots have also been utilized by previous authors[114,129,133] to further confirm *n*- or *p*-type behavior for electrodeposited Cu_2O samples. Thus, if the plots have a positive slope and a negative intercept, the sample is *n*-type; and conversely for *p*-type samples, the plots will have a negative slope and positive potential intercept. Whether the oxide films containing a metallic Cu phase will exhibit behavior akin to an *n*-type semiconductor, will require capacitance-voltage measurements before and after anodic stripping. It would be interesting to see what effect (if any), the metallic Cu phase exerts on the interfacial potential distribution, and whether the Mott-Schottky plot reverts to that for a classic *p*-type semiconductor behavior once the Cu phase is stripped off. Finally, the effects of film photocorrosion must also be more carefully examined with detailed surface analyses of the films (*e.g.*, X-ray photoelectron spectroscopy or XPS) to gauge how the PCP profiles are impacted. Such measurements take on added value when done in an operando setting. It is worth noting here that XPS has challenges in resolving signals from Cu^0 when present in admixture with Cu(I). This problem is less severe in the mixed Cu^0/Cu(II) case. Complementary use of Auger electron spectroscopy also is useful in these cases.

4.1.4 *N*-type Oxide Semiconductors (TiO_2 and WO_3)

The photoelectrochemical measurements of the nanoporous TiO_2 and WO_3 films were assessed using linear sweep photovoltammetry in Na_2SO_4 supporting electrolyte with added formate species. As elaborated elsewhere,[30] photovoltammetry (a voltammetry experiment involving a slow potential ramp coupled with interrupted illumination of the semiconductor surface) permits evaluation of both the "dark" electrochemical behavior and the photoresponse of the film in one experiment and under identical experimental conditions. Figure 4.13 shows photovoltammograms for TiO_2 and WO_3 nanotube arrays obtained by anodization at 20 V and 60 V for 3 h, respectively.

The positive (anodic) photocurrents along with the entire scan, indicating the *n*-type semiconductor behavior of TiO_2 and WO_3 thin films. Note that the films showed gradual attainment of the steady-state plateau response diagnostic of the transfer of holes (minor carriers) across the electrode/electrolyte interfaces, as diagnosed by the flat baseline response in the dark. In the Na_2SO_4 electrolyte, the photogenerated holes in TiO_2 and WO_3 (that escape recombination) oxidize either adsorbed water molecules or hydroxyl groups, and the presence of formate furnishes a much more facile pathway for the transfer of holes across the electrode/electrolyte interface.

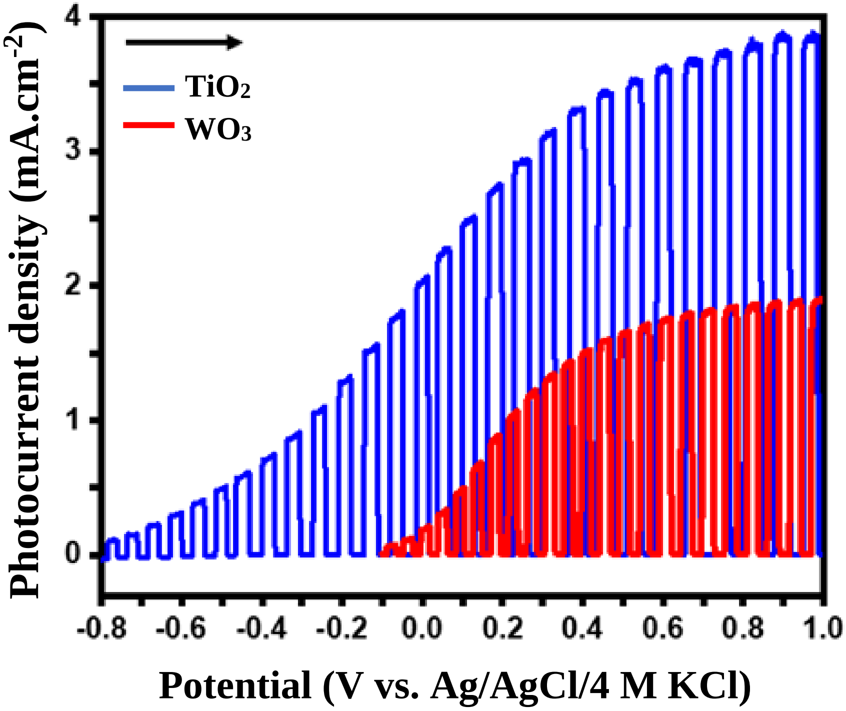

Figure 4.13 Linear sweep photovoltammograms of TiO_2 and WO_3 in 0.5 M sodium sulfate and 0.1 M sodium formate, 5 mV/s potential scan rate.

These self-organized nanoporous morphology thin films are shown to yield excellent quality of photoelectrochemical responses using the photooxidation of organic species as reaction probes. As shown in Figure 4.13, the dark (leakage) currents in these films were negligible, attesting to the excellent rectification property of the resultant semiconductor/electrolyte contacts. The photocurrent densities for the nanoporous TiO_2 and WO_3 films were significantly higher (by orders of magnitude) than those obtained with the corresponding compact film counterparts (obtained, for example, by cathodic electrodeposition, cf., Refs. 35 and 134). Therefore, these data unequivocally confirmed the good stability and quality of the aforementioned thin films. Having established that as-prepared TiO_2 and WO_3 thin films have reasonable electrochemical and PEC stability, studies of charge transfer kinetics were conducted in the dark as described in subsequent sections.

4.1.5 *P*-type Oxide Semiconductors (CuO, $AgVO_3$, and $CuBi_2O_4$)

Similar experiments were performed to assess the stability of as-prepared *p*-type thin films. The PEC experiments were conducted using dioxygen as an electron acceptor. Cathodic photocurrents were observed under negative applied bias potentials for CuO, $CuBi_2O_4$, and $AgVO_3$ electrodes consistent with *p*-type semiconductor behavior (Figures 4.14 and 4.15).

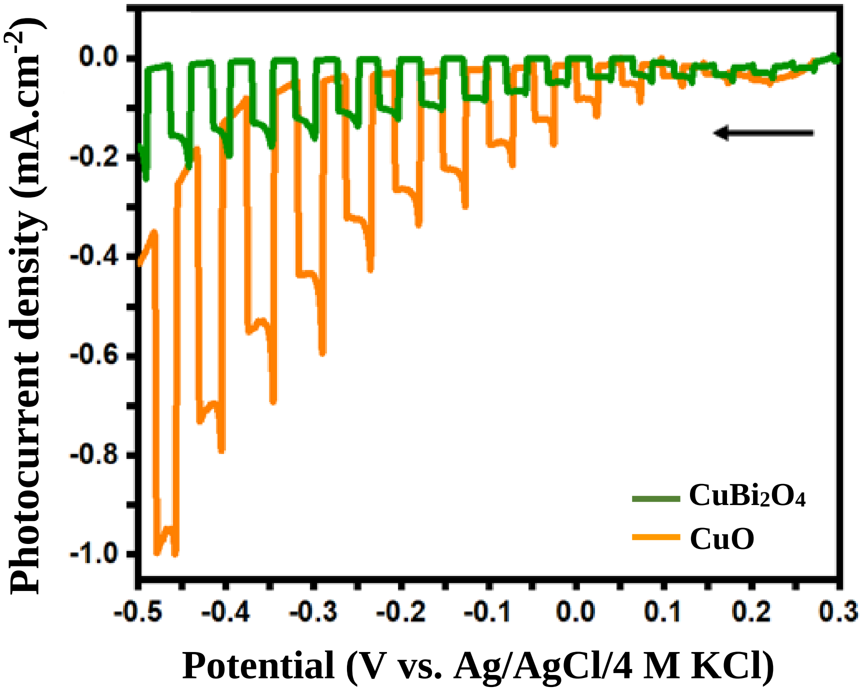

Figure 4.14 Linear sweep photovoltammograms of CuO and $CuBi_2O_4$ in 0.5 M sodium sulfate and dioxygen-purged as an electron acceptor, 5 mV/s potential scan rate.

In Figure 4.14, as long as the negative potential limit was kept above - 0.4 V, the dark current was negligible for both CuO and $CuBi_2O_4$, but below -0.4 V dark current increases with decreasing potential. A known drawback for CuO is its self-reduction by photogenerated electrons,[135,136] which may explain the dark current in Figure 4.14. Understanding the mechanism of film corrosion and how to suppress it is critical for further development of CuO photocathode but is outside the scope of this work. The PEC experiments also were conducted for electrodeposited $AgVO_3$ thin films using dioxygen as an electron acceptor in a non-aqueous electrolyte. Figure 4.15 contains the corresponding photovoltammetry data for as-prepared $AgVO_3$. Again, the dark current flow is unmistakable and signals film corrosion *in the dark* (see below).

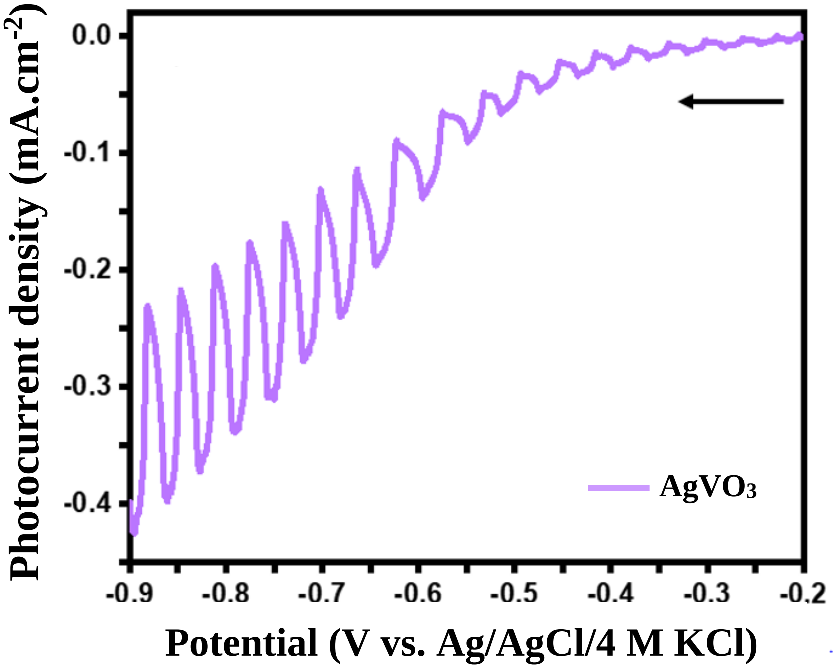

Figure 4.15 Linear sweep photovoltammograms of $AgVO_3$ in dioxygen-purged and 0.2 M tetrabutylammonium perchlorate in acetonitrile, 5 mV/s potential scan rate.

Note that these experiments were conducted in the *reverse bias* regime, thus, the photocurrents were generated by minority carriers which are electrons for a *p*-type semiconductor. Consistent with this notion, the photocurrent polarity is cathodic in the traces in Figure 4.15 in line with the *p*-type semiconductor behavior of $AgVO_3$. Unfortunately, there was significant dark current flow on applying negative overpotentials, suggesting that the $AgVO_3$ electrode/electrolyte junction was “leaky”. The dark current can be attributed to the reduction of dioxygen in the electrolyte or can arise from the reduction of the oxide itself to silver, as per details given elsewhere.[31] However, considerable improvement in the quality of the $AgVO_3$/electrolyte junction would be needed under irradiation even in the same electrolyte.

4.2 Electrochemical Properties and Charge Transfer Kinetics Analyses in the Dark

Use of a metal electrode like Pt as a benchmark and studying its electrochemical properties helps in gaining a better understanding of charge transfer kinetics at semiconductor/electrolyte interfaces. To this end, the electrochemical properties of Pt were studied in the dark and current-potential (*i-E*) curves were employed to determine the standard heterogeneous rate constant, k^0 (cm s^{-1}). In order to investigate the electron transfer kinetics, two redox couples, namely, $Fe(CN)_6^{3-/4-}$ and $Fe^{3+/2+}$ were employed. Both redox systems have been extensively studied and have been used as model systems for the characterization of electrode kinetics and diffusion coefficient determinations.[137] The reduction of ferricyanide to ferrocyanide (E°= + 0.36 V *vs.* NHE)[82] at a platinum electrode is an example of an electrode process involving two ions in solution that are coupled through the following reaction:

$$\mathrm{Fe\ (CN)_6^{3-} + e^- \leftrightarrow Fe\ (CN)_6^{4-}} \tag{4.7}$$

The charge transfer parameters characterizing the ferri-/ferrocyanide redox system in a KNO_3 solution were determined by comparison of polarization curves per procedures described in the proceeding sections. The standard redox potential of $Fe^{3+/2+}$ (+0.77 V vs. NHE) is more positive than the oxide semiconductor conduction band edge. Therefore, an electron on a *n*-type oxide semiconductor can reduce Fe^{3+} (ferric) to Fe^{2+} (ferrous) in aqueous solution (Figure 4.16).

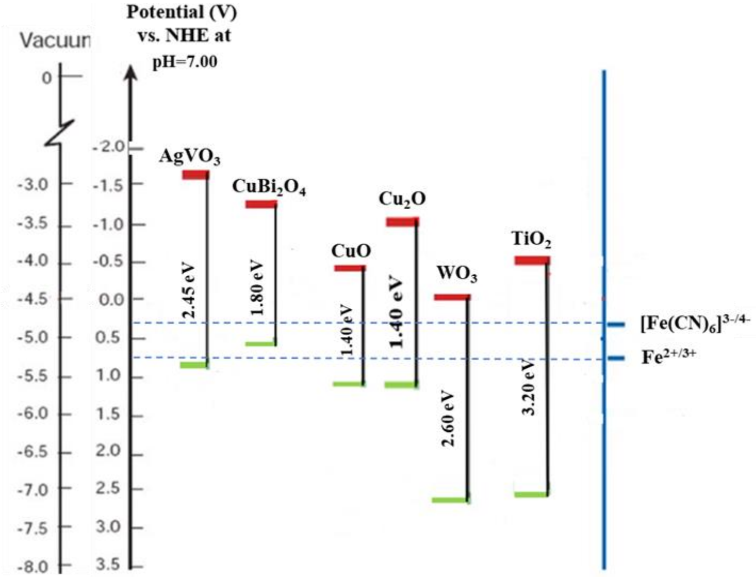

Figure 4.16 Band edge positions for selected binary and ternary oxide semiconductors (pH=7).

Prior to the measurements, the electrolyte was deoxygenated by bubbling with nitrogen gas for 10 min, while during the experiment, a nitrogen blanket was maintained over the cell. This resulted in a substantial flattening of the reduction plateau of ferricyanide due to O_2 reduction. In addition, the cell was always shielded from light in order to avoid the following photochemical decomposition of ferrocyanide.[138]

$$Fe(CN)_6^{4-} \overset{\text{light}}{\leftrightarrow} Fe(CN)_5^{3-} + CN^- \qquad [4.8]$$

$$CN^- + H_2O \leftrightarrow HCN + OH^- \qquad [4.9]$$

Figures 4.17 and 4.18 show typical *i-E* behavior of Pt in contact with the two redox couples.

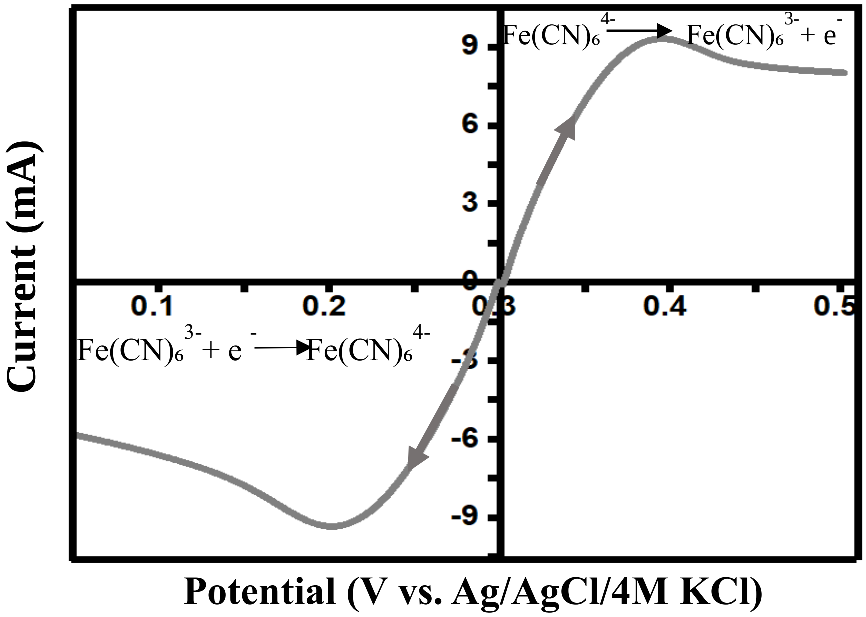

Figure 4.17 Current-potential curve for Pt in 0.5 M $[Fe(CN)_6]^{3-/4-}$ and 0.5 M KNO_3, scan rate of 5 mV/s.

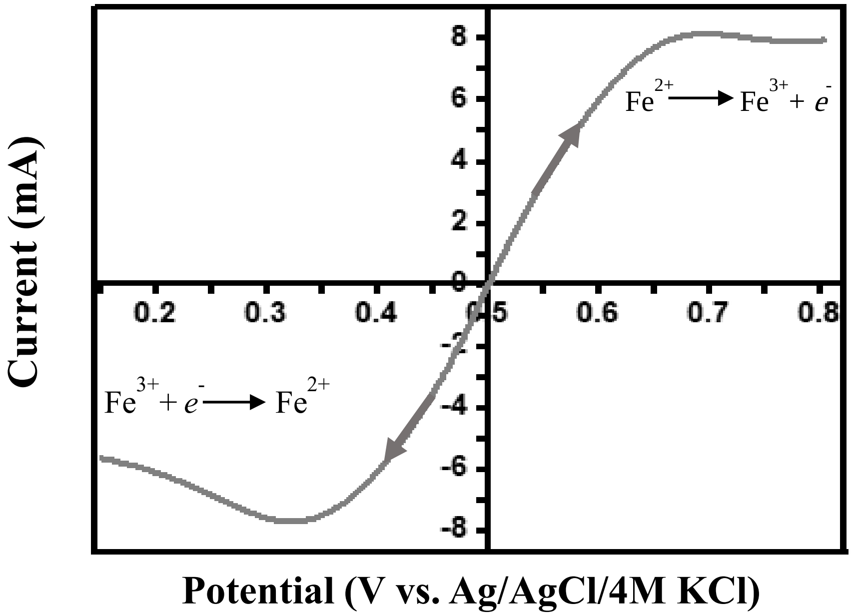

Figure 4.18 Current-potential curve for Pt in 0.5 M $Fe^{3+/2+}$ and 0.5 M KNO_3, scan rate of 5 mV/s.

The intersection point of the current density lines lies at E = +0.300 V *vs.* Ag/AgCl (0.495 vs. NHE) in Figure 4.17, which is in agreement with the literature value for the formal potential of the $Fe(CN)_6^{3-/4-}$ redox couple.[139] The transfer coefficient (α), exchange current density (j_0), and standard rate constant (k^0) were calculated from the slope and intersection of the linear part of the Tafel plot (Figure 4.19). The calculated kinetic parameters are summarized in Table 4.1.

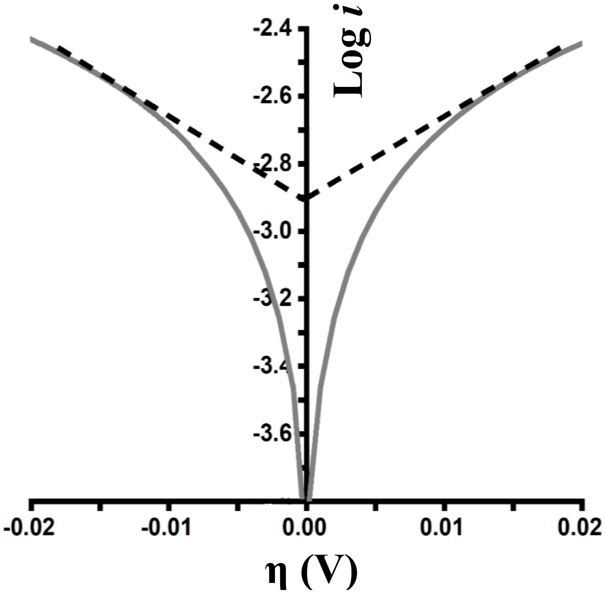

Figure 4.19 Tafel plot of Pt for $[Fe(CN)_6]^{3-} + e^- \leftrightarrow [Fe(CN)_6]^{4-}$.

Table 4.1 Kinetic parameters for Pt and the $Fe(CN)_6^{3-/4-}$ redox couple.

Electrode	**α**	**Slope (mV/decade)**	**j_0 (A/cm^2)**	**k^0 (cm/s)**
Pt (Cathodic)	0.54	109	$(3.8 \pm 0.1) \times 10^{-3}$	$(7.9 \pm 0.1) \times 10^{-5}$
Pt (Anodic)	0.49	120	$(3.8 \pm 0.1) \times 10^{-3}$	$(7.9 \pm 0.1) \times 10^{-5}$

When comparing electrode kinetics parameters measured by different methods, several considerations must be taken into account. The measurements are open to interference from slight impurities in the solutions. When a platinum electrode is used, the roughness factor and the pre-treatment of the electrode surface may differ. While the obtained α values on Pt (c.f., Table 4.1) agree with literature values (c.f., Table 2.1 in Chapter 2), this was not seen for k^0. The determined standard rate constants are significantly smaller than the values reported in the literature.[79–88] This can be attributed to the inverse proportionality of k^0 and the redox couple concentration.[140] A high concentration of redox couples was chosen to avoid the mass transfer limit prerequisite for Tafel analysis.[55]

Figure 4.18 illustrates *i-E* curve on Pt for the second redox couple, namely $Fe^{3+/2+}$. The reduction and oxidation peaks are shifted to more positive potential for Pt in contact with $Fe^{3+/2+}$ relative to the $Fe(CN)_6^{3-/4-}$ redox couple. These trends are reflective of the higher standard potential of $Fe^{3+/2+}$ redox couple (E°= + 0.77 V *vs.* NHE)[84] compared to $Fe(CN)_6^{3-/4-}$ (E°= 0.36 V *vs.* NHE).[84]

Thus, a variation of the redox couple affects the onset reduction or oxidation potential. By comparison of current densities for both redox couples, one can identify the more sluggish electron transfer kinetics of $Fe^{3+/2+}$ redox couple relative to $Fe(CN)_6^{3-/4-}$ redox couple. To couch the aforementioned differences in kinetic facility of these redox couples at Pt electrode in more quantitative terms, a Tafel plot was constructed as described earlier. Such Tafel plots are illustrated in Figures 4.19 and 4.20 for the $Fe(CN)_6^{3-/4-}$ and $Fe^{2+/3+}$ redox couples, respectively. The α, j_0, and k^0 values were calculated from the slope and intersection of the linear part of the Tafel plot. The calculated kinetic parameters are summarized in Table 4.2 for the $Fe^{2+/3+}$ redox couple. A comparison of the calculated standard rate constant (k^0) for both $Fe(CN)_6^{3-/4-}$ and $Fe^{2+/3+}$ reveals that the kinetics in the $Fe^{2+/3+}$ redox system are more sluggish than $Fe(CN)_6^{3-/4-}$ (~ one order of magnitude). An intrinsically sluggish redox behavior has been also observed for $Fe^{3+/2+}$ for Pt and ITO earlier.[42]

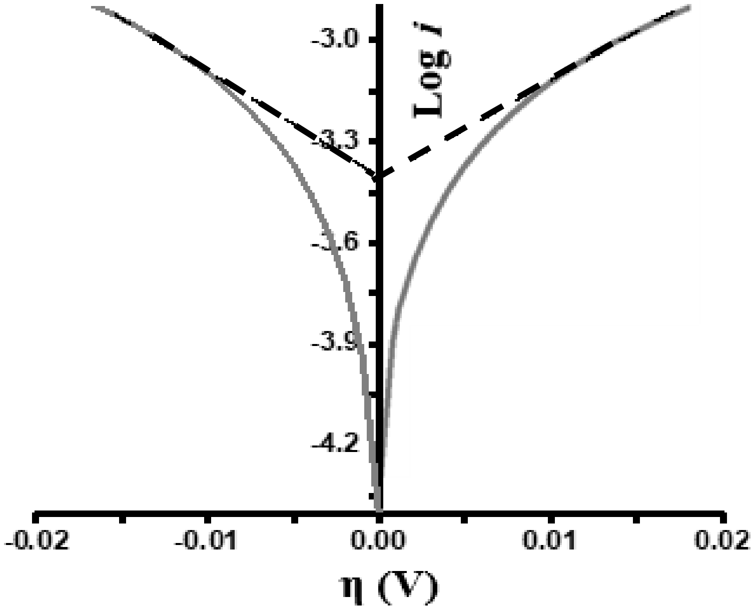

Figure 4.20 Tafel plot of Pt for $Fe^{3+} + e^- \leftrightarrow Fe^{2+}$.

Table 4.2 Kinetic parameters for Pt and the $Fe^{3+/2+}$redox couple.

Electrode	**α**	**Slope (mV/decade)**	**j_0 (A/cm^2)**	**k^0 (cm/s)**
Pt (cathodic)	0.61	96	$(4.5 \pm 0.3) \times 10^{-4}$	$(9.4 \pm 0.2) \times 10^{-6}$
Pt (anodic)	0.34	174	$(4.5 \pm 0.3) \times 10^{-4}$	$(9.4 \pm 0.2) \times 10^{-6}$

However, the current-potential behavior of the metal/electrolyte interfaces is different from semiconductor/electrolyte interfaces because there is always a large density of states on the metal surface relative to a semiconductor. A typical order of magnitude for the concentration of donors (N_D) or acceptors (N_A) in semiconductors is between 10^{16} and 10^{18} cm^{-3}, i.e., about six orders of magnitude lower than that in metals.[141] This has important implications for the charge and potential distribution at the semiconductor/electrolyte interface.[55]

4.2.1 *N*-type Oxide Semiconductors (TiO_2 and WO_3)

In the dark, a high concentration of majority carriers (electrons in a *n*-type semiconductor) controls the charge transfer kinetics. By applying potentials more negative than the flat-band potential in the forward bias regime, the conduction band electrons (majority carriers) in the *n*-type semiconductor electrode, reduce the $Fe(CN)_6^{3-}$ species.

The flat-band potentials for TiO_2 and WO_3 were extracted from the photocurrent onset potential measurements (see Figure 4.13). TiO_2 has a flat band potential of - 0.85 V vs. Ag/AgCl/4 M KCl (- 0.56 V vs NHE by converting to the pH of 7) in accordance with its onset photocurrent presented in Figure 4.13, in agreement with other literature.[30,142,143] Also, the flat-band potential of WO_3 is - 0.1 V vs Ag/AgCl/4 M KCl (+ 0.19 V vs NHE by converting to the pH of 7), again in good agreement with the literature values.[30,144]

Polarization experiments were conducted using the $Fe(CN)_6^{3-/4-}$ redox couple to probe the electrochemical charge transfer kinetics of the two electrodes. Figure 4.21 contains *i-E* curves for both TiO_2 and WO_3 in contact with $Fe(CN)_6^{3-/4-}$ redox couple. The cathodic polarity of the dark current flow in the forward bias regime for TiO_2 and WO_3 is consistent with the *n*-type semiconductor behavior of these semiconductors.

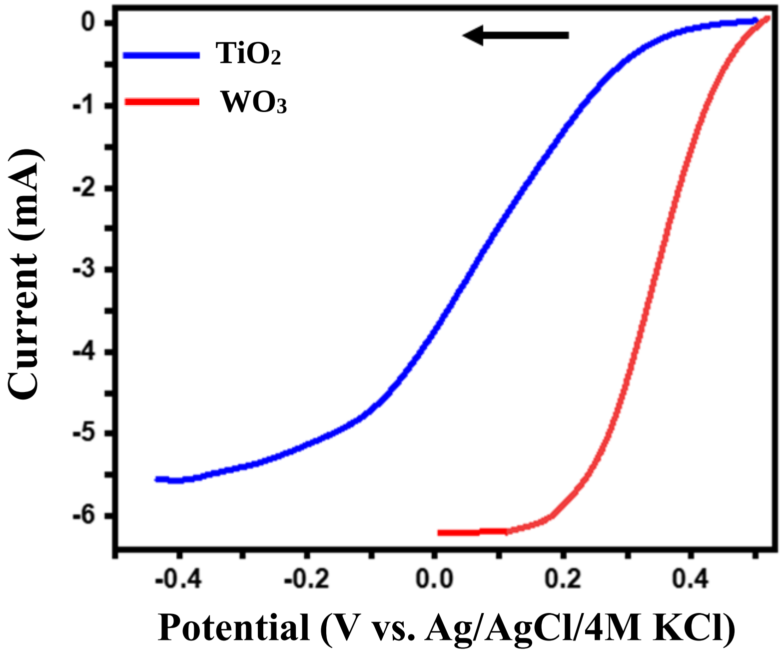

Figure 4.21 Forward bias current-potential plots of WO_3 and TiO_2, reduction of $Fe(CN)_6^{3-}$ species in 0.5 M $K_3Fe(CN)_6$, 0.5 M $K_4Fe(CN)_6$ and 0.5 M KNO_3, scan rate of 5 mV/s.

The results show that the reduction onset potential (see Figure 4.21) appeared at a more positive potential than the flat-band potential of TiO_2 and WO_3. The reduction potential onset is ~+0.35 V vs Ag/AgCl/4 M KCl (+0.55 V vs NHE) for TiO_2, while its flat-band potential is -0.56 V vs NHE. Also, the reduction potential onset is ~+0.45 V vs Ag/AgCl/4 M KCl (+0.65 V vs NHE) for WO_3, while its flat-band potential is + 0.19 V vs NHE. The discrepancy between the flat-band potential and reduction potential onset confirms the presence of the surface states since in an ideal semiconductor without any surface states, $Fe(CN)_6^{3-}$ cannot be reduced at potentials above the flat-band potential. Furthermore, the reduction peaks are shifted to a more positive potential for electrodes in contact with $Fe^{3+/2+}$ relative to the $Fe(CN)_6^{3-/4-}$ redox couple (see Figure 4.22). These trends are reflective of the higher standard potential of $Fe^{3+/2+}$ redox couple (E°= + 0.77 V *vs.* NHE)[84] compared to $Fe(CN)_6^{3-/4-}$ (E°= 0.36 V *vs.* NHE).[84] Hence, a variation of the redox couple affects the onset potentials which confirms again the presence of the surface states if we adopt the Morrison model[137] of assigning the redox potential values to surface state locations.

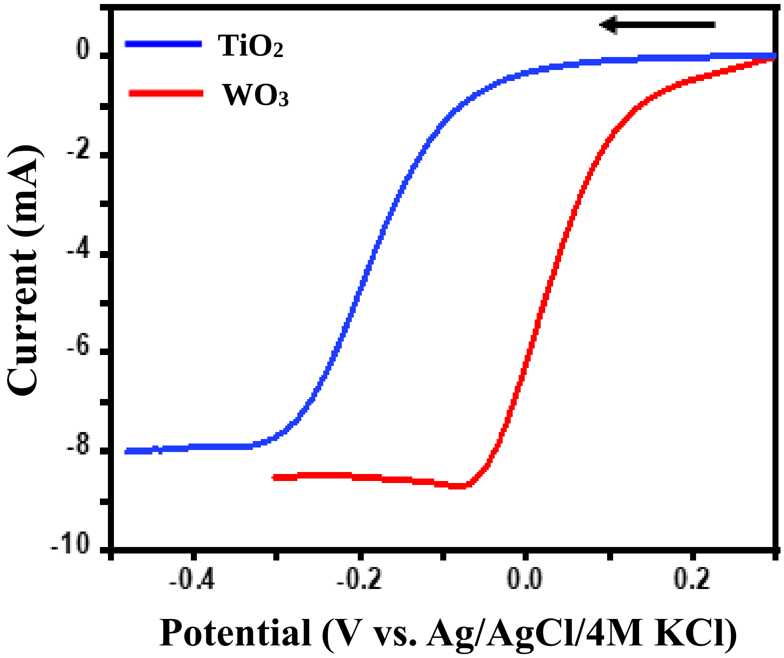

Figure 4.22 Forward bias current-potential plots of WO_3 and TiO_2, reduction of Fe^{3+} species in 0.5 M $Fe(NO_3)_3$, 0.5 M $Fe(SO)_4$ and 0.5 M KNO_3, scan rate of 5 mV/s.

Surface states can take two different forms: either, intrinsic to the semiconductor surface (e.g., dangling bonds or surface imperfections) or those formed at the semiconductor surface by adsorption of redox species or ions in the electrolyte. The above trends in the cathodic dark current-voltage curves for WO_3 and TiO_2 in the presence of two different oxidizing agents, confirm that the energy level of the surface states is changed by varying the redox specious. This is reminiscent of the Morrison model as alluded to earlier.[145,146]

The study of cathodic dark current-voltage for WO_3 and TiO_2 in the presence of two different oxidizing agents also reveals a surface state mediated electron transfer mechanism. The schematic electron transfer mechanism for nonilluminated TiO_2 and WO_3/electrolyte interfaces at equilibrium and at different bias potentials in the presence of surface states, is illustrated in Figures 4.23 and 4.24 for TiO_2 or WO_3, respectively.

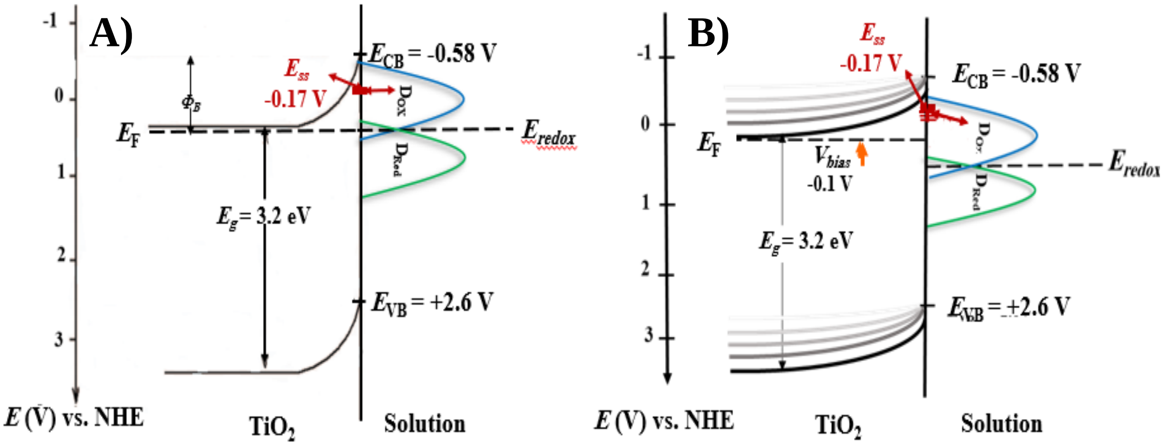

Figure 4.23 Schematic electron transfer mechanism at nonilluminated TiO_2/solution interface A) at equilibrium and B) under different bias potentials.

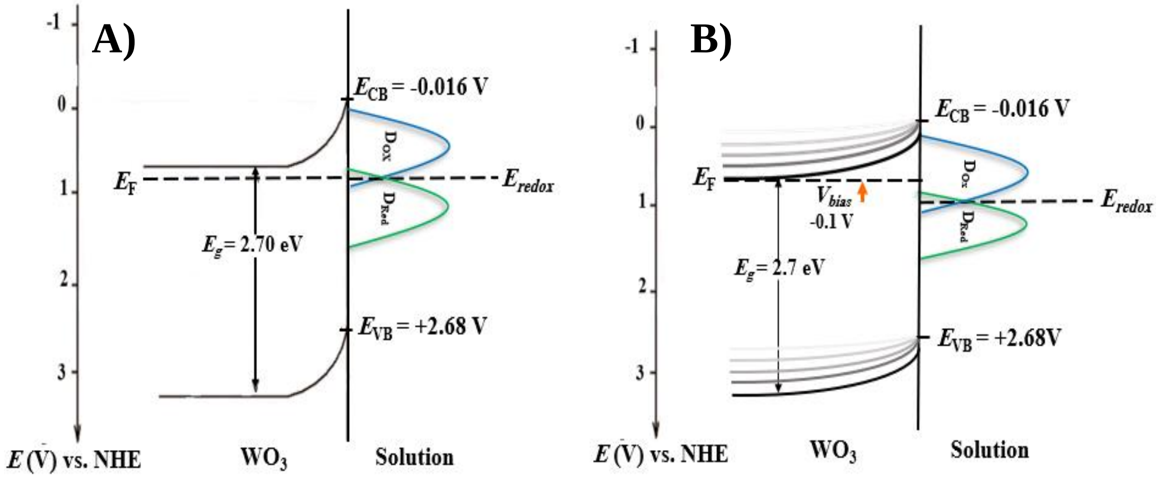

Figure 4.24 Schematic electron transfer mechanism at nonilluminated WO_3/solution interface A) at equilibrium and B) under different bias potentials.

Having established that TiO_2 has a flat band potential of - 0.85 V vs. Ag/AgCl/4 M KCl in accordance with its onset photocurrent presented in Figure 4.13, its Fermi level (E_F) was placed in the schematic diagrams at - 0.56 V vs NHE by converting to a pH of 7. The effective density states at the bottom of the conduction band (N_c) was calculated using Equation [4.10]:[147]

$$N_c = 2\left(\frac{2\pi m^* kT}{h^2}\right)^{3/2} \qquad [4.10]$$

where m^* is the effective electron mass in terms of m_0 ($m_0 = 9.11\times10^{-31}$ kg) and h is the Planck constant (6.626×10^{-34} J.s). The offset between the E_C and E_F levels can then be estimated by applying the literature values of donor densities (N_D) for TiO_2 (6.0×10^{18} cm^{-3}) [148,149] and WO_3 (7.0×10^{17} cm^{-3}) [147] in Equation [4.11]:

$$E_{CB} - E_F = \frac{kT}{e} \cdot ln\frac{N_C}{N_D} \qquad [4.11]$$

where k is the Boltzmann constant (1.38×10^{-23} J/K), T is temperature in Kelvin, and e is electron charge (1.6×10^{-19} C). The calculated E_C - E_F values for anodized TiO_2 and WO_3 films were 0.02 and 0.06 eV, respectively. These offsets were used to construct Figures 4.23 and 4.24.

Using the calculated offsets and the energy band gaps for the two semiconductors, the valence band positions could be estimated as illustrated in Figures 4.23 and 4.24. In addition, surface states (E_{ss}) at the anodized anatase TiO_2/electrolyte interfaces have been reported[150] at 0.5 eV below the conduction band edge (~ -0.17 eV). Though surface states have been invoked for WO_3/electrolyte interfaces, to the best of my knowledge, there are no reported values for E_{ss}. By applying a bias potential, the E_F of semiconductors shift upward through the negative energy diagram as shown in Figures 4.23 and 4.24. The band bending decreases when a more negative potential is applied and nearly approaches the flat band potential of a semiconductor.

Tafel plots for TiO_2 and WO_3 thin films were constructed from the cathodic polarization data in Figures 4.25 and 4.26. The linear behavior observed for these electrodes in the kinetically controlled charge transfer regime indicate that the Tafel analyses were optimal under the present experimental conditions. The calculated α values of TiO_2 and WO_3 (0.39-0.43) were relatively low for both redox couples.

In an ideal semiconductor/electrolyte interface system, α is equal to 1, however, this is rarely observed.[137,151] A Tafel slope (*dE/d log i*) of 60 mV/decade ($\alpha \cong 1$) is in accordance with the generally accepted model for direct electron transfer from conduction band to oxidized species, based upon the concepts used to describe ordinary semiconducting behavior.[55] This accepted model assumes an isoenergetic electron transfer from the semiconductor conduction band to unoccupied solution levels.

Since the α values for both TiO_2 and WO_3 were less than 1 (Tables 4.3 and 4.4) in our data, a direct isoenergetic charge transfer pathway seems unlikely. Tables 4.3 and 4.4 contain the standard charge transfer rate constants of WO_3 and TiO_2 in two different redox couples. Interpretation of Tafel data is often complicated by the existence of parallel processes at a semiconductor surface, such as corrosion, which can contribute significantly to the measured current and also by the increased series resistance due to the semiconductor electrode itself. For instance, a low α value was observed for *n*-WSe_2 by Koval and co-workers[152] for the reduction of Fe^{3+} and $Fe(CN)_6^{3-}$ (c.f., Table 2.4).

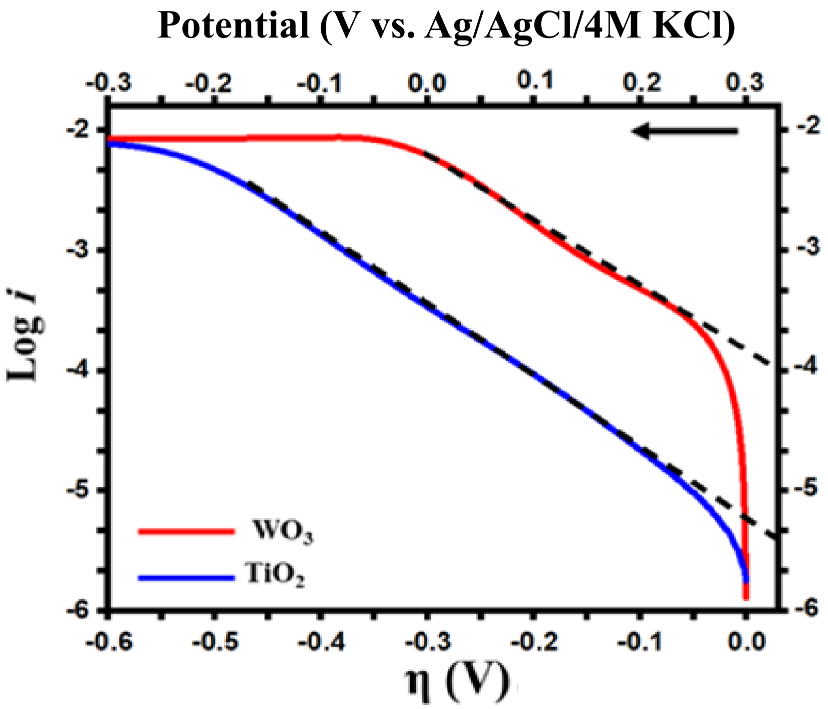

Figure 4.25 Tafel plots constructed from cathodic polarization data for WO_3 and TiO_2 in 0.5 M $Fe(CN)_6^{3-/4-}$ redox electrolyte.

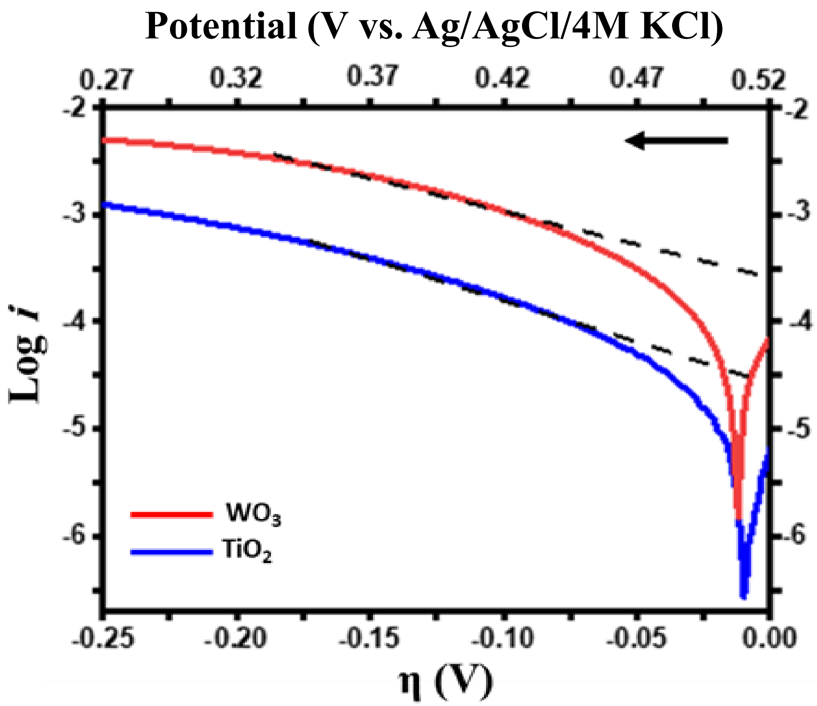

Figure 4.26 Tafel plots constructed from cathodic polarization data for WO_3 and TiO_2 in 0.5 M $Fe^{3+/2+}$ redox electrolyte.

Also, Horvat *et al.*[106] reported $\alpha < 1$ (Tafel slope of 110 mV/decade) for *n*-$Fe_{80}B_{20}$ and $Fe(CN)_6^{3-/4-}$ redox electrolytes. Consistent with the low α values less than one in previously reported literature and also in our data, a surface-state mediated charge transfer model can be invoked.

Table 4.3. Kinetic parameters for WO_3 and TiO_2 in 0.5 M $Fe(CN)_6^{3-/4-}$ redox electrolyte.

Electrode	α	Slope (mV/decade)	j_0 (A/cm^2)	k^0 (cm/s)
WO_3	0.39	151	$(4.8 \pm 0.3) \times 10^{-4}$	$(1.0 \pm 0.2) \times 10^{-5}$
TiO_2	0.39	151	$(1.5 \pm 0.3) \times 10^{-5}$	$(3.1 \pm 0.2) \times 10^{-7}$

Table 4.4. Kinetic parameters for WO_3 and TiO_2 in 0.5 M $Fe^{3+/2+}$ redox electrolyte.

Electrode	α	Slope (mV/decade)	j_0 (A/cm^2)	k^0 (cm/s)
WO_3	0.39	151	$(3.2 \pm 0.1) \times 10^{-4}$	$(6.7 \pm 0.1) \times 10^{-6}$
TiO_2	0.43	137	$(3.2 \pm 0.1) \times 10^{-5}$	$(6.7 \pm 0.1) \times 10^{-8}$

Another factor to be considered in the kinetics of charge transfer, is the surface density of states (SDOS) both for metal and semiconductor electrodes.[55] In general, the SDOS follows the trend: metal > degenerately doped semiconductor > nominally doped semiconductor.[55] The outcomes of the experiments above indicated faster kinetics for metals relative to the semiconductors. Consistent with this notion, the charge transfer kinetics at *n*-type electrodes can be ordered thus: Pt > WO_3 > TiO_2. A plausible explanation for this trend is a higher surface density of states in WO_3, relative to TiO_2. However, this hypothesis needs further verification.

4.2.2 *P*-type Oxide Semiconductors (CuO, $AgVO_3$, and $CuBi_2O_4$)

Forward bias (anodic) polarization experiments were also conducted for selected *p*-type semiconductors; namely CuO, $AgVO_3$, and $CuBi_2O_4$. The *i*-*E* curves for $Fe(CN)_6^{3-/4-}$ redox couple are illustrated in Figure 4.27. In forward bias, valence band holes oxidized $Fe(CN)_6^{4-}$ species in the positive overpotential regime. The anodic current onset potential is +0.30 V vs Ag/AgCl/4 M KCl (+0.50 V vs NHE). These results show that the oxidation onset potential (+0.50 V vs NHE at pH 7.0) appeared at a more negative potential than the flat-band potential of $AgVO_3$ (+0.65 V vs NHE at pH 7.0) and very close to the flat-band potential of $CuBi_2O_4$ (+0.53 V vs NHE at pH 7.0) and CuO (+0.46 V vs NHE at pH 7.0). Since the oxidation onset potential of the $Fe(CN)_6^{3-/4-}$ redox couple was very close to the flat-band potential of $CuBi_2O_4$ and CuO, the surface states could not be visualized. Therefore, forward bias (anodic) polarization experiments were conducted in the second candidate redox couple, $Fe^{3+/2+}$, with more positive redox potential (+0.77 vs NHE). The linear sweep voltammogram for $CuBi_2O_4$ and CuO in the presence of $Fe^{3+/2+}$ is illustrated in Figure 4.28. The oxidation onset is shifted to a more positive potential for the electrodes in contact with $Fe^{3+/2+}$ relative to the $Fe(CN)_6^{3-/4-}$ redox couple. These trends are reflective of the higher standard potential of $Fe^{3+/2+}$ redox couple ($E^\circ = +0.77$ V *vs.* NHE)[84] compared to $Fe(CN)_6^{3-/4-}$ ($E^\circ = +0.36$ V *vs.* NHE).[84] Consequently, a variation of the redox couple affects the onset potentials, which again confirms the presence of the surface states.

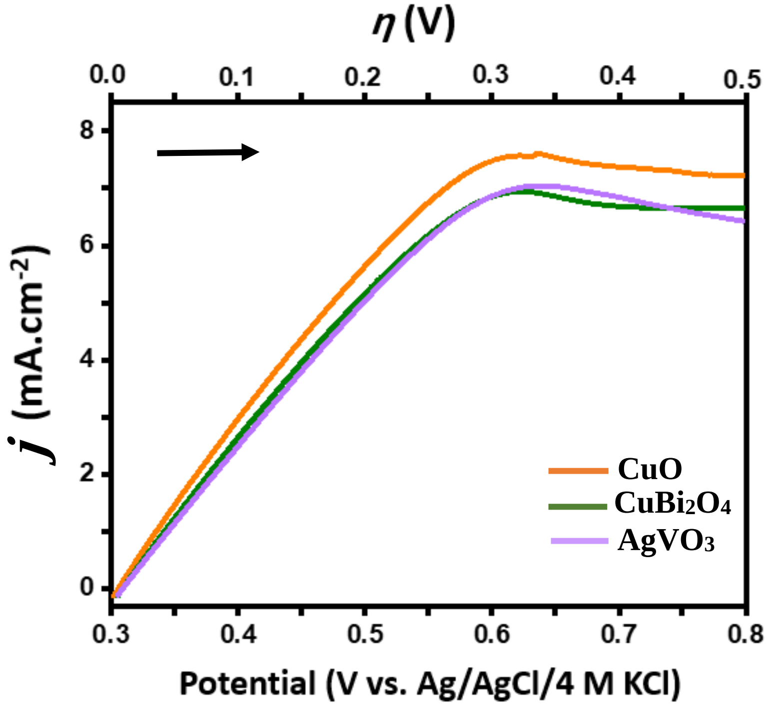

Figure 4.27 Forward bias current-potential plots for CuO, $CuBi_2O_4$, and $AgVO_3$ for oxidation of $Fe(CN)_6^{4-}$ species in 0.5 M $K_3Fe(CN)_6$, 0.5 M $K_4Fe(CN)_6$, and 0.5 M KNO_3, scan rate of 5 mV/s. The overpotentials are also shown.

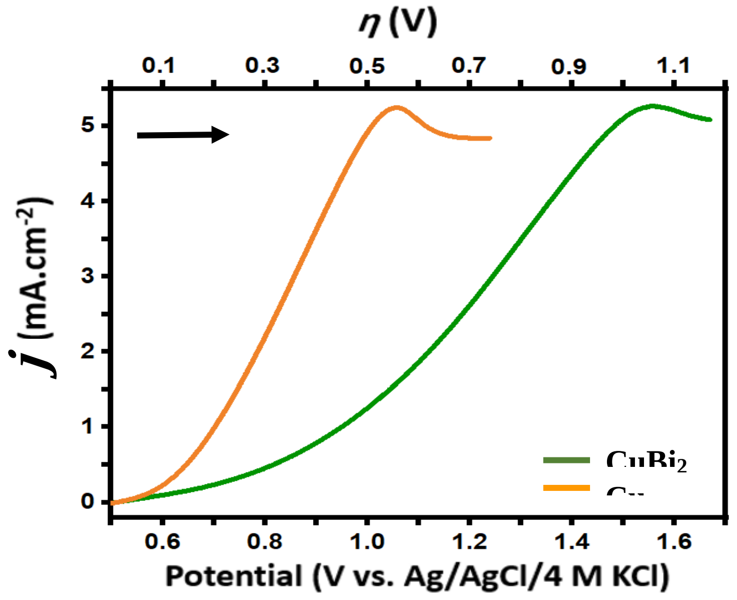

Figure 4.28 Forward bias current-potential plots for CuO and $CuBi_2O_4$ for oxidation of Fe^{2+} species in 0.5 M $Fe(NO_3)_3$, 0.5 M $Fe(SO)_4$ and 0.5 M KNO_3, scan rate of 5 mV/s. The overpotentials are also shown.

Consistent with the sluggish kinetics of the $Fe^{3+/2+}$ redox couple, these trends can be seen again from the differences in oxidation current in the two cases, $Fe(CN)_6^{3-/4-}$ and $Fe^{3+/2+}$ (see Figures 4.17 and 4.18). Figure 4.29 contains Tafel plots for CuO, $CuBi_2O_4$, and $AgVO_3$ in the presence of the 0.5 M $Fe(CN)_6^{3-/4-}$ redox couple. Figure 4.30 illustrates corresponding Tafel plots for CuO and $CuBi_2O_4$ in the presence of the 0.5 M $Fe^{3+/2+}$ redox couple. The α, j_0, and k^0 values were calculated from the slope and intersection of the linear part of the Tafel plots. The calculated kinetic parameters are summarized in Tables 4.5 and 4.6.

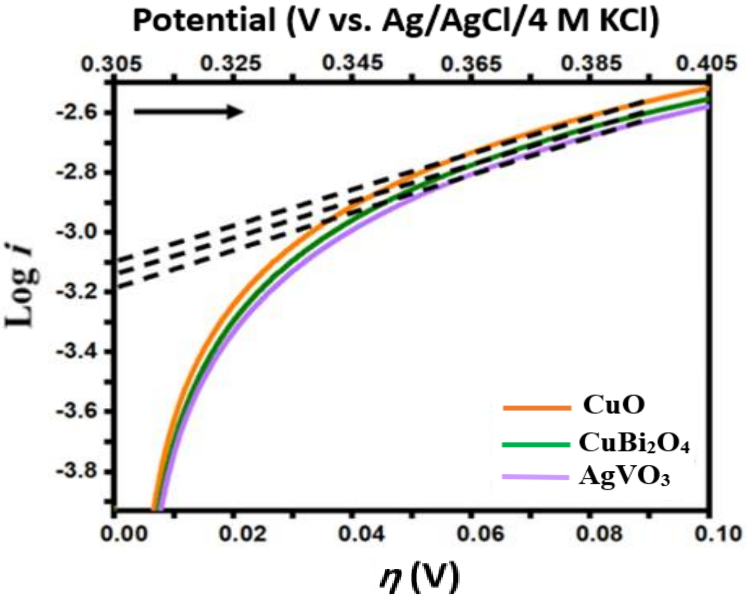

Figure 4.29 Tafel plots constructed from anodic polarization data for CuO, $CuBi_2O_4$, and $AgVO_3$ in 0.5 M $Fe(CN)_6^{3-/4-}$ redox electrolyte.

Table 4.5. Kinetic parameters for CuO, $CuBi_2O_4$, and $AgVO_3$ in 0.5 M $Fe(CN)_6^{3-/4-}$ redox.

Electrode	**α**	**Slope (mV/decade)**	**j_0 (A/cm^2)**	**k^0 (cm/s)**
CuO	0.4	147	$(1.5 \pm 0.5) \times 10^{-3}$	$(3.2 \pm 0.3) \times 10^{-5}$
$CuBi_2O_4$	0.4	147	$(1.2 \pm 0.3) \times 10^{-3}$	$(2.5 \pm 0.2) \times 10^{-5}$
$AgVO_3$	0.4	147	$(1.2 \pm 0.3) \times 10^{-3}$	$(2.5 \pm 0.4) \times 10^{-5}$

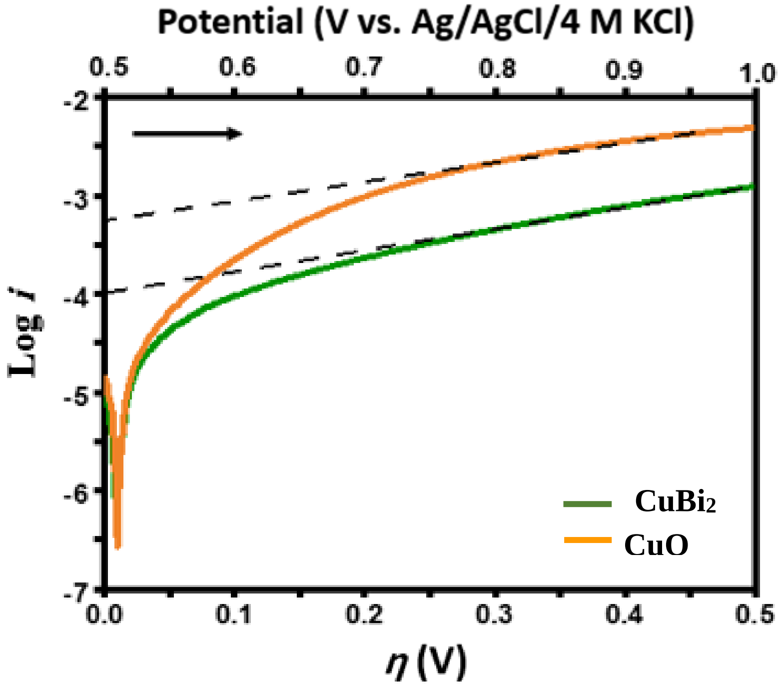

Figure 4.30 Tafel plots constructed from anodic polarization data for CuO and $CuBi_2O_4$ in 0.5 M $Fe^{3+/2+}$ redox electrolyte.

Table 4.6. Kinetic parameters for CuO and $CuBi_2O_4$ in 0.5 M $Fe^{3+/2+}$ redox electrolyte.

Electrode	**α**	**Slope (mV/decade)**	**j_0 (A/cm²)**	**k^0 (cm/s)**
CuO	0.80	74	$(7.2 \pm 0.2) \times 10^{-4}$	$(1.5 \pm 0.2) \times 10^{-5}$
$CuBi_2O_4$	0.78	76	$(1.0 \pm 0.2) \times 10^{-4}$	$(2.1 \pm 0.2) \times 10^{-6}$

On the basis of the calculations, α values equal to unity were not observed for the oxidation of $Fe(CN)_6^{4-}$ and Fe^{2+} on the *p*-type semiconductors. This can be explained by the same phenomenon related to the role of surface states in the charge transfer pathway as in the case of the *n*-type semiconductors.

CHAPTER 5

SUMMARY AND CONCLUSIONS

Chalcogenide and oxide semiconductors are important in numerous technology applications especially related to photovoltaic solar conversion, fuel cells and hydrogen generation. In this dissertation, I studied the electrochemical and photoelectrochemical (PEC) properties of semiconductors. As oxide and chalcogenide semiconductor candidates, binary *n*-type (e.g.,TiO_2 and WO_3) and *p*-type (e.g., Cu_2O and CuO) semiconductors, ternary (e.g., $AgVO_3$, $CuBi_2O_4$) semiconductors, and quaternary chalcogenides [e.g., $Ca(La_{1-x}Ce_x)_2S_4$ $(0 \leq x \leq 1)$] were selected.

In the first part, I investigated the PEC behavior of solid solution $Ca(La_{1-x}Ce_x)_2S_4$ $(0 \leq x \leq 1)$. In this series of compounds, the *f* electron density was absent in $CaLa_2S_4$ and was progressively increased until it maximized in $CaCe_2S_4$. The PEC data revealed all samples to be *n*-type semiconductors regardless of the chemical composition. The measured photocurrent was found to improve as Ce was progressively substituted for La, reaching a peak around $x = 0.50$. This can be attributed mainly to a new energy level in the host material. Continued increase of Ce content then caused a decline in photocurrent, which can be attributed to the generated oxygen crystal defects. Subsequent incorporation of Ce resulted in incremental changes in the electronic band structure. The valence band edges shifted upward resulting in a shrinking of the energy band gap from the UV range to the visible due to the reduced impact of *d* electronic states.

The second part of my dissertation related to the bipolar photoactivity of Cu_2O. This part of the study demonstrated that the use of photocurrent polarity (PCP) as an unambiguous diagnostic of *n*- or *p*-type conductivity was dependent on the semiconductor film being stringently pure and single phase. Another essential factor was the PEC stability of the film; the copper(I) oxide showed complications in the photovoltammetry data arising from possible photocorrosion of the film itself. On the other hand, the anomalous PCP was shown to be simply and inversely correlated with the amount of adventitious metallic copper in the oxide film. Importantly, the dilemma that existed to rationalize the theoretical conclusions and the fact that donor defects could not be identified for the postulated *n*-type semiconductor behavior, could be effectively circumvented.

The last part of my dissertation focused on the charge transfer kinetics at semiconductor/electrolyte interfaces in the dark. Polarization experiments were conducted using the $Fe(CN)_6^{3-/4-}$ and $Fe^{3+/2+}$ redox couples to probe the electrochemical charge transfer kinetics for the *n*-type and *p*-type electrodes. The obtained kinetics parameters were consistent with a surface state mediated charge transfer pathway (Figure 2.8) in both sets of cases.

References

(1) Kanatzidis, M. G. Discovery-Synthesis, Design, and Prediction of Chalcogenide Phases. *Inorg. Chem.* **2017**, *56*, 3158–3173.

(2) Flahaut, J. Sulfides, Selenides and Telluride, Non-Metallic Compounds- II. In *Handbook on the Physics and Chemistry of Rare Earths*; Elsevier Science, 1979; Chapter 31, pp 1–88.

(3) Zhao, H.-J.; Zhong, X.-A. Synthesis, Crystal Structure, and Optical Properties of the Noncentrosymmetric Sulfide $Ce_8Sb_2S_{15}$. *J. Solid State Chem.* **2017**, *251*, 65–69.

(4) Zhao, H.-J. Centrosymmetry vs Noncentrosymmetry in La2Ga0.33SbS5 and Ce4GaSbS9 Based on the Interesting Size Effects of Lanthanides: Syntheses, Crystal Structures, and Optical Properties. *J. Solid State Chem.* **2016**, *237*, 99–104.

(5) Iyer, A. K.; Yin, W.; Stoyko, S. S.; Rudyk, B. W.; Mar, A. Quaternary Rare-Earth Sulfides Nd_7FeInS_{13} and Pr_7CoInS_{13}. *J. Solid State Chem.* **2017**, *251*, 50–54.

(6) Kudo, A.; Miseki, Y. Heterogeneous Photocatalyst Materials for Water Splitting. *Chem. Soc. Rev.* **2009**, *38*, 253–278.

(7) Osterloh, F. E. Inorganic Materials as Catalysts for Photochemical Splitting of Water. *Chem. Mater.* **2008**, *20*, 35–54.

(8) Sivula, K.; van de Krol, R. Semiconducting Materials for Photoelectrochemical Energy Conversion. *Nat. Rev. Mater.* **2016**, *1*, 1–16.

(9) Brammertz, G.; Vermang, B.; ElAnzeery, H.; Sahayaraj, S.; Ranjbar, S.; Meuris, M.; Poortmans, J. Fabrication of Ternary and Quaternary Chalcogenide Compounds Based on Cu, Zn, Sn and Si for Thin Film Photovoltaic Applications. *Phys. Status Solidi C* **2017**, *14*, 160–162.

(10) D. Matthews, P.; D. McNaughter, P.; J. Lewis, D.; O'Brien, P. Shining a Light on Transition Metal Chalcogenides for Sustainable Photovoltaics. *Chem. Sci.* **2017**, *8*, 4177–4187.

(11) Scheer, R.; Schock, H.-W. *Chalcogenide Photovoltaics: Physics, Technologies, and Thin Film Devices*; John Wiley & Sons : New York, 2011; pp 157–208.

(12) Rajeshwar, K. Hydrogen Generation from Irradiated Semiconductor-Liquid Interfaces. In *Solar Hydrogen Generation: Toward a Renewable Energy Future*; Rajeshwar, K., McConnell, R., Licht, S., Eds.; Springer : New York, 2008; pp 167–228.

(13) Rajeshwar, K. Materials Aspects of Photoelectrochemical Energy Conversion. *J. Appl. Electrochem.* **1985**, *15*, 1.

(14) Shi, Y.; Sturm, C.; Kleinke, H. Chalcogenides as Thermoelectric Materials. *J. Solid State Chem.* **2019**, *270*, 273–279.

(15) Tedstone, A. A.; Lewis, D. J.; O' Brien, P. Synthesis, Properties, and Applications of Transition Metal-Doped Layered Transition Metal Dichalcogenides, *Chem. Mater.* **2016**, *28*, 1965–1974.

(16) Nie, L.; Zhang, Q. Recent Progress in Crystalline Metal Chalcogenides as Efficient Photocatalysts for Organic Pollutant Degradation. *Inorg. Chem. Front.* **2017**, *4*, 1953–1962.

(17) Alonso-Vante, N. Transition Metal Chalcogenides for Oxygen Reduction. In *Electrocatalysis in Fuel Cells: A Non- and Low- Platinum Approach*; Shao, M., Ed.; Lecture Notes in Energy; Springer : London, 2013; pp 417–436.

(18) Xi, X.; Wang, Z.; Zhao, W.; Park, J.-H.; Law, K. T.; Berger, H.; Forró, L.; Shan, J.; Mak, K. F. Ising Pairing in Superconducting $NbSe_2$ Atomic Layers. *Nat. Phys.* **2016**, *12*, 139–143.

(19) Yang, L.; Hong, H.; Fu, Q.; Huang, Y.; Zhang, J.; Cui, X.; Fan, Z.; Liu, K.; Xiang, B. Single-Crystal Atomic-Layered Molybdenum Disulfide Nanobelts with High Surface Activity. *ACS Nano* **2015**, *9*, 6478–6483.

(20) Gao, M.-R.; Chan, M. K. Y.; Sun, Y. Edge-Terminated Molybdenum Disulfide with a 9.4-Å Interlayer Spacing for Electrochemical Hydrogen Production. *Nat. Commun.* **2015**, *6*, 7493–7497.

(21) Voiry, D.; Yamaguchi, H.; Li, J.; Silva, R.; Alves, D. C. B.; Fujita, T.; Chen, M.; Asefa, T.; Shenoy, V. B.; Eda, G.; Chhowalla, M. Enhanced Catalytic Activity in Strained Chemically Exfoliated WS_2 Nanosheets for Hydrogen Evolution. *Nat. Mater.* **2013**, *12*, 850–855.

(22) Huang, X.; Zeng, Z.; Zhang, H. Metal Dichalcogenide Nanosheets: Preparation, Properties and Applications. *Chem. Soc. Rev.* **2013**, *42*, 1934–1946.

(23) Rajeshwar, K.; Ibanez, J. G. *Environmental Electrochemistry: Fundamentals and Applications in Pollution Sensors and Abatement*; Academic Press, 1997; pp 34–46.

(24) Weber, A.; Mainz, R.; Schock, H. W. On the Sn Loss from Thin Films of the Material System Cu–Zn–Sn–S in High Vacuum. *J. Appl. Phys.* **2010**, *107*, 013516.

(25) Perrin, M.-A.; Wimmer, E. Color of Pure and Alkali-Doped Cerium Sulfide: A Local-Density-Functional Study. *Phys. Rev. B* **1996**, *54*, 2428–2435.

(26) Sotelo, P.; Orr, M.; Galante, M. T.; Hossain, M. K.; Firouzan, F.; Longo, C.; Kormányos, A.; Sarker, H.; Janáky, C.; Huda, M. N.; Rajeshwar, K.; Macaluso, R. T. Role of f Electrons in the Optical and Photoelectrochemical Behavior of $Ca(La_{1-x}Ce_{x})_2S_4$ $(0 \leq x \leq 1)$. *Inorg. Chem.* **2019**, *58*, 4553–4560.

(27) Tao, M. Inorganic Photovoltaic Solar Cells: Silicon and Beyond. *Electrochem. Soc. Interface* **2008**, *17*, 30–35.

(28) Rajeshwar, K. Hydrogen Generation at Irradiated Oxide Semiconductor–Solution Interfaces. *J. Appl. Electrochem.* **2007**, *37*, 765–787.

(29) Sharma, V. K.; Chenay, B. V. N. Heterogeneous Photocatalytic Reduction of Fe(VI) in UV-Irradiated Titania Suspensions: Effect of Ammonia. *J. Appl. Electrochem.* **2005**, *35*, 775–781.

(30) de Tacconi, N. R.; Chenthamarakshan, C. R.; Yogeeswaran, G.; Watcharenwong, A.; de Zoysa, R. S.; Basit, N. A.; Rajeshwar, K. Nanoporous TiO_2 and WO_3 Films by Anodization of Titanium and Tungsten Substrates: Influence of Process Variables on Morphology and Photoelectrochemical Response. *J. Phys. Chem. B* **2006**, *110*, 25347–25355.

(31) Vali, A.; Sarker, H. P.; Jee, H.-W.; Kormányos, A.; Firouzan, F.; Myung, N.; Paeng, K.-J.; Huda, M. N.; Janáky, C.; Rajeshwar, K. Electrodeposition of Silver Vanadate Films: A Tale of Two Polymorphs. *ChemPhysChem* **2019**, *20* , 2635–2646.

(32) Zhang, Y. X.; Li, G. H.; Jin, Y. X.; Zhang, Y.; Zhang, J.; Zhang, L. D. Hydrothermal Synthesis and Photoluminescence of TiO_2 Nanowires. *Chem. Phys. Lett.* **2002**, *365*, 300–304.
(33) Endrődi, B.; Kecsenovity, E.; Rajeshwar, K.; Janáky, C. One-Step Electrodeposition of Nanocrystalline TiO_2 Films with Enhanced Photoelectrochemical Performance and Charge Storage. *ACS Appl. Energy Mater.* **2018**, *1*, 851–858.
(34) Alotaibi, A. M.; Sathasivam, S.; Williamson, B. A.; Kafizas, A.; Sotelo-Vazquez, C.; Taylor, A.; Scanlon, D. O.; Parkin, I. P. Chemical Vapor Deposition of Photocatalytically Active Pure Brookite TiO_2 Thin Films. *Chem. Mater.* **2018**, *30*, 1353–1361.
(35) de Tacconi, N. R.; Chanmanee, W.; Rajeshwar, K.; Rochford, J.; Galoppini, E. Photoelectrochemical Behavior of Polychelate Porphyrin Chromophores and Titanium Dioxide Nanotube Arrays for Dye-Sensitized Solar Cells. *J. Phys. Chem. C* **2009**, *113*, 2996–3006.
(36) Rajeshwar, K. Fundamentals of Semiconductor Electrochemistry and Photoelectrochemistry. In *Encyclopedia of Electrochemistry*; Bard, A. J.; Stratmann, M. Eds.; Wiley-VCH : New York, 2007; pp 1–20.
(37) Chen, X.; Mao, S. S. Titanium Dioxide Nanomaterials: Synthesis, Properties, Modifications, and Applications. *Chem. Rev.* **2007**, *107*, 2891–2959.
(38) Zheng, H.; Ou, J. Z.; Strano, M. S.; Kaner, R. B.; Mitchell, A.; Kalantar-zadeh, K. Nanostructured Tungsten Oxide–Properties, Synthesis, and Applications. *Adv. Funct. Mater.* **2011**, *21*, 2175–2196.
(39) Di Quarto, F.; Di Paola, A.; Sunseri, C. Kinetics of Growth of Amorphous WO_3 Anodic Films on Tungsten. *J. Electrochem. Soc.* **1980**, *127*, 1016–1020.
(40) Panicker, M. P. R.; Knaster, M.; Kroger, F. A. Cathodic Deposition of CdTe from Aqueous Electrolytes. *J. Electrochem. Soc.* **1978**, *125*, 566.
(41) Schlesinger, T. E.; Rajeshwar, K.; de Tacconi, N. R. Electrodeposition of Semiconductors. *Modern. Electroplating :* Schlesinger, M., Paunovic, M. Eds.; Wiley-VCH : New York, 2001; *5, 32*–45.
(42) Chyan, O. M.-R.; Rajeshwar, K. Heterojunction Photoelectrodes: II. Electrochemistry at Tin-Doped Indium Oxide/Aqueous Electrolyte Interfaces. *J. Electrochem. Soc.* **1985**, *132*, 2109–2117.
(43) Richert, H. *Electrochemical Kinetics*, 1st Edition, Springer : New York, 1982; pp 121–145.
(44) Gerischer, H. The Impact of Semiconductors on the Concepts of Electrochemistry. *Electrochimica Acta* **1990**, *35*, 1677–1699.
(45) Gerischer, H. On the Role of Electrons and Holes in Surface Reactions on Semiconductors. *Surf. Sci.* **1969**, *13*, 265–278.
(46) Smith, A. M.; Nie, S. Semiconductor Nanocrystals: Structure, Properties, and Band Gap Engineering. *Acc. Chem. Res.* **2010**, *43*, 190–200.
(47) Bard, A. J.; Memming, R.; Miller, B. Terminology in Semiconductor Electrochemistry and Photoelectrochemical Energy Conversion. *Pure Appl Chem* **1991**, *63*, 569–596.

(48) Hoffmann, M. R.; Martin, S. T.; Choi, W.; Bahnemann, D. W. Environmental Applications of Semiconductor Photocatalysis. *Chem. Rev.* **1995**, *95*, 69–96.

(49) Vandermolen, J.; Gomes, W. P.; Cardon, F. Investigation on the Kinetics of Electroreduction Processes at Dark TiO_2 and $SrTiO_3$ Single Crystal Semiconductor Electrodes. *J. Electrochem. Soc.* **1980**, *127*, 324–350.

(50) Kang, D.; Hill, J. C.; Park, Y.; Choi, K.-S. Photoelectrochemical Properties and Photostabilities of High Surface Area $CuBi_2O_4$ and Ag-Doped $CuBi_2O_4$ Photocathodes. *Chem. Mater.* **2016**, *28*, 4331–4340.

(51) Shi, H.; Zhou, C.; Zhang, C. Silver Vanadate Nanowires: Photocatalytic Properties and Theoretical Calculations. *Res. Chem. Intermed.* **2015**, *41*, 7725–7737.

(52) Chen, L.; Shet, S.; Tang, H.; Wang, H.; Deutsch, T.; Yan, Y.; Turner, J.; Al-Jassim, M. Electrochemical Deposition of Copper Oxide Nanowires for Photoelectrochemical Applications. *J. Mater. Chem.* **2010**, *20*, 6962–6967.

(53) Atkins, P.; Jones, L. *Chemical Principles: The Quest for Insight*. W. H. Freeman: New York, 2004; pp 1024–1036.

(54) Harris, D. C. *Quantitative Chemical Analysis*; W. H. Freeman : New York, 2010; pp 750–832.

(55) Bard, A. J.; Faulkner, L. R. *Electrochemical Methods: Fundamentals and Applications*, 2nd Edition; Wiley-VCH : New York, 2001; PP 732–864.

(56) Mishra, K. K.; Rajeshwar, K. A Re-Examination of the Mechanisms of Electrodeposition of CdX and ZnX (X= Se, Te) Semiconductors by the Cyclic Photovoltammetric Technique. *J. Electroanal. Chem.* **1989**, *273*, 169–182.

(57) Honda, K. Dawn of the Evolution of Photoelectrochemistry. *J. Photochem. Photobiol. Chem.* **2004**, *166*, 63–68.

(58) Nozik, A. J. Photoelectrochemistry: Applications to Solar Energy Conversion. *Annu. Rev. Phys. Chem.* **1978**, *29*, 189–222.

(59) Rajeshwar, K. Photoelectrochemistry and the Environment. *J. Appl. Electrochem.* **1995**, *25*, 1067–1082.

(60) Grätzel, M. Photoelectrochemical Cells. In *Materials for Sustainable Energy*; Nature Group : United Kingdom, 2001; pp *338*–344.

(61) Zhang, F.; Inganäs, O.; Zhou, Y.; Vandewal, K. Development of Polymer–Fullerene Solar Cells. *Natl. Sci. Rev.* **2016**, *3*, 222–239.

(62) Müller-Buschbaum, P.; Thelakkat, M.; Fässler, T. F.; Stutzmann, M. Hybrid Photovoltaics – from Fundamentals towards Application. *Adv. Energy Mater.* **2017**, *7*, 1700248–1700261.

(63) Nozik, A. J.; Memming, R. Physical Chemistry of Semiconductor- Liquid Interfaces. *J. Phys. Chem.* **1996**, *100*, 13061–13078.

(64) Gerischer, H. Electron-Transfer Kinetics of Redox Reactions at the Semiconductor/Electrolyte Contact. A New Approach. *J. Phys. Chem.* **1991**, *95*, 1356–1359.

(65) Koval, C. A.; Howard, J. N. Electron Transfer at Semiconductor Electrode-Liquid Electrolyte Interfaces. *Chem. Rev.* **1992**, *92*, 411–433.

(66) Meissner, D.; Memming, R. Analysis of Current—Potential Characteristics of *n*- and *p*-Type Semiconductor Electrodes. *Electrochimica Acta* **1992**, *37*, 799–809.

(67) Hens, Z. The Electrochemical Impedance of One-Equivalent Electrode Processes at Dark Semiconductor| Redox Electrodes Involving Charge Transfer through Surface States. 1. Theory. *J. Phys. Chem. B* **1999**, *103*, 122–129.

(68) Lewis, N. S. *Progress in Understanding Electron-Transfer Reactions at Semiconductor/Liquid Interfaces*; *J. Phys. Chem. B* **1998**, *102*, 4843–4855.

(69) Wilson, R. H. Electron Transfer Processes at the Semiconductor-Electrolyte Interface. In *Critical Reviews in Solid State and Material Sciences*; *Crit. Rev. Solid State Mater. Sci.* Taylor and Francis : New York, 1980, pp 1–41.

(70) Gerischer, H. Charge Transfer Processes at Semiconductor-Electrolyte Interfaces in Connection with Problems of Catalysis. *Surf. Sci.* **1969**, *18*, 97–122.

(71) Nakabayashi, S.; Fujishima, A.; Honda, K. Kinetic Aspects of Highly Exothermic Electron-Transfer Reactions in Heterogeneous Systems. *J. Phys. Chem.* **1983**, *87*, 3487–3492.

(72) Marcus, R. A. On the Theory of Oxidation-Reduction Reactions Involving Electron Transfer. I. *J. Chem. Phys.* **1956**, *24*, 966–978.

(73) Tender, L.; Carter, M. T.; Murray, R. W. Cyclic Voltammetric Analysis of Ferrocene Alkanethiol Monolayer Electrode Kinetics Based on Marcus Theory. *Anal. Chem.* **1994**, *66*, 3173–3181.

(74) Marcus, R. A.; Sutin, N. Electron Transfers in Chemistry and Biology. *Biochimica. et Biophysica. Acta.* **1985**, *811*, 265–322.

(75) Marcus, R. A. On the Theory of Electron-Transfer Reactions. VI. Unified Treatment for Homogeneous and Electrode Reactions. *J. Chem. Phys.* **1965**, *43*, 679–701.

(76) Nicholson, R. S.; Shain, I. Theory of Stationary Electrode Polarography. Single Scan and Cyclic Methods Applied to Reversible, Irreversible, and Kinetic Systems. *Anal. Chem.* **1964**, *36*, 706–723.

(77) Nicholson, R. S. Semiempirical Procedure for Measuring with Stationary Electrode Polarography Rates of Chemical Reactions Involving the Product of Electron Transfer. *Anal. Chem.* **1966**, *38*, 1406–1406.

(78) Nicholson, R. S. Theory and Application of Cyclic Voltammetry for Measurement of Electrode Reaction Kinetics. *Anal. Chem.* **1965**, *37*, 1351–1355.

(79) Randles, J. E. B.; Somerton, K. W. Kinetics of Rapid Electrode Reactions. Part 3. Electron Exchange Reactions. *Trans. Faraday Soc.* **1952**, *48*, 937–950.

(80) Wijnen, M. D.; Smit, W. M. Square Wave Electrolysis IV. Results and Discussion. *Recl. Trav. Chim. Pays-Bas* **1960**, *79*, 289–312.

(81) Jordan, J.; Javick, R. A. Electrode Kinetics by Hydrodynamic Voltammetry, Study of Ferrous-Ferric, Ferrocyanide-Ferricyanide and Iodide-Iodine Systems. *Electrochimica Acta.* **1962**, *6*, 23–33.

(82) Jahn, D.; Vielstich, W. Rates of Electrode Processes by the Rotating Disk Method. *J. Electrochem. Soc.* **1962**, *109*, 849–862.

(83) Daum, P. H.; Enke, C. G. Electrochemical Kinetics of the Ferri-Ferrocyanide Couple on Platinum. *Anal. Chem.* **1969**, *41*, 653–656.

(84) Angell, D. H.; Dickinson, T. The Kinetics of the Ferrous/Ferric and Ferro/Ferricyanide Reactions at Platinum and Gold Electrodes: Part I. Kinetics at Bare-Metal Surfaces. *J. Electroanal. Chem.* **1972**, *35*, 55–72.

(85) Sharp, M.; Petersson, M.; Edström, K. A Comparison of the Charge Transfer Kinetics between Platinum and Ferrocene in Solution and in the Surface Attached State. *J. Electroanal. Chem.* **1980**, *109*, 271–288.

(86) Kempton, J. H.; Lindberg, R. D.; Runnells, D. D. Numerical Modeling of Platinum Eh Measurements by Using Heterogeneous Electron-Transfer Kinetics. In *Chemical Modeling of Aqueous Systems II*; ACS Symposium Series 416, American Chemical Society : Washington, D. C., 1990; pp 339–349.

(87) Winkler, K. The Kinetics of Electron Transfer in Fe (CN) 64- 3- Redox System on Platinum Standard-Size and Ultramicroelectrodes. *J. Electroanal. Chem.* **1995**, *388*, 151–159.

(88) Bortels, L.; Van den Bossche, B.; Deconinck, J.; Vandeputte, S.; Hubin, A. Analytical Solution for the Steady-State Diffusion and Migration Involving Multiple Reaction Ions Application to the Identification of Butler-Volmer Kinetic Parameters for the Ferri-/Ferrocyanide Redox Couple. *J. Electroanal. Chem.* **1997**, *429*, 139–155.

(89) Gerischer, H. Eine Einführung in die Methoden zur Untersuchung der Kinetik von Elektrodenprozessen. *Z. Für Elektrochem. Berichte Bunsenges. Für Phys. Chem.* **1955**, *59*, 604–612.

(90) Anson, F. C. Exchange Current Densities for Fe (II)-Fe (III) Solutions in Sulfuric Acid and Perchloric Acid. *Anal. Chem.* **1961**, *33*, 939–942.

(91) Galus, Z.; Adams, R. N. The Investigation of the Kinetics of Moderately Rapid Electrode Reactions Using Rotating Disk Electrodes. *J. Phys. Chem.* **1963**, *67*, 866–871.

(92) Weber, J.; Samec, Z.; Mareček, V. The Effect of Anion Adsorption on the Kinetics of the Fe^{3+}/Fe^{2+} Reaction on Pt and Au Electrodes in $HClO_4$. *J. Electroanal. Chem.* **1978**, *89*, 271–288.

(93) Morrison, B.; Striebel, K.; Ross Jr, P. N.; Andricacos, P. C. Kinetic Studies Using a Rotating Cylinder Electrode: Part I. Electron Transfer Rates in Ferrous/Ferric Sulfate on Platinum. *J. Electroanal. Chem.* **1986**, *215*, 151–160.

(94) Tan, S.; Lazenby, R. A.; Bano, K.; Zhang, J.; Bond, A. M.; Macpherson, J. V.; Unwin, P. R. Comparison of Fast Electron Transfer Kinetics at Platinum, Gold, Glassy Carbon and Diamond Electrodes Using Fourier-Transformed AC Voltammetry and Scanning Electrochemical Microscopy. *Phys. Chem. Chem. Phys.* **2017**, *19*, 8726–8734.

(95) Harinipriya, S.; Sangaranarayanan, M. V. Electron Transfer Reactions at Metal Electrodes: Influence of Work Function on Free Energy of Activation and Exchange Current Density. *J. Chem. Phys.* **2001**, *115*, 6173–6178.

(96) Blum, L.; Quijada, M.; Schmidt, P. P. Kinetics of Charge Transfer at Metal Electrolyte Interfaces: From Classical to Quantum Statistics. *Int. J. Quantum Chem.* **1987**, *32*, 245–249.

(97) Gellings, P. J. *The CRC Handbook of Solid State Electrochemistry*, 1st Edition.; Gellings, P. J., Bouwmeester, H. J. M., Eds.; CRC Press, 2019; pp 274–280.

(98) Antiochia, R.; Lavagnini, I.; Magno, F.; Valentini, F.; Palleschi, G. Single-Wall Carbon Nanotube Paste Electrodes: A Comparison with Carbon Paste, Platinum and

Glassy Carbon Electrodes via Cyclic Voltammetric Data. *J. Electroanalysis* **2004**, *16*, 1451–1458.

(99) Gerischer, H. Electrochemical Behavior of Semiconductors under Illumination. *J. Electrochem. Soc.* **1966**, *113*, 1174–1179.

(100) Lewis, N. S. An Analysis of Charge Transfer Rate Constants for Semiconductor/Liquid Interfaces. *Annu. Rev. Phys. Chem.* **1991**, *42*, 543–580.

(101) Rodman, S.; Spitler, M. T. Determination of Rate Constants for Dark Current Reduction at Semiconductor Electrodes Using ZnO Single-Crystal Microelectrodes. *J. Phys. Chem. B* **2000**, *104*, 9438–9443.

(102) Azcarate, I.; Costentin, C.; Methivier, C.; Laberty-Robert, C.; Grimaud, A. Electron Transfer at the Metal Oxide/Electrolyte Interface: A Simple Methodology for Quantitative Kinetics Evaluation. *J. Phys. Chem. C* **2018**, *122*, 12761–12770.

(103) Farjardo, A. M.; Lewis, N. S. Rate Constants for Charge Transfer across Semiconductor-Liquid Interfaces. *Science AAAS* **1996**, *274,* 969–972.

(104) Acharya, S.; Lancaster, M.; Maldonado, S. Semiconductor Ultramicroelectrodes: Platforms for Studying Charge-Transfer Processes at Semiconductor/Liquid Interfaces. *Anal. Chem.* **2018**, *90*, 12261–12269.

(105) Hens, Z.; Gomes, W. P. The Electrochemical Impedance of One-Equivalent Electrode Processes at Dark Semiconductor/Redox Electrodes Involving Charge Transfer through Surface States. 2. The *n*-GaAs/Fe^{3+} System as an Experimental Example. *J. Phys. Chem. B* **1999**, *103,* 130–138.

(106) Horvat-Radošević, V.; Kvastek, K.; Križekar, D. Kinetics of the $[Fe(CN)_6]^{3-}$/$[Fe(CN)_6]^{4-}$ Redox Couple Reaction on Anodically Passivated $Fe_{80}B_{20}$. *Croat. Chem. Acta* **1997**, *70*, 537–561.

(107) Uhlendorf, I.; Reineke-Koch, R.; Memming, R. Investigation of the Kinetics of Redox Reactions at GaAs Electrodes by Impedance Spectroscopy. *J. Phys. Chem.* **1996**, *100*, 4930–4936.

(108) Ahmed, S. M.; Gerischer, H. Influence of Crystal Surface Orientation on Redox Reactions at Semiconducting MoS2. *Electrochimica Acta.* **1979**, *24*, 705–711.

(109) Horrocks, B. R.; Mirkin, M. V.; Bard, A. J. Scanning Electrochemical Microscopy. 25. Application to Investigation of the Kinetics of Heterogeneous Electron Transfer at Semiconductor (WSe_2 and Si) Electrodes. *J. Phys. Chem.* **1994**, *98*, 9106–9114.

(110) Marcus, R. A. Electrostatic Free Energy and Other Properties of States Having Nonequilibrium Polarization. I. *J. Chem. Phys.* **1956**, *24*, 979–989.

(111) Noufi, R. N.; Kohl, P. A.; Frank, S. N.; Bard, A. J. Semiconductor Electrodes: XIV. Electrochemistry and Electroluminescence at *n*-Type in Aqueous Solutions. *J. Electrochem. Soc.* **1978**, *125*, 246.

(112) Salvador, P.; Gutierrez, C. Mechanisms of Charge Transfer at the Semiconductor-Electrolyte Interface: I. Kinetics of Electroreduction at Dark of and in Aqueous Solution on a Sintered Nb-Doped Electrode: Influence of pH. *J. Electrochem. Soc.* **1984**, *131*, 326–334.

(113) Kalubowila, K.; Gunawardhana, L.; Wijesundera, R. P.; Siripala, W. Methods for Improving *n*-Type Photoconductivity of Electrodeposited Cu_2O Thin Films. *Semicond. Sci. Technol.* **2014**, *29*, 075012–075019.

(114) Wang, P.; Wu, H.; Tang, Y.; Amal, R.; Ng, Y. H. Electrodeposited Cu_2O as Photoelectrodes with Controllable Conductivity Type for Solar Energy Conversion. *J. Phys. Chem. C* **2015**, *119*, 26275–26282.

(115) Patnaik, P. *Dean's Analytical Chemistry Handbook*. 2nd Edition; Springer : New York, 1990; pp 290–297.

(116) Cullity, B. D. *Elements of X-Ray Diffraction*; Addison-Wesley : Massachusetts, 1967; pp 75–83.

(117) Macak, J. M.; Tsuchiya, H.; Taveira, L.; Aldabergerova, S.; Schmuki, P. Smooth Anodic TiO_2 Nanotubes. *Angew. Chem. Int. Ed.* **2005**, *44*, 7463–7465.

(118) Chen, S. W.; Lee, J. M.; Lu, K. T.; Pao, C. W.; Lee, J. F.; Chan, T. S.; Chen, J. M. Band-Gap Narrowing of TiO2 Doped with Ce Probed with x-Ray Absorption Spectroscopy. *Appl. Phys. Lett.* **2010**, *97*, 012104–012110.

(119) Li, Y.; Xu, R.; Wei, D.; Feng, R.; Fan, D.; Zhang, N.; Wei, Q. A Photoelectrochemical Aptasensor for the Detection of 17β-Estradiol Based on In_2S_3 and CdS Co-Sensitized Cerium Doped TiO_2. *New J. Chem.* **2019**, *44*, 346–353.

(120) Patra, A. S.; Chauhan, M. S.; Keene, S.; Gogoi, G.; Reddy, K. A.; Ardo, S.; Prasad, D. L. V. K.; Qureshi, M. Combined Experimental and Theoretical Insights into the Synergistic Effect of Cerium Doping and Oxygen Vacancies in $BaZrO_{3-\delta}$ Hollow Nanospheres for Efficient Photocatalytic Hydrogen Production. *J. Phys. Chem. C* **2019**, *123*, 233–249.

(121) Ellis, A. B.; Kaiser, S. W.; Bolts, J. M.; Wrighton, M. S. Study of *n*-Type Semiconducting Cadmium Chalcogenide-Based Photoelectrochemical Cells Employing Polychalcogenide Electrolytes. *J. Am. Chem. Soc.* **1977**, *99*, 2839–2848.

(122) Meissner, D.; Memming, R.; Kastening, B. Photoelectrochemistry of Cadmium Sulfide. 1. Reanalysis of Photocorrosion and Flat-Band Potential. *J. Phys. Chem.* **1988**, *92*, 3476–3483.

(123) Sotelo, P.; Orr, M.; Galante, M. T.; Hossain, M. K.; Firouzan, F.; Vali, A.; Li, J.; Subramanian, M.; Longo, C.; Rajeshwar, K.; Macaluso, R. T. Ternary Rare Earth Sulfide $CaCe_2S_4$: Synthesis and Characterization of Stability, Structure, and Photoelectrochemical Properties in Aqueous Media. *J. Solid State Chem.* **2018**, *262*, 149–155.

(124) Bard, A. J.; Wrighton, M. S. Thermodynamic Potential for the Anodic Dissolution of *n*-Type Semiconductors: A Crucial Factor Controlling Durability and Efficiency in Photoelectrochemical Cells and an Important Criterion in the Selection of New Electrode/Electrolyte Systems. *J. Electrochem. Soc.* **1977**, *124*, 1706–1723.

(125) Gerischer, H. On the Stability of Semiconductor Electrodes against Photodecomposition. *J. Electroanal. Chem.* **1977**, *82*, 133–143.

(126) Bouroushian, M. Monographs in Electrochemistry. In *Electrochemistry of Metal Chalcogenides*; Springer : Germany, 2010; pp 178–190.

(127) Scanlon, D. O.; Morgan, B. J.; Watson, G. W.; Walsh, A. Acceptor Levels in *p*-Type Cu_2O: Rationalizing Theory and Experiment. *Phys. Rev. Lett.* **2009**, *103*, 096405–096412.

(128) Raebiger, H.; Lany, S.; Zunger, A. Origins of the P-Type Nature and Cation Deficiency in Cu_2O and Related Materials. *Phys. Rev. B* **2007**, *76*, 045209–045223.

(129) Han, J.; Chang, J.; Wei, R.; Ning, X.; Li, J.; Li, Z.; Guo, H.; Yang, Y. Mechanistic Investigation on Tuning the Conductivity Type of Cuprous Oxide (Cu_2O) Thin Films via Deposition Potential. *Int. J. Hydrogen Energ.* **2018**, *43*, 13764–13777.

(130) Scanlon, D. O.; Watson, G. W. Undoped *n*-Type Cu_2O: Fact or Fiction? *J. Phys. Chem. Lett.* **2010**, *1*, 2582–2585.

(131) Lim, J.-W.; Isshiki, M. Electrical Resistivity of Cu Films Deposited by Ion Beam Deposition: Effects of Grain Size, Impurities, and Morphological Defect. *J. Appl. Phys.* **2006**, *99*, 094909–094915.

(132) Valladares, L.; Salinas, D. H.; Dominguez, A. B.; Najarro, D. A.; Khondaker, S. I.; Mitrelias, T.; Barnes, C. H. W.; Aguiar, J. A.; Majima, Y. Crystallization and Electrical Resistivity of Cu_2O and CuO Obtained by Thermal Oxidation of Cu Thin Films on SiO_2/Si Substrates. *Thin Solid Films* **2012**, *520*, 6368–6374.

(133) Wang, L.; Tao, M. Fabrication and Characterization of pn Homojunctions in Cuprous Oxide by Electrochemical Deposition. *Electrochem. Solid State Lett.* **2007**, *10*, H248–H264.

(134) de Tacconi, N. R.; Chenthamarakshan, C. R.; Rajeshwar, K.; Pauporté, T.; Lincot, D. Pulsed Electrodeposition of WO_3–TiO_2 Composite Films. *Electrochem. Commun.* **2003**, *5*, 220–224.

(135) Tang, H.; Matin, M. A.; Wang, H.; Sudhakar, S.; Chen, L.; Al-Jassim, M. M.; Yan, Y. Enhancing the Stability of CuO Thin-Film Photoelectrodes by Ti Alloying. *J. Electron. Mater.* **2012**, *41*, 3062–3067.

(136) Xing, H.; Lei, E.; Guo, Z.; Zhao, D.; Li, X.; Liu, Z. Exposing the Photocorrosion Mechanism and Control Strategies of a CuO Photocathode. *Inorg. Chem. Front.* **2019**, *6*, 2488–2499.

(137) Morrison, S. R. *Electrochemistry at Semiconductor and Oxidized Metal Electrodes;* Plenum Press : New York, 1980; pp 2184–2199.

(138) Kraljić, I. Decomposition of Ferrocyanide in Analysis: IV. New Spot Test for Gold. *Anal. Chim. Acta.* **1960**, *23*, 514–517.

(139) Wilhelm, S. M.; Yun, K. S.; Ballenger, L. W.; Hackerman, N. Semiconductor Properties of Iron Oxide Electrodes. *J. Electrochem. Soc.* **1979**, *126*, 419–427.

(140) Ammar, I. A.; Darwish, S. A.; Khalil, M. W.; El-Taher, S. Kinetics of the Ferro— Ferricyanide Electron Transfer Reaction on Anodically Formed Tin Oxide. *Electrochimica Acta.* **1988**, *33*, 231–238.

(141) Peter, L.; Lewerenz, H.-J. *Photoelectrochemical Water Splitting: Materials, Processes and Architectures*; RSC : United Kingdom, 2013; pp 80–97.

(142) Sang, L. X.; Zhang, Z. Y.; Ma, C. F. Photoelectrical and Charge Transfer Properties of Hydrogen-Evolving TiO_2 Nanotube Arrays Electrodes Annealed in Different Gases. *Int. J. Hydrog. Energy* **2011**, *36*, 4732–4738.

(143) Kavan, L.; Grätzel, M.; Gilbert, S. E.; Klemenz, C.; Scheel, H. J. Electrochemical and Photoelectrochemical Investigation of Single-Crystal Anatase. *J. Am. Chem. Soc.* **1996**, *118*, 6716–6723.

(144) Zych, M.; Syrek, K.; Zaraska, L.; Sulka, G. D. Improving Photoelectrochemical Properties of Anodic WO_3 Layers by Optimizing Electrosynthesis Conditions. *Molecules* **2020**, *25*, 6011–6023.

(145) Boschloo, G.; Fitzmaurice, D. Spectroelectrochemical Investigation of Surface States in Nanostructured TiO_2 Electrodes. *J. Phys. Chem. B* **1999**, *103*, 2228–2231.

(146) Tomkiewicz, M. Surface States on Chemically Modified TiO_2 Electrodes. *Surf. Sci.* **1980**, *101*, 286–294.

(147) Abou-Ras, D.; Kirchartz, T.; Rau, U. *Advanced Characterization Techniques for Thin Film Solar Cells*; Wiley-VCH : New York, 2016; pp 69–84.

(148) Tang, H.; Prasad, K.; Sanjines, R.; Schmid, P. E.; Levy, F. Electrical and Optical Properties of TiO_2 Anatase Thin Films. *J. Appl. Phys.* **1994**, *75*, 2042–2047.

(149) Goldner, R. B.; Wong, K.; Foley, G.; Norton, P.; Wamboldt, L.; Seward, G.; Haas, T.; Chapman, R. Thin Films of WO_3 for Practical Electrochromic Windows. *Sol. Energy Mater.* **1987**, *16*, 365–370.

(150) Mora-Seró, I.; Bisquert, J. Fermi Level of Surface States in TiO_2 Nanoparticles. *Nano Lett.* **2003**, *3*, 945–949.

(151) Henderson, D.; Jost, W.; Eyring, H. *Physical Chemistry: An Advanced Treatise*; Academic Press : New York, 1967; pp 129–136.

(152) Koval, C. A.; Olson, J. B. Simultaneous Determination of Interfacial Energetics and Kinetic Currents at the Tungsten Diselenide/Acetonitrile Interface. *J. Phys. Chem.* **1988**, *92*, 6726–6732.

BIOGRAPHICAL INFORMATION

Farinaz Firouzan was born and raised in Tehran, Iran. She completed her bachelor's degree in chemical engineering from the Science and Technology University in Iran. Farinaz then joined Dr. Rajeshwar's group in 2016 at the University of Texas at Arlington as a PhD student in Chemistry. Her research mainly focused on electrochemical and photoelectrochemical properties of oxide and chalcogenide semiconductors. She aspires to continue her research adventure either in academia or industry.